UNIVERSITY OF OKLAHOMA

GRADUATE COLLEGE

RESERVOIR CHARACTERIZATION OF THE BRAE FORMATION, SOUTH BRAE FIELD, UK NORTH SEA

A THESIS

SUBMITTED TO THE GRADUATE FACULTY

in partial fulfillment of the requirements for the

Degree of

MASTER OF SCIENCE

By

MUIZZ AYOKANMI MATEMILOLA
Norman, Oklahoma
2018

RESERVOIR CHARACTERIZATION OF THE BRAE FORMATION, SOUTH BRAE FIELD, UK NORTH SEA

A THESIS APPROVED FOR THE

CONOCOPHILLIPS SCHOOL OF GEOLOGY AND GEOPHYSICS

BY

Dr. Roger M. Slatt, Chair

Dr. Kurt Marfurt

Dr. Fuge Zou

ACKNOWLDGEMENTS

I am forever indebted to Dr. Roger Slatt for the wonderful experience my master's degree program has been. It was an honor to learn from him and his nuggets of wisdom. Working under him and experiencing his kindness was an absolute pleasure. Thank you.

I would like to appreciate both of my committee members. Dr. Kurt Marfurt for the opportunity to learn from him at OU and for being a part of my committee. Dr. Fuge Zou for his continued support during my time at OU and at Marathon Oil.

This research was made possible by Marathon Oil Corporation. I would like to thank them for granting me access to their dataset and for the permission to publish. I appreciate their continued support for the Institute of Reservoir Characterization, through which this research was funded. I also want to thank Schlumberger for their donation of *Petrel*™ and *Techlog*™ licenses to the School of Geology and Geophysics, Eric Geocience, inc. for providing a license of *GAMLS*™ for this project, and the AASPI Consortium member companies for the support and funding for the AASPI software.

I would like to acknowledge the technical coaching and support from the following people: Rodrigo Bastidas (also for his support during my time at Marathon), Javier Perez, Luis Rodrigues, Dr. Eric Eslinger, Falene Pearson, and Brian Eslick. I would also like to thank the following students at OU for their assistance during the course of this project: Karelia La Marca, Austin McGlannan, Benjamin Slechta, Benmadi Milad, Lennon Infante-Paez, Barrett Cloud, and my friends in the IRC.

Finally, I would like to say thank you to my family and friends for their support throughout the course of my education, continued support during difficult periods, and words of encouragement.

TABLE OF CONTENTS

LIST OF FIGURES

LIST OF TABLES

ABSTRACT

The South Brae Field is located 166 miles off the coast of Aberdeen, Scotland in the UK sector of the North Sea. The Upper Jurassic Brae submarine channel-fan complex deposits are the primary hydrocarbon reservoirs in UK Blocks 16/07a and 16/07b. The field is composed of channelized silici-clastic slope-apron and fan deposits from high- to low-density debris flows, sandy and muddy turbidites, and hemipelagic settling. They were deposited during the Late Oxfordian to Middle Volgian. The Kimmeridge Clay Formation is a regionally-extensive, organic-rich, transgressive shale—deposited concurrently—that separates the Brae Formation from the overlying Cretaceous deposits and serves as the source rock and stratigraphic seal. The reservoir is trapped by the western escarpment of the South Viking Graben, which formed as a result of Permo-Triassic rifting and additional Middle to Late Jurassic rifting events.

The Brae formation is composed of seven main lithofacies including conglomerate, pebbly sandstone, sandstone, sandy siltstone, silty shale, shale, and calcite-cemented sandstone. Core descriptions, thin-section petrography, x-ray diffraction, and core plug measurements were used to understand the lithological, depositional, and petrophysical variations of the formation. Log-based, and seismic stratigraphic correlations were used to identify second-, third-, and fourth-order stratigraphic sequences. Thickness maps of the subunits within the Early to Middle Volgian – J66 – third-order sequence and spectral decomposition of the seismic volume aided the identification of depositional fairways within the upper part of the Brae Formation.

Electrofacies were generates using supervised multi-variate cluster analysis and artificial neural network classification models. The classifications showed overall accuracies around 90 percent. Facies proportion maps were constructed to understand their lateral distribution within the third-order sequence. Log-based and seismic stratigraphic interpretations of fourth-order

sequences within the J66 sequence helped to illustrate the internal distribution of the reservoir-quality facies (sandstones, pebbly sandstones, and conglomerates) within the depositional fairways. The lower subunit of the J66 system – the Ac subunit – is composed of laterally- and vertically-connected channel-fills and fans with a high abundance of thick calcite-cemented sandstone concretions that impede the flow of fluids within the reservoir. The Aa subunit – the upper part of the J66 sequence – primarily contains isolated channel-fills with a smaller amount of calcite concretions. Both subunits are composed of sandstone, pebbly sandstone, and conglomerate channel-fans and fans that were deposited after incision into muddy turbidite units that underlie them.

1. INTRODUCTION

1.1. Scope of Thesis

A majority of the energy consumed in the world is sourced from oil and natural gas extraction, a large percentage (>30%) of which is sourced from offshore sources (US Energy Information Administration, 2016). These projects are expensive when compared to most onshore developments. Spatially limited information for geological characterization is often all that is available for industrial and academic purposes. This study uses the example of a North Sea field to continue to make the case for generating a lot of valuable information from limited datasets that can be acquired from offshore fields.

Deposits from shallow marine environments, their associated sedimentary processes, as well as the resulting lithofacies have been extensively described in geological literature (Reading and Richards,1991; Shanmugam, 2016). Reservoir characterization is best carried out with access to outcrop exposures which show textural, depositional, and lithological variations of the same or similar facies that occur in the reservoir. Outcrops of reservoir analogs that require characterization are sometimes inaccessible due to remoteness and must be characterized only with the information available. Subsurface drill core can provide valuable insights into the nature of reservoir rocks. However, core is limited by the size of the wellbore which limits the spatial information that can be gathered from it. Incorporating machine-learning classification techniques to tie wireline log responses to core can aid in reducing lateral uncertainty in the subsurface reservoir characterization process (Rogers et al., 1992).

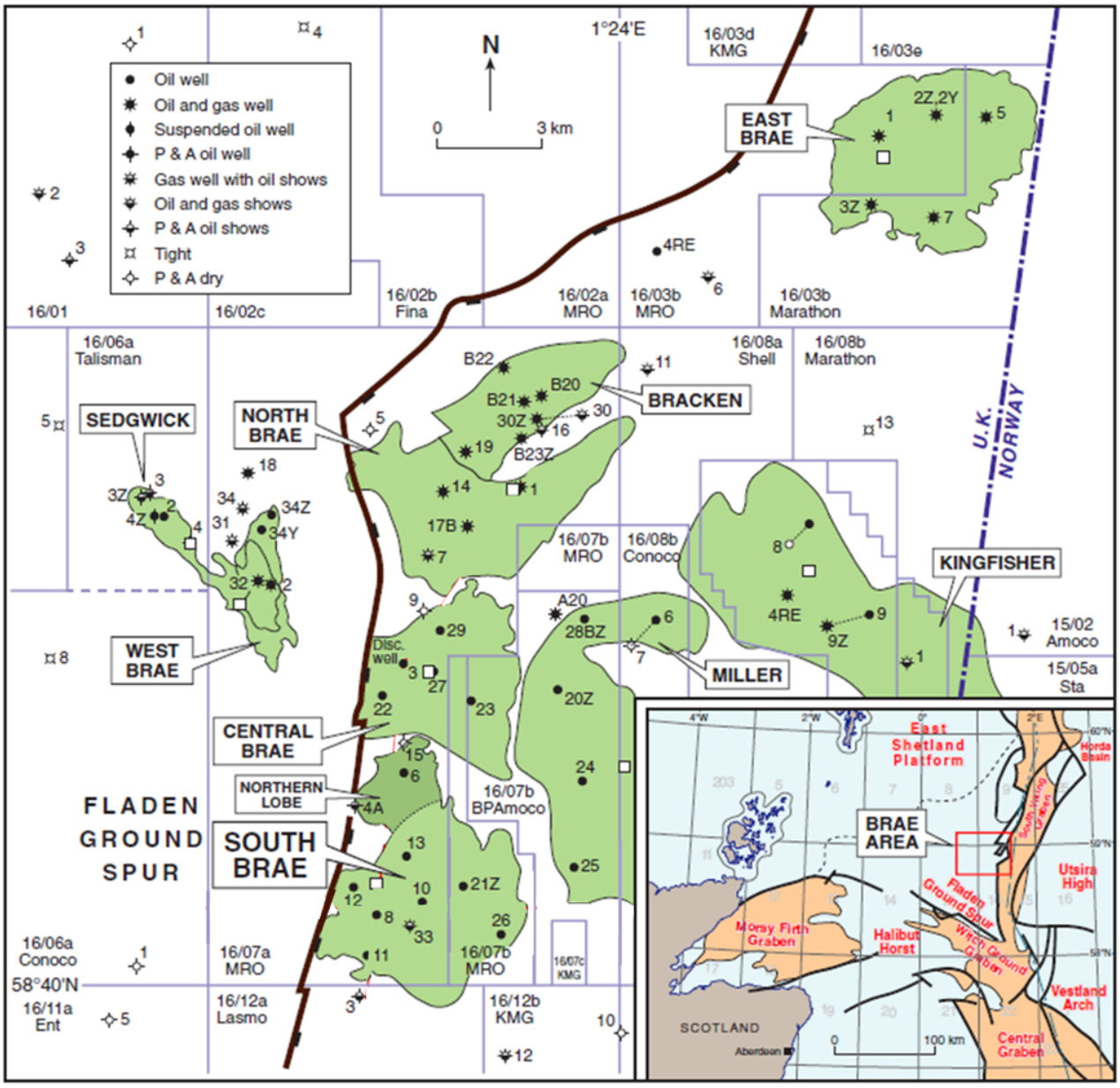

Figure 1: Location of the South Brae Field. Inset map the geological provinces of the North Sea (modified from Fletcher, 2003).

The principal contribution of this study is the clarification of the petrophysical and lithofacies relationship of the Brae Formation in the J66 sequence within the South Brae Field, North Sea. This was achieved by improving the understanding of the lithofacies and their associated petrophysical properties using the techniques described in this thesis. The integration

of core and thin section analyses to identify the lithofacies present along with core- and log-based lithofacies predictions and seismic interpretation help to explain, within a stratigraphic framework, the high reservoir quality observed within the sandstone facies of the Brae Formation.

1.2. Previous Research

The Brae Formation, located on the southwestern part of the South Viking Graben in the North Sea, is interpreted to be a set of slope-apron fans deposited along a faulted scarp margin. It is the primary reservoir within the hydrocarbon fields in the Brae area. The major controls on the reservoir quality are fault-related fracture cementation, diagenetic alteration, and lithofacies (Harms et al., 1981; Stow et al., 1982). Understanding the relative magnitude of these factors is important to adequately characterize this reservoir.

Through the use of drill core, Stow et al. (1982) identified three main sediment facies groups within the Brae Formation: the mudstone group, the sandstone group, and the conglomerate group. The mudstone group is comprised of dark interbedded mudstones and light interbedded fine- and very fine-grained sandstones. The sandstone group is comprised of thin- and medium- to thick-bedded sandstones with thin internal laminations and pebble-sized clasts. The conglomerate group is described as containing breccias and clast- and matrix-supported pebbly conglomerates.

Using genetic stratigraphic sequencing and palynology, Partington et al. (1993) subdivided the Brae Formation into three key sequences, the end of each sequence corresponding to a Tectonically Enhanced Maximum Flooding Surface (TEMFS). A TEMFS is characteristic of

changing basinfloor paleogeography due to tectonic activity. In a rift basin, a singular condensed section is present in the footwall and stacked retrogradational parasequences of the condensed sections are present within the basin due to continued flooding. The J50-J62 sequence represents the Late Oxfordian to Early Kimmeridgian and is correlated to the Eudoxus TEMFS. The J63-J66 sequence represents the Mid-Late Kimmeridgian and is correlated to the Fittoni TEMFS. The J71-J72 sequence represents the Early Portlandian and is correlated to the Anguiformis TEMFS (Fig. 2).

Turner et al. (1987 and 1991), Reading and Richards (1991), and Fraser et al. (2003) interpret the Brae Formation as a gravel-rich system deposited by multiple point-source ramps and slope aprons in the south and by a submarine single point-source system in the north. They describe up to 1-km wide channel fills that extend up to 5-km into the basin from different sources along the 20-km fault scarp on the west.

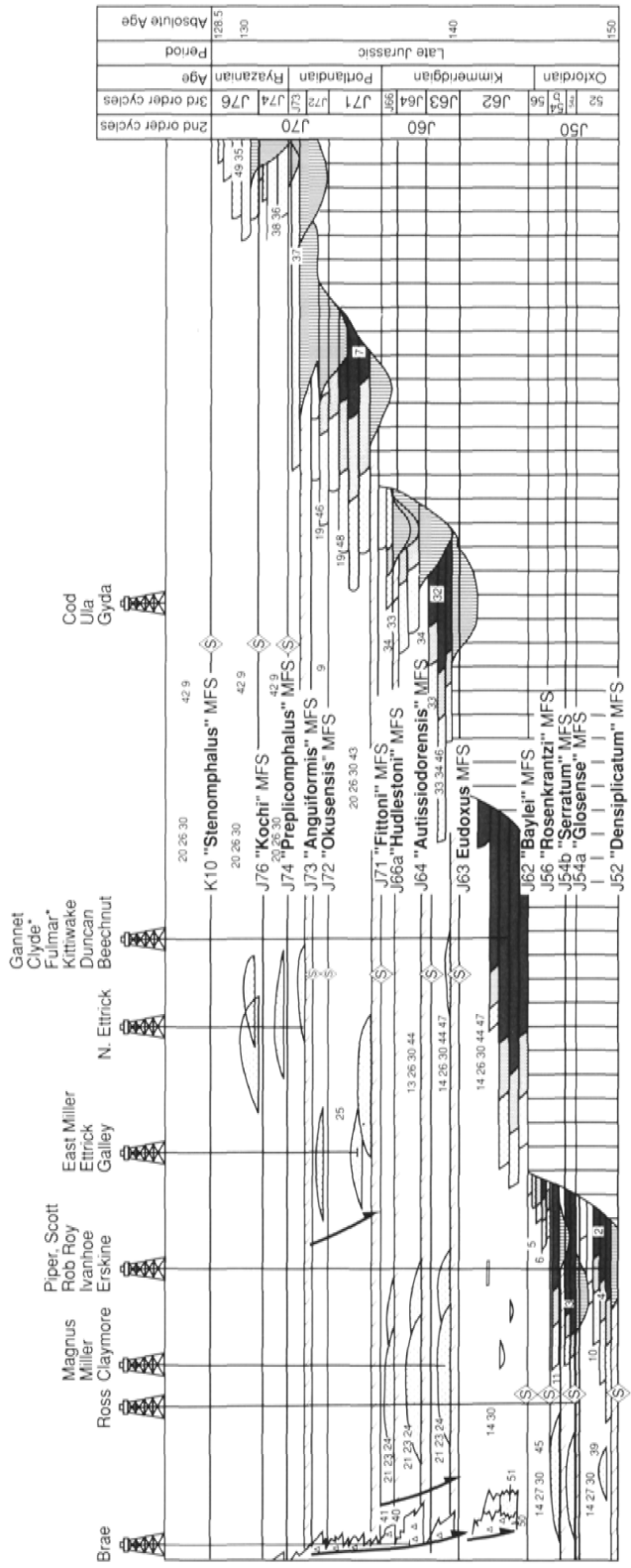

Figure 2: Oxfordian to Ryazanian sequence stratigraphy (Partington et al., 1993).

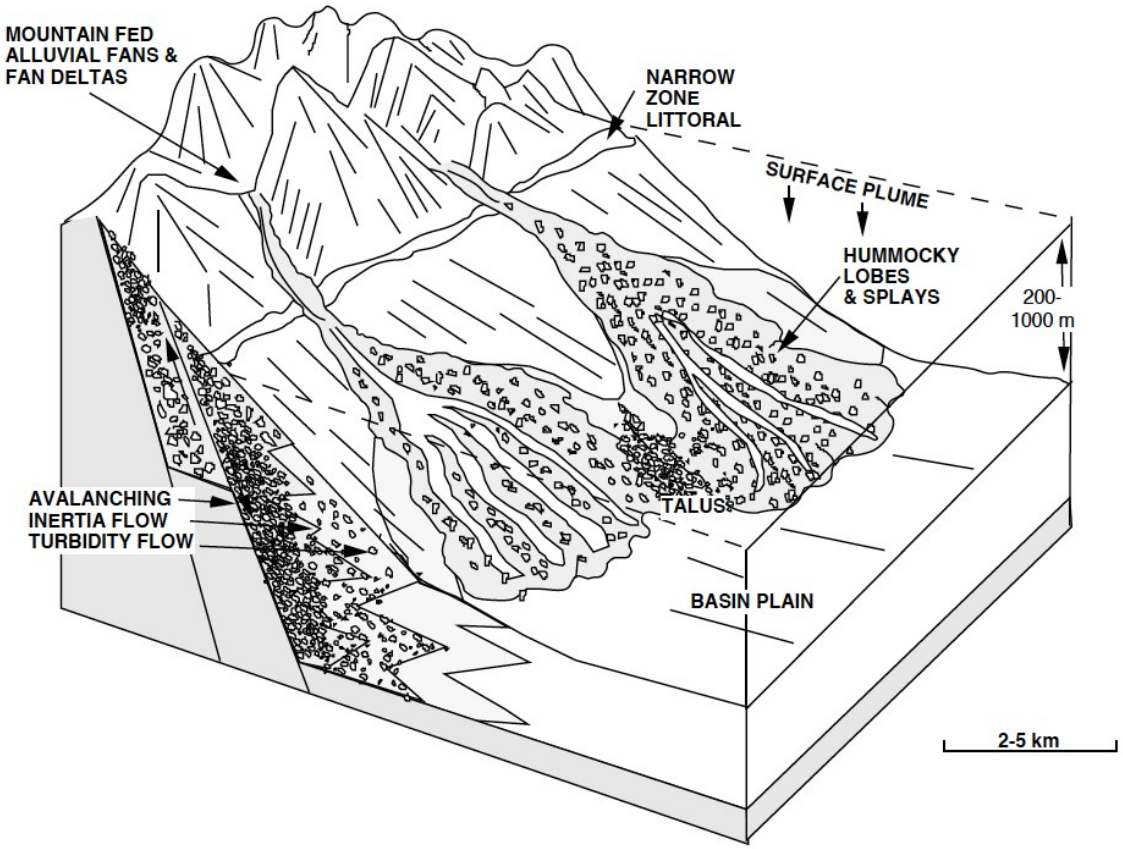

Figure 3: Multiple point-source gravel-rich ramp depositional model (Reading and Richards, 1991).

Harms et al. (1981) and Stow et al. (1982) interpret the depositional environment of the Brae Formation as shallow marine based upon core description. They observed pelagic and benthonic flora and fauna, as well as terrestrial spores, pollen, and debris. They also observed small-scale sedimentary features such as ripples and parallel laminations, as well as an absence of bioturbation, indicating unperturbed deposition primarily beneath the shallow- to storm-wave base.

Cherry (1993) incorporated core descriptions, well logs, and seismic in identifying the relationships between the structure of the Viking Graben and the sedimentary processes that

deposited the Brae Formation. It is interpreted as a Mutti (1985) Type II proximal submarine fan turbidite deposit that is affected by tectonic uplift. The location of faults in relation to the Western Margin Fault of the South Viking Graben, as the sediment pathways follow surface fault lines that are preferentially eroded and determines the pathway into the basin (Fig. 3). Seven (7) major lithofacies are identified in core. They were deposited by high to low density turbidity currents, debris flows, hyperpycnal flows, and hemipelagic settling.

McLaughlin (1992), through isotope analysis of core samples, observed an abundance of authigenic carbonate and quartz cements interspersed within the South Brae fan complex. The cementation was caused by paleohydrological factors. Shallow water burial allowed for meteoric water to penetrate pore spaces leading to carbonate concretion growth from the Late Jurassic to Early Paleocene. A change in hydrology caused by a pressure solution of warm basin waters and saline pore fluids led to the precipitation of authigenic quartz. Subsequent cementation occurred as the fluids were forced out of the pore spaces by compaction.

2. GEOLOGICAL CONTEXT

2.1. Regional Geology

The South Viking Graben is the southernmost portion of the Viking Graben, a north-northeast trending rift basin in the North Sea. It is bounded on its western margin by the Fladen Ground Spur, the Utsira high to the east, the Central Viking Graben to the north, and the Fisher Bank basin to the south (Figs. 1 & 4) (Zanella and Coward, 2003). The break-up of Pangea during the Permo-Triassic led to the formation of the complex triple-junction that created three (3) rift basins in the North Sea: the Viking Graben, Central Graben, and Witch Ground Graben-Moray Firth Basin (Fig. 5) (Thomas and Coward, 1996). The South Viking Graben is a westward-dipping half-graben that gently slopes from the Utsira High in the east, through tilted basement fault blocks, into a high-displacement (> 4 km) graben-margin fault zone on the west that separates pre- and syn-rift sediments from the basement (Jackson et al., 2011).

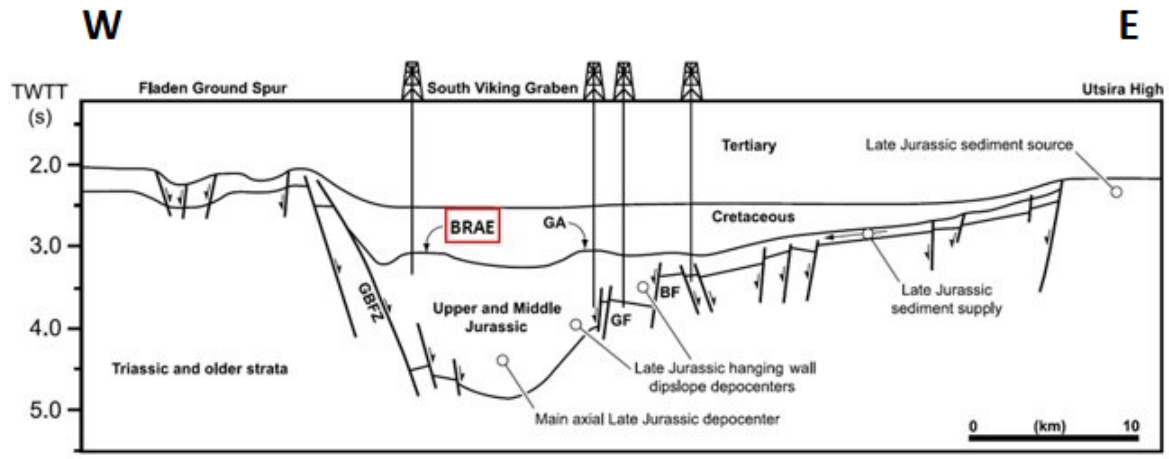

Figure 4: Schematic cross-section of the South Viking Graben (modified from Jackson et al., 2011).

The Viking Graben was formed by a series of rifting events which started in the Late Carboniferous-Early Permian and ceased in the Paleocene (McLaughlin, 1992). Early Permian NW-SE trending extensional faults are evidence of the first phase of rifting. The associated subsidence led to the creation of flexural salt basins where the carbonates and evaporites of the Zechstein Group precipitated after the deposition of the Rotliegende dune sands in the Late Permian (Ziegler, 1975; Thomas and Coward, 1994). Rifting in the Triassic occurred due to the localized effects of crustal extension (Glennie, 1984). The Zechstein Sea regressed towards the Arctic as the Tethys rift system began to develop. This rift formed the dominant structural features that allowed for significant terrestrial sediment input into the basin during the Triassic. Footwall uplift caused the deposition of the Skagerrak Formation (Ziegler, 1975).

The Forties Volcanic Province occurs at the junction of the three (3) North Sea grabens. The doming and subsequent erosion of the volcanoes is the source of Lower to Middle Jurassic sedimentation (Smith and Ritchie, 1993). Sequence stratigraphic coastal and marine onlap of Lower Jurassic sediments are evidence of doming and deflation. Active rifting continued in the Middle Jurassic. The deltaic and delta-front deposits of the Sleipner and Hugin Formations were deposited during the associated regression. The distal muds and sands of the Heather Formation complete the Middle Jurassic deposits (Thomas and Coward, 1996).

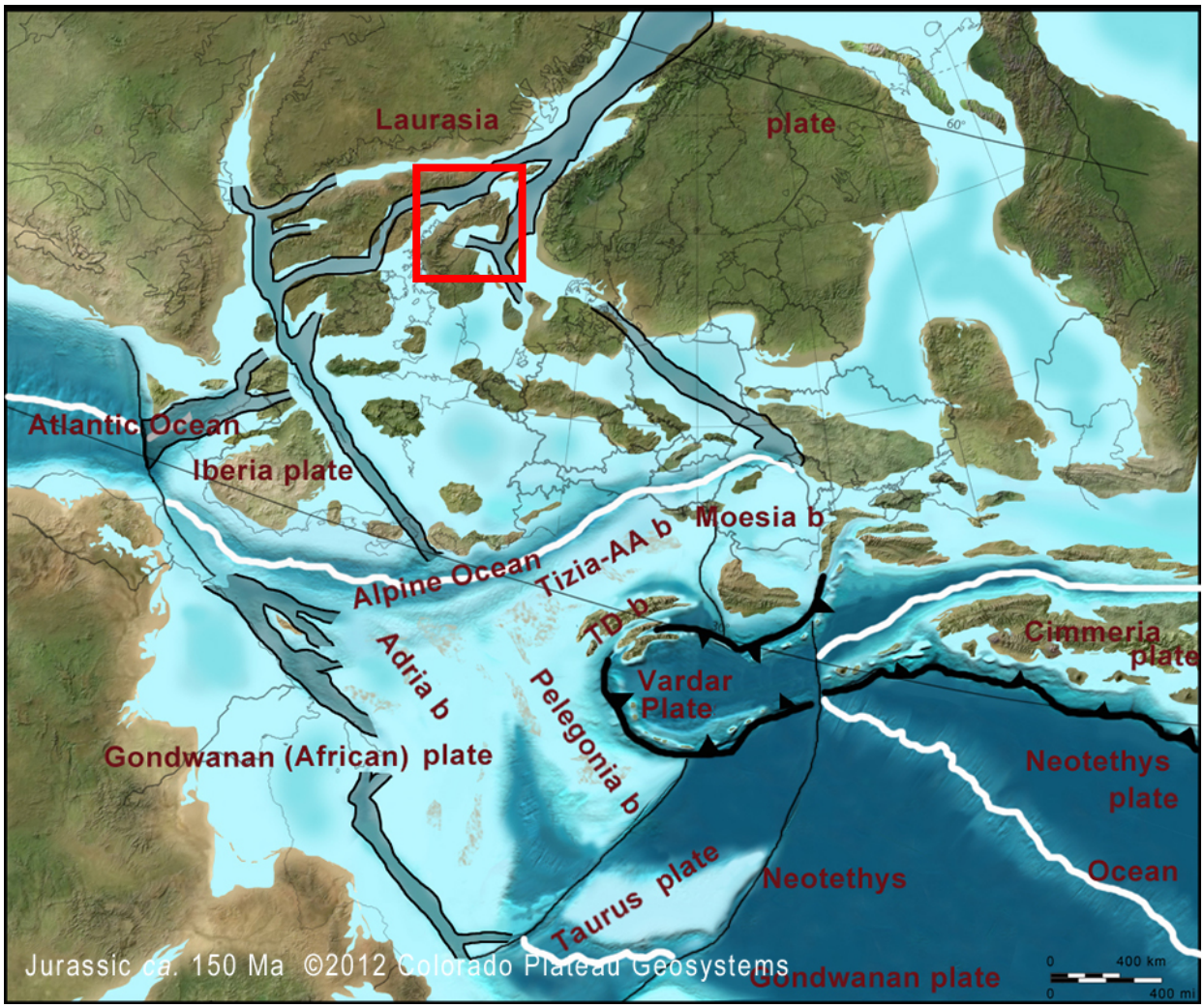

Figure 5: Paleogeographic map of the Upper Jurassic. Red box indicates approximate location of the South Viking Graben (Blakey, 2012).

Large-scale extension in the Late Jurassic saw dip-slip movement along the western margin fault system of the South Viking Graben form the present half-graben structure. Fault movement started in the Callovian and ended in the Early Cretaceous. This allowed for nearshore and marine deposition. Gravel-dominated fan systems of the Brae Formation deposited a thick (> 1 km) column of silici-clastic sediments. The Kimmeridge Clay Formation was deposited simultaneously as continued subsidence allowed for hyperpycnal flows and hemipelagic sedimentation distal to the coastal highland provenance in the West. Inversion occurred in the

Late Jurassic-Early Cretaceous due to fold tightening associated with concentration of the underlying salt cores of the Zechstein Group (Turner et al., 1987; Ziegler, 1990 McClure and Brown, 1992; Thomas and Coward, 1996).

2.2. Brae Formation

The Brae Formation was deposited by a series of eastward flowing, gravel-dominated, submarine fan systems as the South, East, Central, and North Brae fan complexes. Late Jurassic sedimentation reached a maximum thickness of 2,500 feet within the Brae Area. The Brae Formation is overlain and underlain by the Kimmeridge Clay Formation (Fig. 6). It was deposited as the rifting reached peak intensity and it serves as the regional source, stratigraphic trap, and seal for the Brae Formation. The Brae Formation is comprised of three broad lithofacies: sand-matrix conglomerates and mud-matrix breccias represent proximal slope-apron fan deposition, coarse to fine grained sandstones deposited in turbidite channels and fans form the remainder of the reservoir rock; thinly-bedded and laminated very fine-grained sandstones, siltstones, and shales form the distal inter-channel and channel-margin deposits. Sedimentation and structural deformation after the deposition of the Brae Formation led to the formation of anticlines that serve as the structural trap for the field (Fletcher, 2003; Gautier, 2005; Stow et al., 1982; Turner et al., 1987; Turner, 2013).

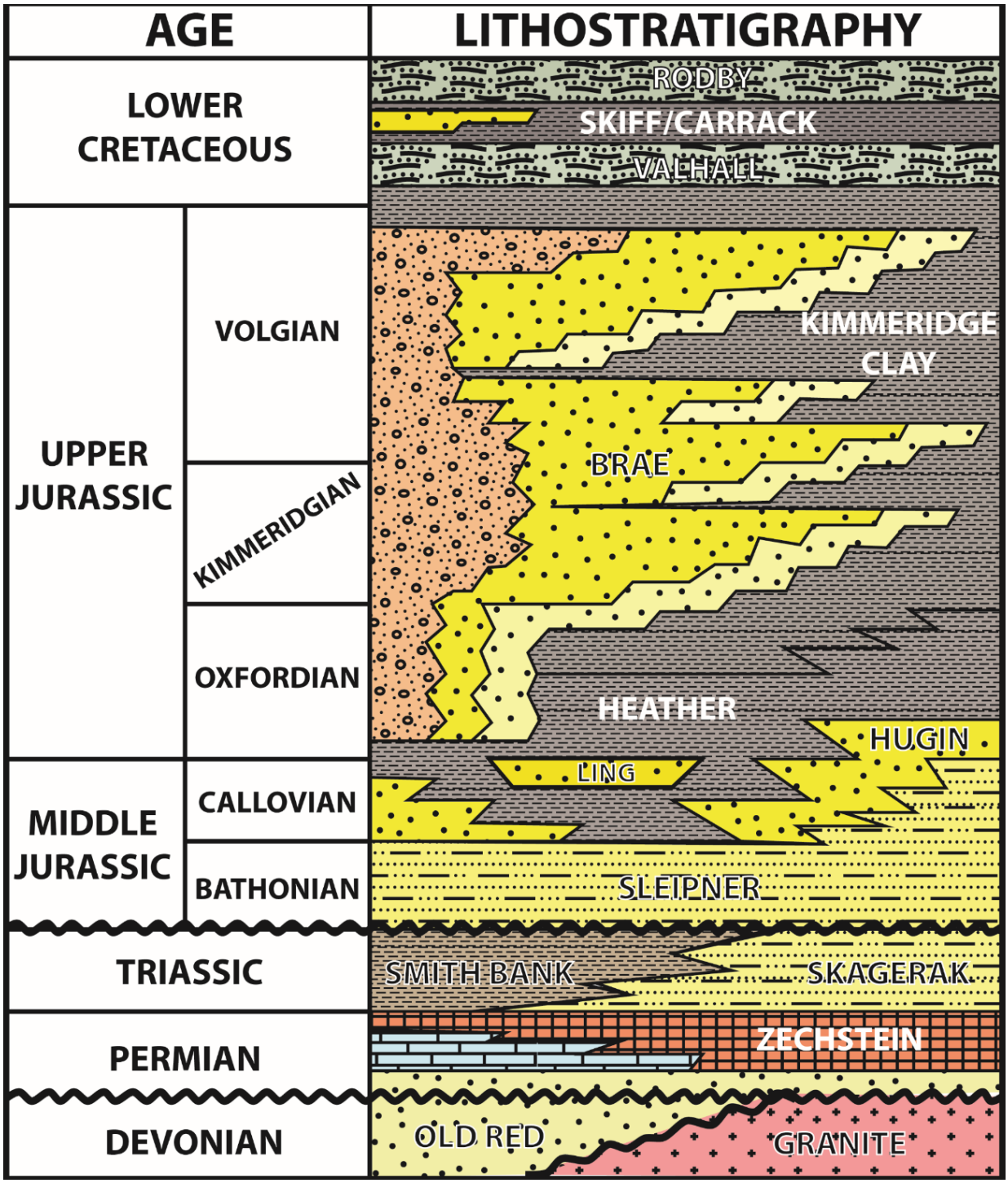

Figure 6: Pre-Cretaceous stratigraphic chart of the Brae area (modified from Turner, 2013).

The Brae Formation was deposited during the Upper Jurassic from the Late Oxfordian to Mid-Volgian (147.5 Ma to 133.5 Ma) (Fraser et al., 2003; Partington et al., 1993). Partington et al. (1993) proposed a shallow marine depositional environment which experienced a continued increase in accommodation space as tectonic subsidence occurred in the Late Jurassic. Syn-rift deposition, where subsidence exceeded sediment input, led to a change from coarse alluvial fan to slope apron fans in the Early Kimmeridgian. This first phase of sedimentation (Late Oxfordian to Mid-Kimmeridgian) saw the deposition of conglomerate-rich slope apron fan deposits. The second phase of sedimentation (Mid-Kimmeridgian to Mid-Volgian) occurred as a reduction in relief of the Fladen Ground Spur led to the deposition of sand-rich basin floor fans (Fig. 7) (Turner et al., 1987; Fraser et al., 2003).

The Brae Formation occurs in five (5) distinct syn-rift sequence stratigraphic units: (1) The J54 and J56 sequences were deposited during the Late Oxfordian to Early Kimmeridgian. These units are defined by the 144 Ma *Baylei* Maximum Flooding Surface (MFS). This represents a shallow marine fan delta to a lowstand submarine fan. (2) The J62 sequence was deposited during the Early to Mid-Kimmeridgian. This unit is defined by the 142 Ma *Eudoxus* MFS. This flooding event occurred due to tectonic subsidence and a rise in relative sea level. This represents a multiple point-source slope apron fan depositional setting. (3) The J63 and J64 sequences were deposited during the Late Kimmeridgian to Early Volgian. This unit is defined by the 138 Ma *Huddlestoni* MFS. This represents coarse alluvial fan deposition to alluvial fan delta and, eventually, slope apron fan deposition as sea level begins to fall. (4) The J66 sequence was deposited during the Early to Mid-Volgian. This unit is defined by the 136 Ma *Fittoni* MFS. This represents lowstand aggradational basin floor sands. Subsequently, transgressive and highstand shallow marine deposition occurred. (5) The J71 and J72 sequences were deposited during the Mid-Volgian. These units are defined by the 133.5 Ma *Anguiformis* MFS. This

represents sea level rise associated with rifting and a fall in sea level that caused the deposition of aggradational basin floor fans (Fig. 2) (Partington et al., 1993; Partington et al., 1993).

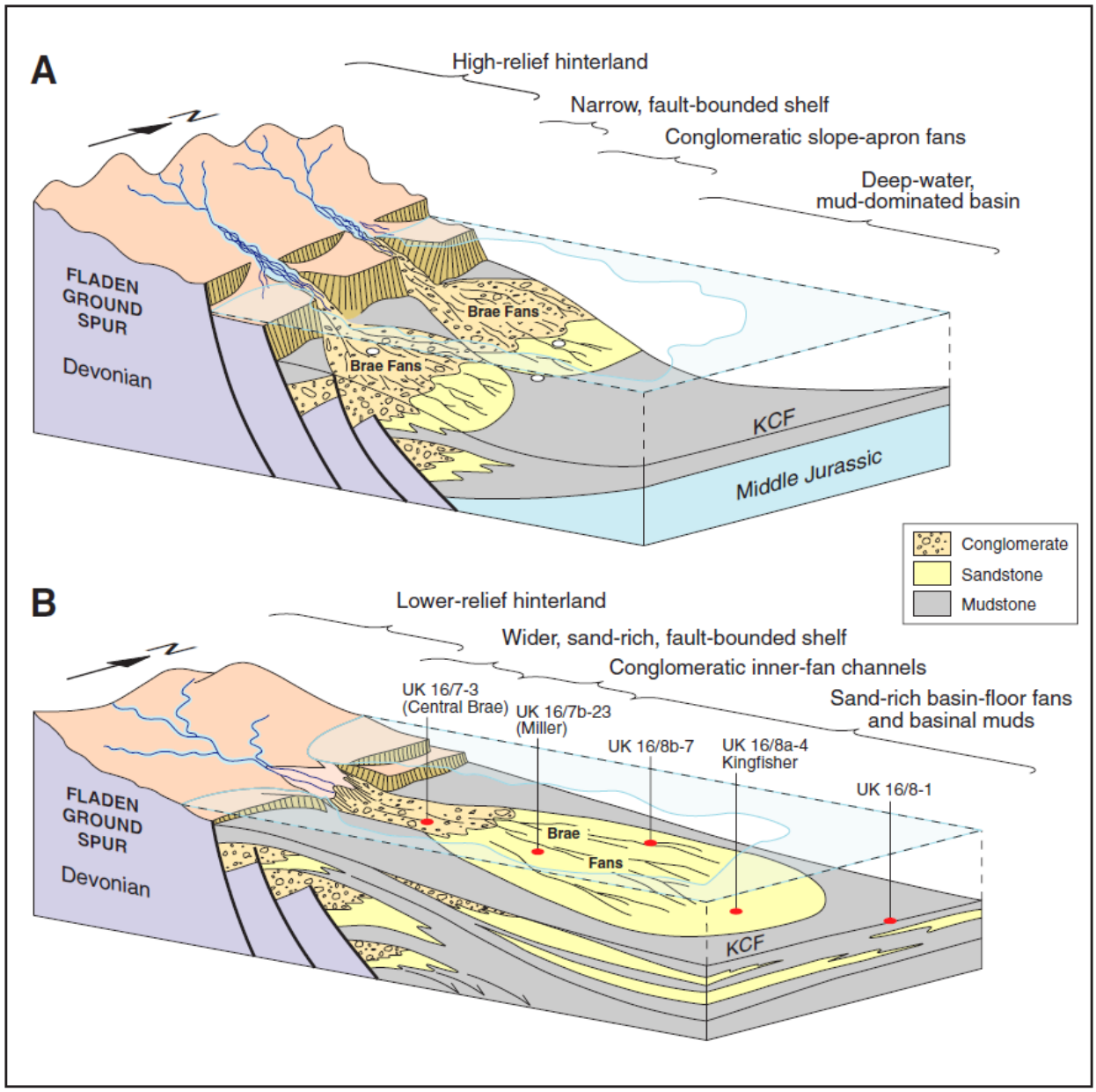

Figure 7: Generalized (A) early- and (B) late-stage depositional models of the Brae Formation (Fraser et al., 2003).

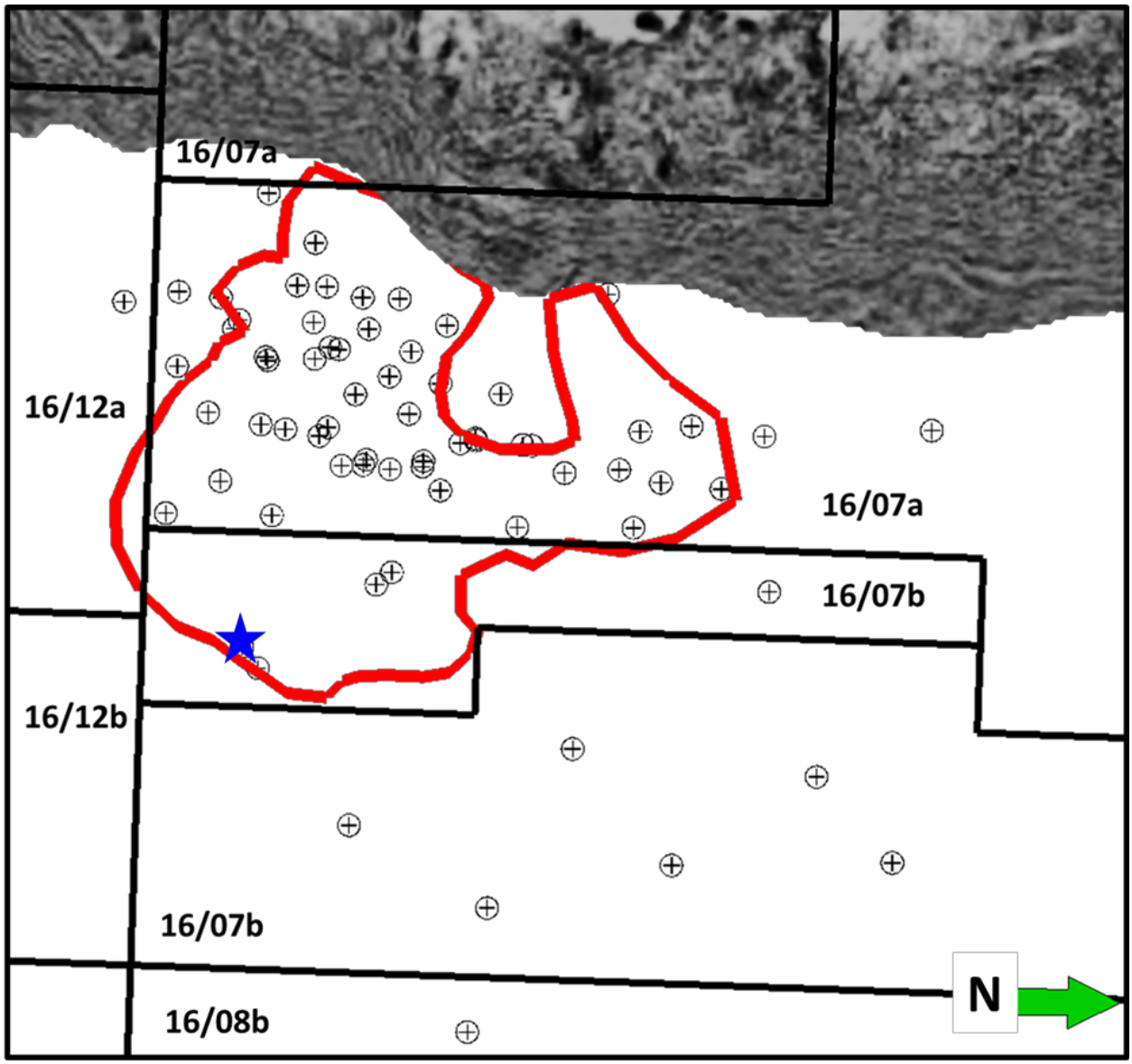

Figure 8: Base map of the study area. The South Brae field limit is outlined in red. Cored well is marked by blue star.

2.3. Area of Study

Regionally, the South Brae Field is located at the Southern portion of the South Viking Graben, close to the Central and Witch Ground Grabens. Geographically, it is located 166 miles northeast of the coast of Aberdeen—in 370 feet of water—in the British sector of the North Sea (Fig. 1). The Brae Formation, the producing reservoir interval in the field, is buried to depths in

excess of 12,000 feet TVDSS. The field covers about 10 square miles spanning UK blocks 16/07a and 16/07b. It is operated by Marathon Oil UK (Fig. 8) (Roberts, 1991; Fletcher, 2003). 'Brae' is a Scottish word for steep bank or hillside.

Data for this study was provided by Marathon Oil UK. A 1026 km^2 pre-stack time migrated 3D seismic volume covering UK blocks 16/03e, 16/07a, 16/07b, 16/08a, 16/08b, and 16/08c was used for seismic interpretation. Sixty-eight (68) wireline logs from blocks 16/07a, 16/07b, 16/08b, and 16/12a were available for stratigraphic correlations and petrophysical characterization (Fig. 8). A 410-foot core section from Well O was available for core characterization.

3. METHODOLOGY

3.1. Lithofacies Identification

3.1.1. Core Analyses

The lithologies penetrated by Well O were initially identified from core descriptions provided by Marathon Oil. This core description included lithology, grain type, grain size, sedimentary structures, and palynofacies. The core was re-described by me for verification prior to the interpretation of the local depositional environment of Well O. The core was divided into lithofacies based on the core description (Table 2).

Additionally, results from core plug testing conducted by Redwood Corex Services Ltd. and Core Laboratories UK Ltd. were made available for this study. The core plugs are 1-inch diameter. The sampling interval is one (1) foot for plugs parallel to the apparent bedding plane and five (5) feet for plugs perpendicular to the apparent bedding plane. Core plug samples were collected at 361 unique depths. The core plug analysis consisted of (vertical and horizontal) nitrogen permeability, helium porosity, and grain density measurements. Grain densities and porosities were calculated after mercury displacement of helium. Permeabilities were measured at a pressure of 180 psi with nitrogen as the flowing fluid.

3.1.2. Thin Section Analysis

Thin sections were cut for petrographic analysis – fifteen (15) thin-section samples in total. They were made by National Petrographic Service, Inc. Each thin section was sized 27 mm by 48 mm. Epoxy resin impregnation and carbonate staining were not included. The samples were analyzed using a Zeiss Imager Z1 petrographic microscope. The objective of this analysis

was the observation of any heterogeneity present within each facies which cannot be observed from conventional core observation.

3.1.3. Bulk Mineralogical Analysis

Mineralogy of the Well O core was analyzed using x-ray diffraction (XRD). This geochemical analysis was conducted at the Genesis GeoChem Lab by Paladin Geological Services. The analysis was conducted using the *Rigaku MiniFlex600*. Sixteen (16) samples representing the major facies present in the core were analyzed (Fig. 9). The bulk mineralogy (in volume percent) of the following components were determined: quartz, calcite, dolomite, albite, anorthite, orthoclase, muscovite, pyrite, and clays.

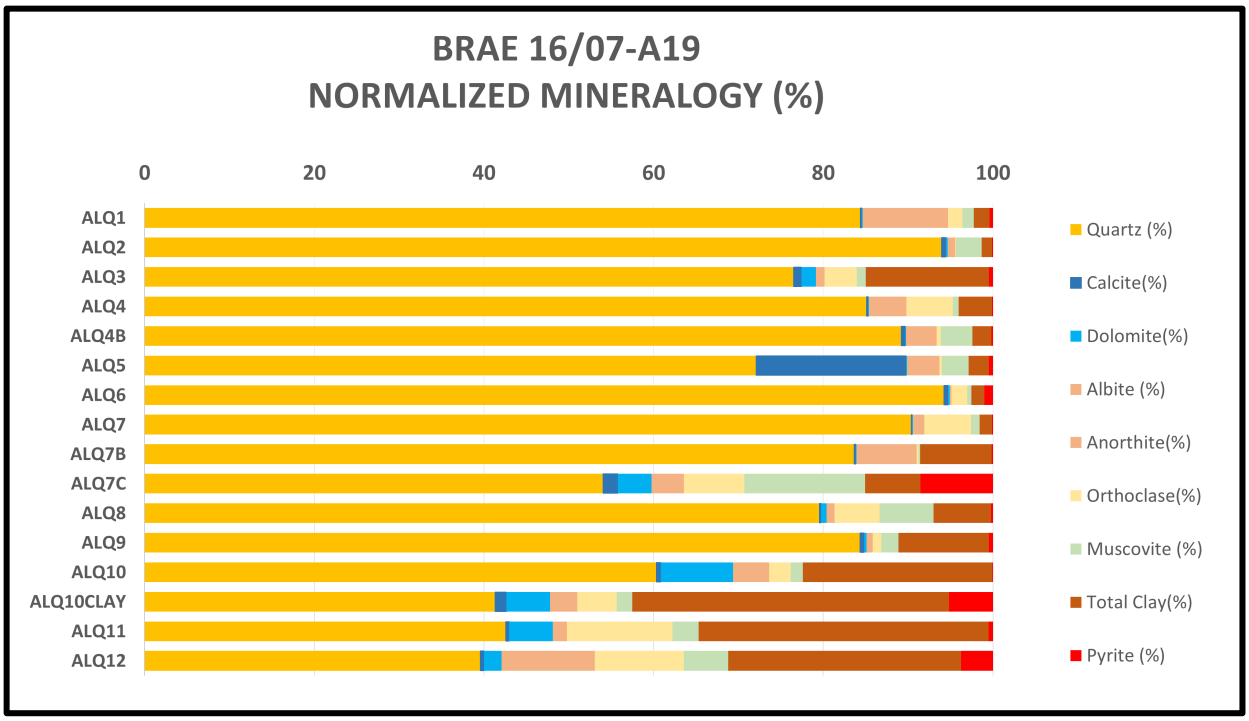

Figure 9: Bulk mineralogy volumes from XRD analysis.

3.2. Stratigraphic Framework

3.2.1. Well-log Correlation

The Brae formation was correlated on wireline logs by subdividing it into Four (4) members – A, B, C, and D – representing the J66, J64, J63, and J62 sequences respectively. Zone A, the interval of focus in this study, is equivalent to the J66 sequence described by Partington et al. (1993). Each member is further divided into four (4) subunits – a, b, c, and d. Alternate subunits of mudstones separate the units and make them fairly easy to correlate (Turner et al., 2018). Gamma ray logs were used for correlation purposes. Smoothened gamma ray derivative logs aided stratigraphic correlation across the field. This process, also known as derivative trend analysis (DTA), has been successfully implemented in a study by Wethington (2017). *Techlog*™ was used to smooth the gamma ray logs within the desired vertical window of interest and calculating the derivative of the resulting curve. The resulting curve highlights intervals on the gamma ray curve where major changes in process energy have occurred. These highlighted inflections in process energy correspond to the subunits of each of the Brae Formation members (alternating sandy/conglomeratic and mudstone subunits). This process allowed for highlighting important changes in process energy where the log responses were relatively muted (Fig. 24). Formation tops were identified from some previously interpreted logs and prior knowledge of the stratigraphy of the area (McClaughlin, 1992; Turner, 2013; Turner et al., 2018).

3.2.2. Seismic Interpretation

Seismic reflectors were used to correlate the Kimmeridge Clay Formation and the J66 sequence (the A member of the Brae Formation) across the field after well log correlations were completed (Vail, 1987). The interpretations were conducted by interpreting the top (J66) and

base (J64) reflectors from tied wells to inline and crossline sections of the volume to form a grid of mapped reflectors (Fig. 10). The mapped seismic reflectors were converted from time to depth units with an approximate velocity for all the overlying sediments. The depth-converted surfaces were used to generate thickness maps, which were subsequently used for facies mapping. The western margin fault separating the pre- and syn-rift sediments from the basement is interpreted on seismic. The basement rock to the west of the field appears almost seismically transparent relative to the reflectors representing the pre-rift deposits. However, defining the exact boundary was difficult in places due to the similarly "transparent" adjacent expression of some older pre-rift, Middle Jurassic deposits.

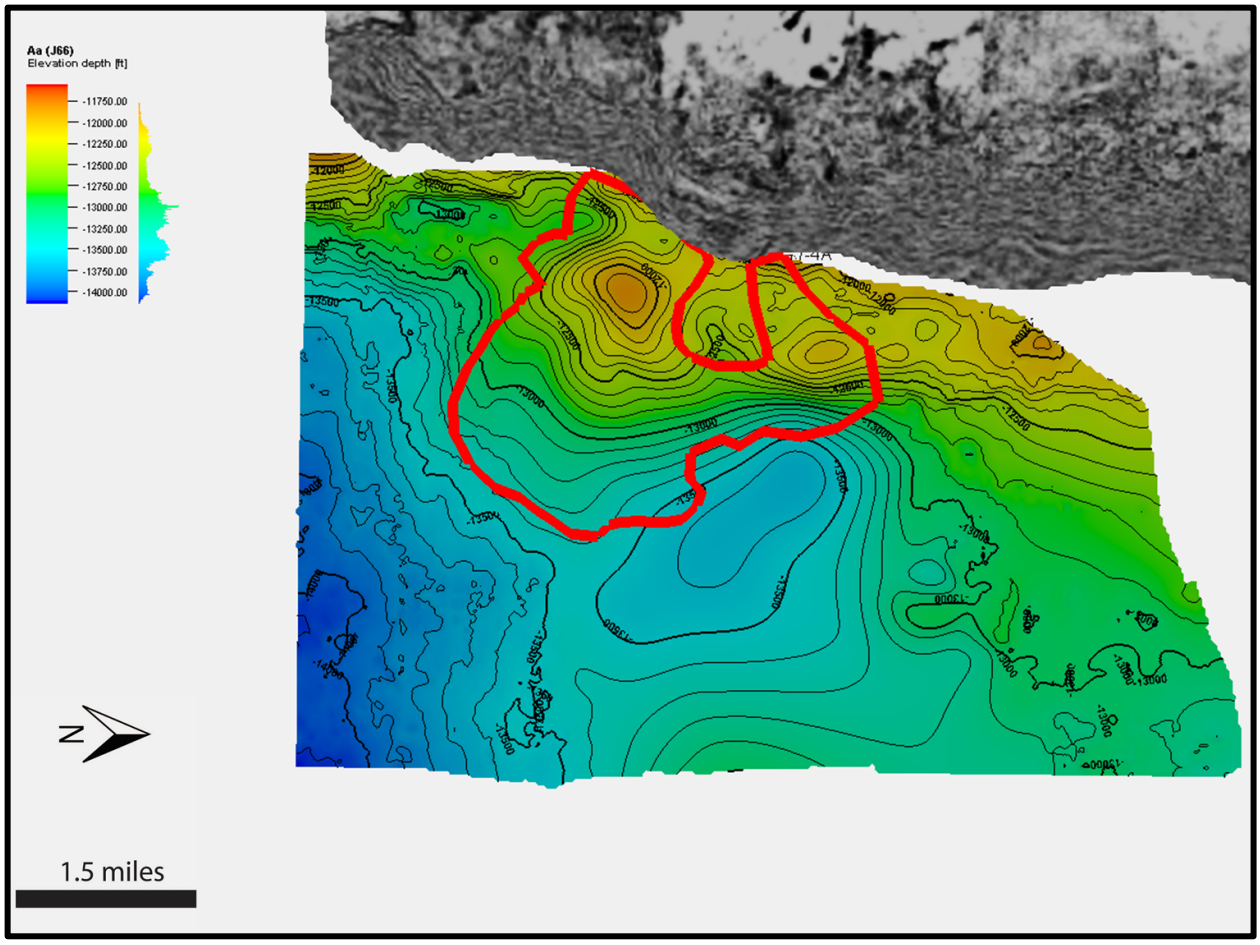

Figure 10: Depth structure map of the top of the J66 sequence. South Brae is outlined in red.

Seismic attribute analysis was conducted using AASPI^{TM} software in order to identify channels (Fig. 11) within the relatively homogeneous Brae Formation. Spectral decomposition of the seismic volume was done to identify the channel fairways within the South Brae Field. The peak frequency range of the reflectors within the channel intervals was identified by observing the frequency spectrum. The voice components of the minimum, intermediate, and maximum peak frequencies were color blended (red, green, and blue) in order to identify the channel fairways within the field, and delineate some internal heterogeneities.

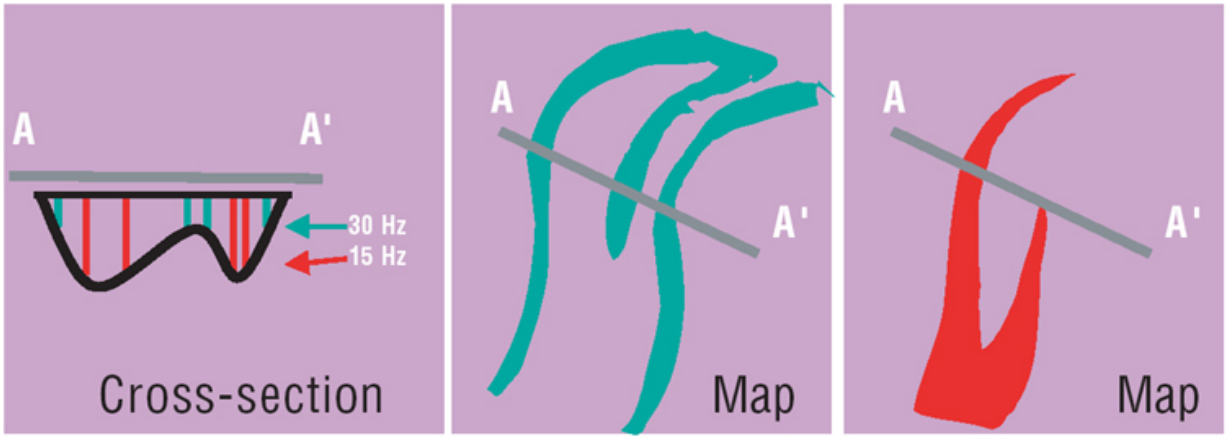

Figure 11: Channel identification using spectral decomposition (Laughlin et.al., 2003).

3.3. Electrofacies Classification

3.3.1. Wireline Log-Conditioning

In this study, wireline data from each well was split into two sets before data combinations – original and calculated – could be determined for supervised facies classification procedure (Table 1). The "original" wireline data included gamma ray (GR), bulk density (DEN), neutron porosity (NEU), photoelectric factor (PEF), and compressional velocity (Vp) logs. The "calculated" data included shale volume (VShale), corrected density porosity

(PHID.c), corrected neutron porosity (PHIN.c), photoelectric factor (PEF), and acoustic impedance (AI) logs. The calculated logs, except PEF, are modified versions of the original log sets. They are calculated as shown below:

1. VShale = (GR – GR.min)/(GR.shale – GR.min)
2. PHID.c = PHID – (VShale * PHID.shale)
    a. PHID = (DEN – DEN.matrix)/(DEN.fluid – DEN.matrix)
3. PHIN.c = NEU – (VShale * NEU.shale)
4. AI = Vp * DEN

The calculated data combinations were used to test the effects of log corrections on the precision of each classification technique. VShale, PHID.c, and PHIN.c – theoretically – correct for shale effects. AI accounts for the effects of bulk density, thus, reducing some of the noise present in the Vp log. The PEF log was left uncorrected as it responds to the mineralogy of the rock matrix. Permeability was not used as an input for classification, as it could only be empirically derived from porosity. Though, this empirical relationship yields a very strong correlation.

Original			Calculated	
O-1	GR, DEN, NEU		C-1	VShale, PHID.c, PHIN.c
O-2	GR, DEN, NEU, PEF		C-2	VShale, PHID.c, PHIN.c, PEF
O-3	GR, DEN, NEU, Vp		C-3	VShale, PHID.c, PHIN.c, AI
O-4	GR, DEN, NEU, PEF, Vp		C-4	VShale, PHID.c, PHIN.c, PEF, AI

Table 1: Log combinations used for electrofacies classification.

3.3.2. Multi-variate Clustering Analysis (MVCA)

Supervised multi-variate clustering analysis was conducted with *GAMLS*™ (Geologic Analysis via Maximum Likelihood System™). This method allows for prediction of lithofacies and has been used with success in previous studies focused in numerous depositional environments (Gonzalez et al., 2007; Gonzalez et al., 2007; Slatt et al., 2009; Vallejo, 2010; Eslinger and Everett, 2012). This process is a Probabilistic Clustering Procedure (PCP). Multiple wireline logs are plotted to identify clusters of data samples with similar log responses (Fig. 12). Data points within clusters are probabilistically assigned to modes (rock types). Each mode assignment is made by its Mode Probability Assignment (MPA). A continuous probability from 0 (absent) to 1.0 (present) determines how probable it is that a data sample within a cluster is representative of a mode (rock type). Each data point is assigned an MPA for each rock type possible, and the sum of all MPAs for every data sample is 1.0. Thus, the data sample is assigned to the rock type based on the probability threshold for a rock type as defined by the user. The data ranges for each wireline log, when clustered, can then be fit to a new – and similar – dataset in order to predict the rock types present in those wireline log datasets (Eric Geoscience, inc., 2000).

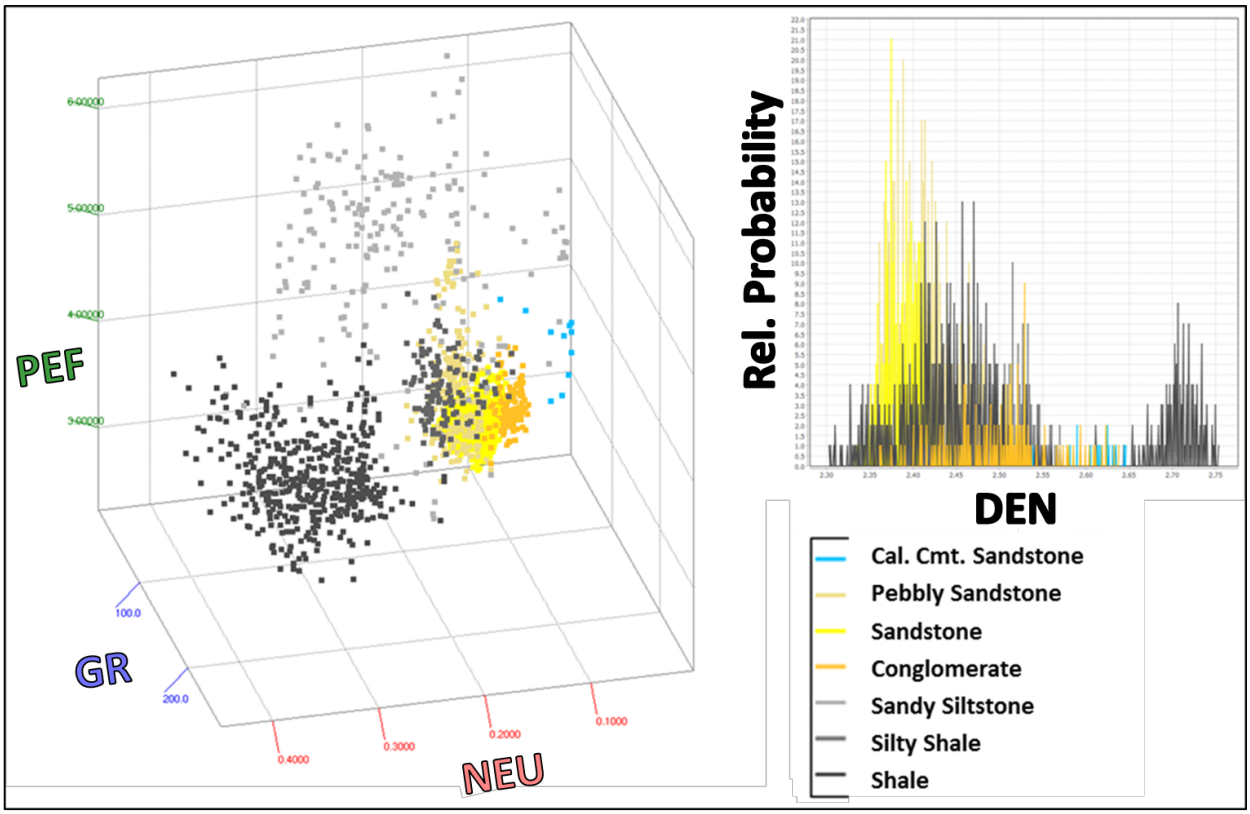

Figure 12: 3D cross-plot (right) of 3 wireline logs. Electrofacies plot as point clouds (clusters). Relative probability of each facies per input log is used to predict electrofacies in other wells. The relative distribution of probabilities of DEN per electrofacies (left).

The MVCA engine in *GAMLS*™ operates using a maximum likelihood artificial neural system. This classification technique is suited to datasets that have complex (non-linear) classification boundaries – mineralogically similar facies in this case. The maximum likelihood system classifies electrofacies using clusters and cluster boundaries determined using the Cramer-Rao theorem. The size and position of clusters are determined using probability density functions (PDF). PDFs are calculated with consideration for the number of observations and classes present. These conditions allow for clusters with overlapping boundaries (Perlovsky, 1988; Perlovsky and McManus, 1991).

3.3.3. Artificial Neural Network (ANN)

Artificial neural network (ANN) is another facies classification method used in this study. Supervised ANN facies predictions were conducted in *Petrel*™. It operates similarly to the biological neural networks present in mammalian brains. This method is a much simpler process than what occurs in a mammalian brain and it has been employed in numerous geological studies (Rogers et al., 1992). It operates with a forward-feeding, backpropagating process. Three (3) layers – input, hidden, and output – handle the data during this process (Fig. 13). The input vector with well log inputs is converted by means of the hidden layer into an output vector with facies. The forward-feeding process weights the input well log to derive a one of the predefined facies. The output is then back-propagated from the output layer to the input layer, where the output can be compared with the actual (from core description) facies present. The error between the output and actual facies is subsequently calculated and the entire process continues until the error can no longer be reduced. The output is a series of probabilities of the presence of each facies which is used to generate a final, discrete facies response (Rogers et al., 1992; Saggaf and Nebrija, 2000; Dubois et al., 2007).

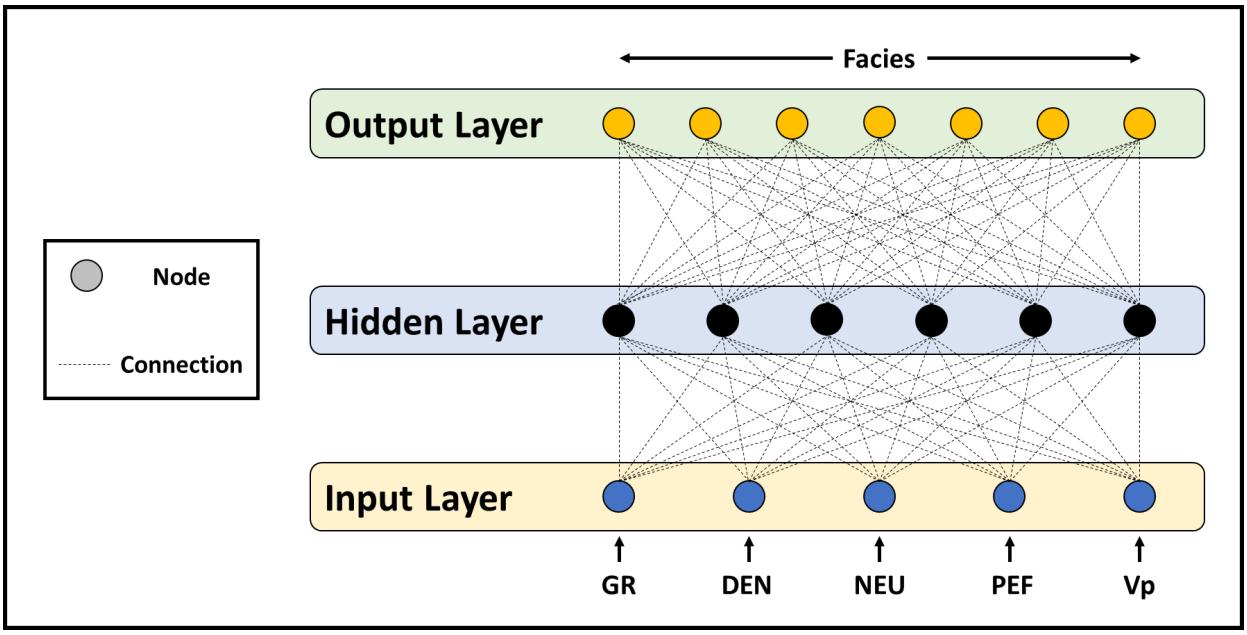

Figure 13: Artificial neural network operation schematic showing paths for the forward-feeding and backward-propagation between the nodes in the input and output layers (modified from Rogers et al., 1992 and Dubois et al., 2007).

4. RESULTS

4.1. Lithofacies

The Brae Formation within the South Brae Field is comprised of seven (7) broad lithofacies that are identified from core samples of Well O. Key lithofacies identified from core descriptions and literature include: (1) shale, (2) silty shale, (3) sandy siltstone, (4) sandstone, (5) calcite-cemented sandstone, (6) pebbly sandstone, and (7) conglomerates. Table 2 summarizes the lithofacies, their descriptions, and depositional environment interpretations. Facies present in the South Brae Field can be split into 10 (Cherry, 1993; Stow et al., 1982; Turner et al., 1987; Turner et al., 2018). However, the classification is simplified to seven because the facies need to be distinguishable by well logs, represent heterogeneity suitably, and remain petrophysically distinct from one another (Dubois et al., 2007).

Lithofacies	Description	Depositional Process Interpretation
Shale	Laminated organic-rich shale.	Hyperpycnal flows and hemipelagic settling.
Silty Shale	Shales (50 to 80 percent) interlaminated with fine- and very fine-grained sandstones and silts.	Muddy turbidity currents and hemipelagic settling.
Sandy Siltstone	Siltstones and sandstones (50 to 80 percent) interlaminated with shales.	Low density turbidite flows and hemipelagic settling.
Sandstone	Normally graded medium- to very coarse-grained sandstones. Medium- to thick-bedded. Thin parallel and wispy silt laminations separate.	Medium and high density turbidite flows.
Calcite-cemented Sandstone	Massive thick-bedded sandstone with an abundance of calcite cement.	Submarine fan channel and diagenetic precipitation from pore fluids and shell dissolution.
Pebbly Sandstone	Medium- to very-coarse grained sandstones with abundant floating pebble-sized quartz clasts.	Medium and high energy sandy debris flows.
Conglomerate	Large, floating quartz clasts within a medium to coarse grained sandstone matrix.	Medium and high energy debris flows.

Table 2: Summary of major lithofacies groups present in the Brae Formation.

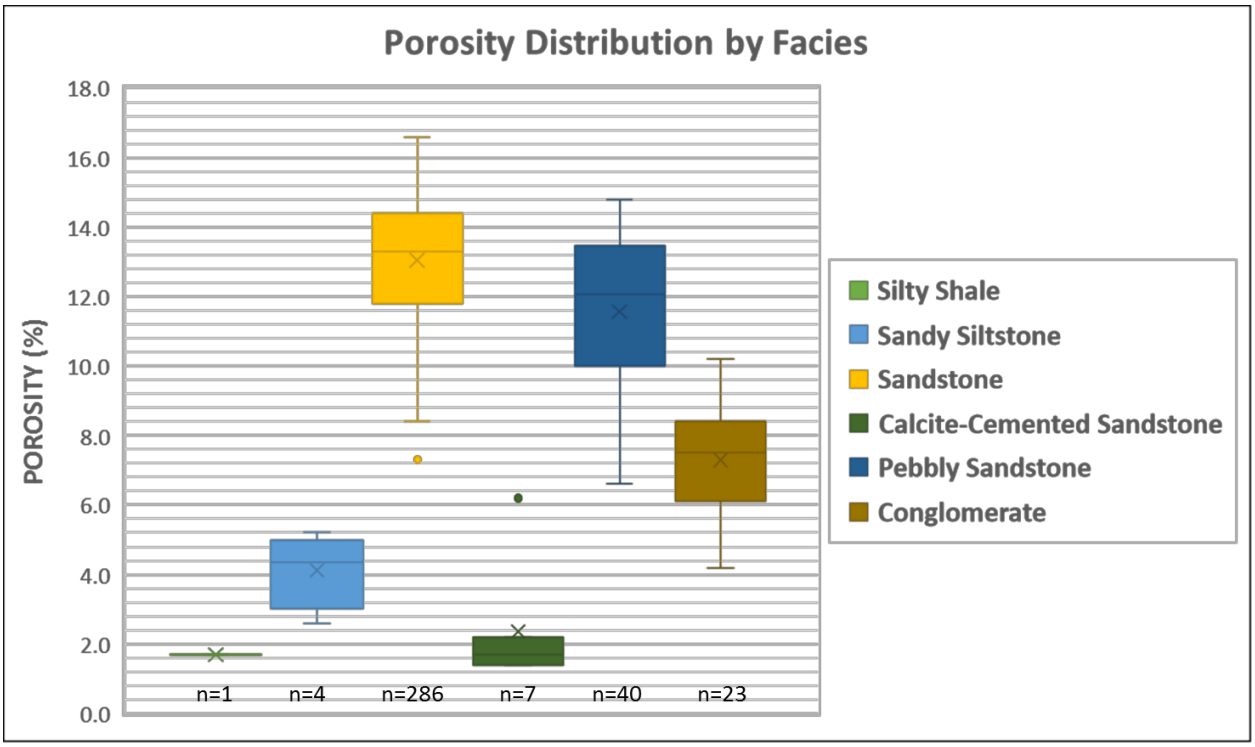

Figure 14: Distribution of core-measured porosities grouped by lithofacies.

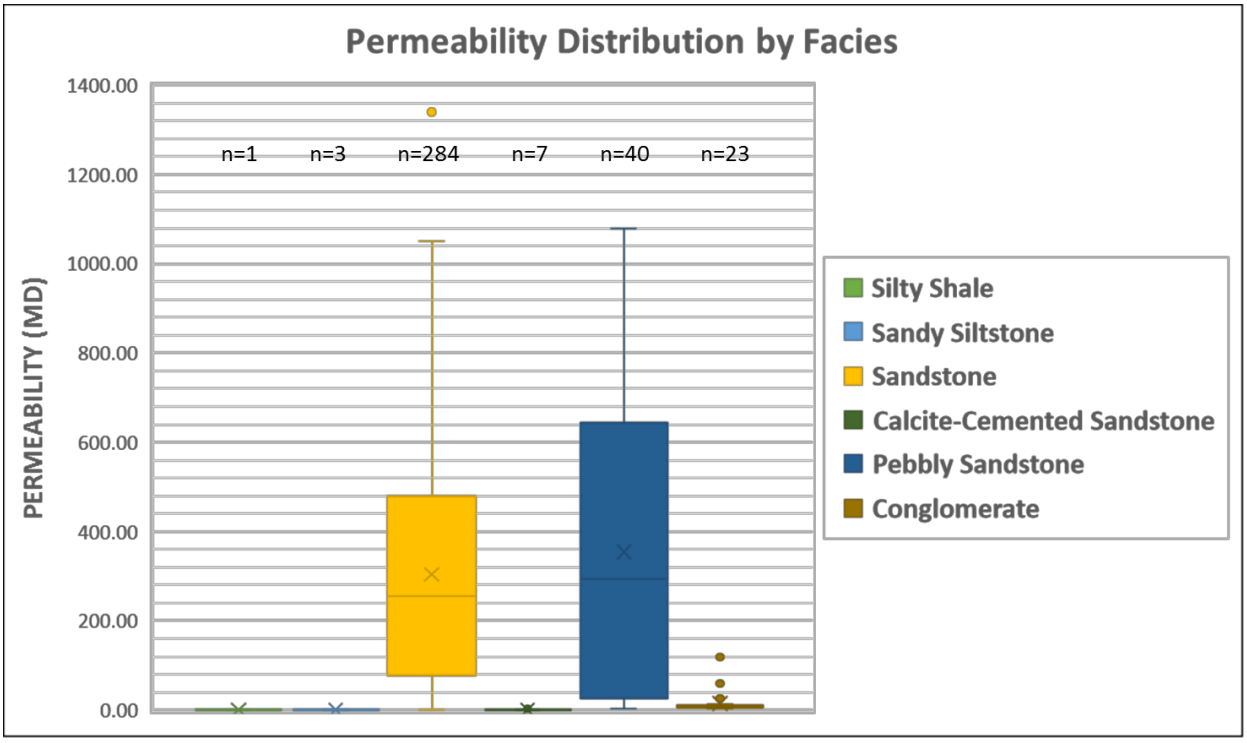

Figure 15: Distribution of core-measured horizontal permeabilities (Kh) grouped by lithofacies.

4.1.1. Shale

The shale present in, and above, the Brae Formation is the Kimmeridge Clay. It is an organic-rich shale deposited as a result of hyperpycnal flows and hemipelagic settling. The shales interbedded with the Brae Formation sandstones and conglomerates form the middle and lower members of the Kimmeridge Clay Formation (Partington, 1993; Fraser et al., 2003). The upper member, which forms the overlying seal of the reservoir, is not cored in Well O. However, the middle members appear interlayered with siltstones at the base of the core. XRD analysis shows the composition of the clays to be primarily illite (up to 97 percent), and almost equal proportions of chlorite and kaolinite. The Kimmeridge Clay has been described in the literature as a thinly laminated dark grey shale (Stow et al., 1982; Turner et al., 2018).

4.1.2. Silty Shale

The silty shale facies is composed of 80 to 50 percent shale, with the residual grain composition being comprised of fine grained sandstones and silts. It is composed of shale interlayered with very thin (up to 1 centimeter), rippled, sandstones and silts. XRD analysis shows almost similar abundances of quartz and clays, 41 and 31 percent respectively. Feldspars (18 percent) and muscovite (5 percent) are also present. Thin section analysis shows layering – organic clay layers and quartz-rich silt and sand beds in a clayey matrix (Fig. 16). Core plug porosity and permeability measurements hint at a very tightly packed interval – with less than 2 percent and less than 0.1 millidarcies recorded (Figs. 14 & 15). This interval is deposited due to muddy turbidity currents and hemipelagic settling (McClure and Brown, 1992).

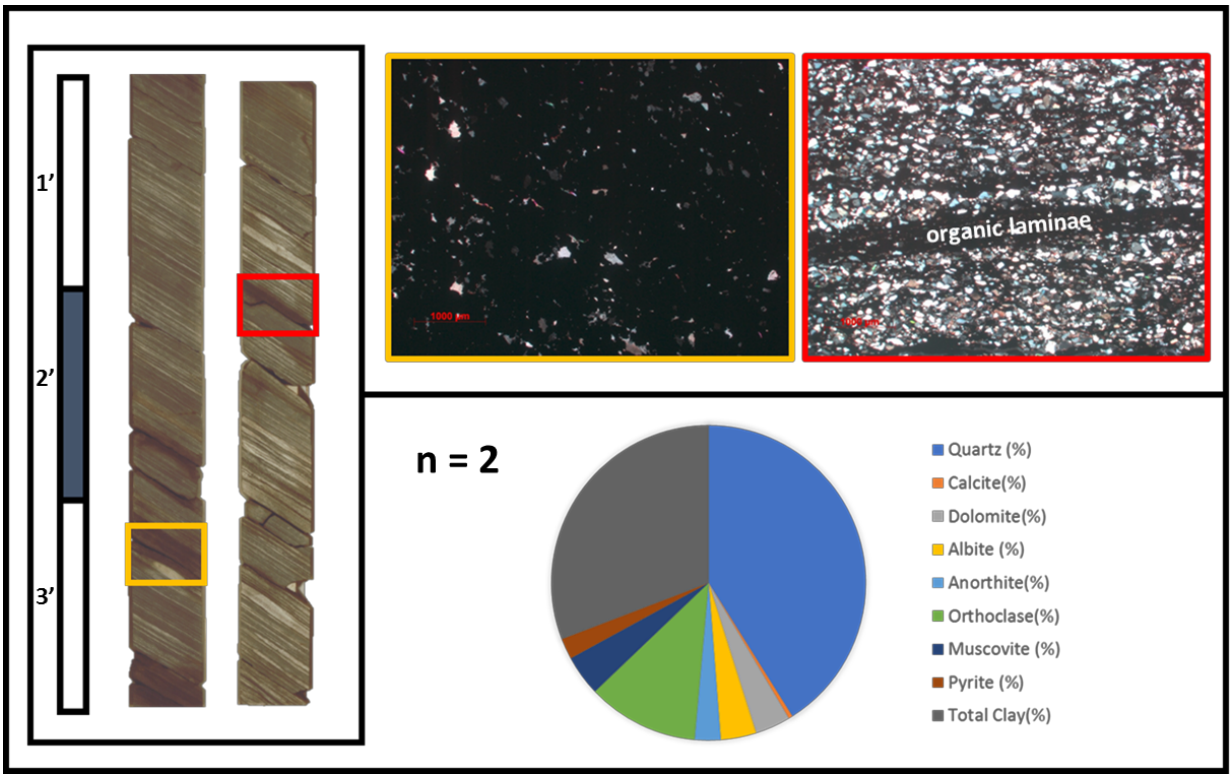

Figure 16: Core (left), thin section photomicrographs (top right), and relative XRD bulk mineralogy of silty shale. Yellow and red outlines on core indicate location of thin-sections.

4.1.3. Sandy Siltstone

The sandy siltstone facies is composed of 80 to 50 percent sandstone and silt, the remainder being shale. It is composed of thin-bedded (up to 3 centimeters), ripple cross-laminated, fine- to medium-grained sandstones with thin laminations of shales separating them. Thin section analysis shows silts and clays in the spaces between fine sand grains and clay laminations parallel to bedding. XRD analysis of the thin section sample depths show an abundance of quartz (50 percent), clays (30 percent), and dolomites (7 percent). The dolomites are observed in hand sample to be present within the clay laminations (Fig. 17). Porosities measured from core plugs are between 2.5 and 5.5 percent. Permeabilities are under 1 millidarcy

(Figs. 14 & 15). This facies is interpreted as being deposited due to low density turbidity currents and hemipelagic settling (Stow et al., 1982; McClure and Brown, 1992).

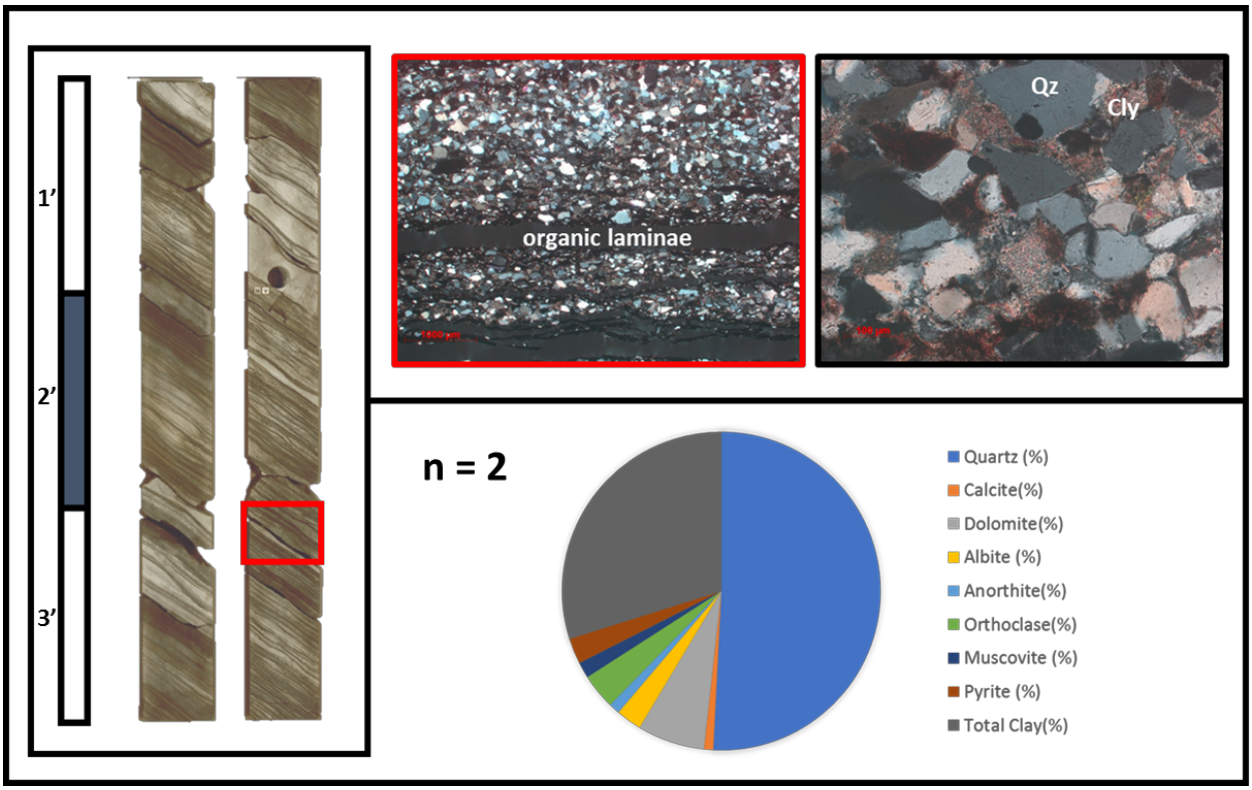

Figure 17: Core (left), thin section photomicrographs (top right), and relative XRD bulk mineralogy of sandy siltstone. Red outline on core indicates location of thin-section.

4.1.4. Sandstone

The sandstone is comprised of normally graded medium- to very coarse-grained sandstones with poor to moderate sorting. Bed bases are generally concentrated with rounded to sub-rounded quartz granules. The proportion of silt-sized grains is less than 10 percent. XRD analyses indicate about 3 (volume) percent each of albite, anorthite, and orthoclase grains – corroborating the granitic origin of the sediments. The grains are primarily quartz cemented. Dolomite cement is observed in core as flakes within thin silt laminations separating the beds

(McLaughlin, 1992). Petrographic analysis of thin sections shows a lot of grain-to-grain contacts with quartz overgrowths and cements. In some cases, clumps of clay are trapped between grains, potentially occluding fluid flow (Fig. 18).

Individual beds are mostly massive and structureless. However, some beds exhibit faint parallel laminations and occasional silt- and clay-rich rip-up clasts – indicating high energy deposition. The beds are thin- to thick-bedded (up to 5 feet). Individual beds are amalgamated or separated by very thin silt laminae. Bed deformation is observable in some thin and medium sized beds – indicating sediment loading. Moderate to very good petrophysical properties are observed in this lithofacies from core plug measurements. Porosity values range from 8 to 17 percent, with an average of 13 percent. Permeability values range from 10 to 1300 millidarcies, with an average of 300 millidarcies (Figs. 14 & 15).

This lithofacies is representative of deposition by submarine fan channels. It corroborates the late-stage depositional model (Fig. 7) of the Brae Formation in the J66 sequence, as grain roundness and moderate sorting indicate large distance from its provenance or a lot of weathering at the source – which occurs with the passage of time (Fletcher, 2003; Turner et al., 2018).

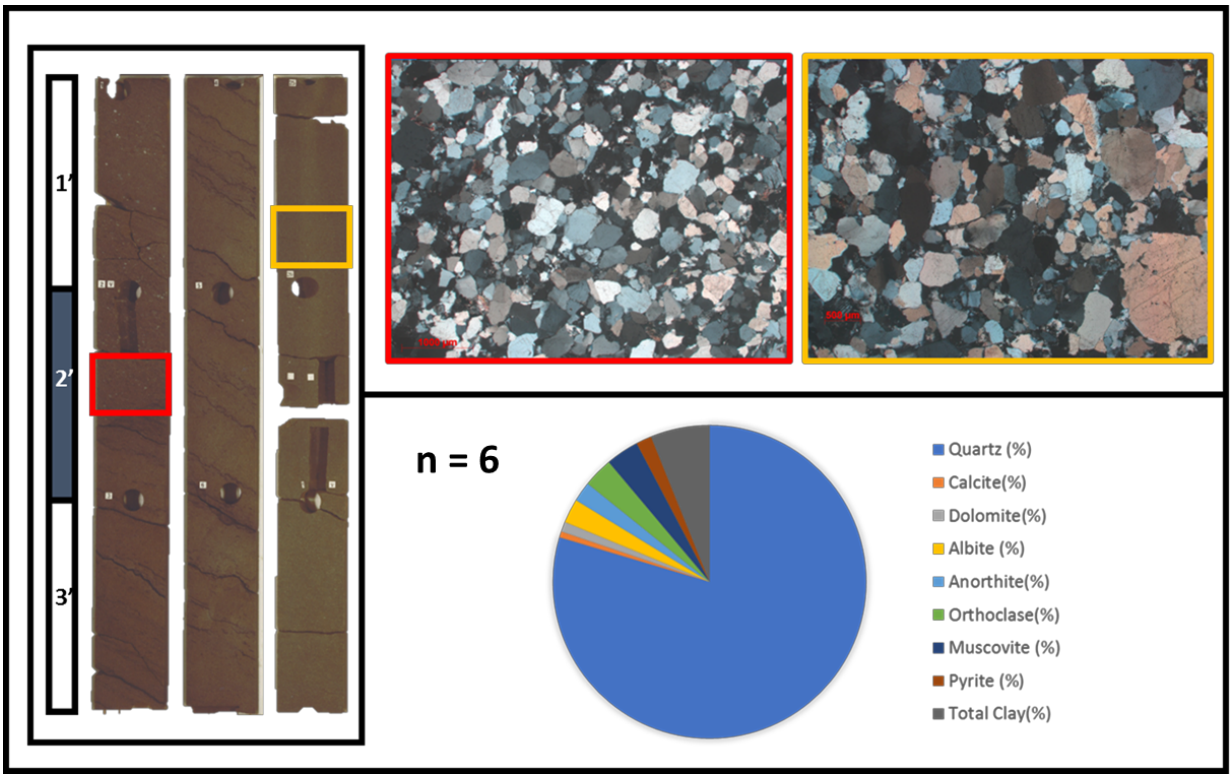

Figure 18: Core (left), thin section photomicrographs (top right), and relative XRD bulk mineralogy of sandstone. Red and yellow outlines on core indicate location of thin-sections.

4.1.5. Calcite-Cemented Sandstone

The calcite-cemented sandstone is similar to the sandstone described in the previous sub-section. It is a massive thick-bedded, structureless sandstone with a visible abundance of calcite cement, giving it a light grey to white appearance. In Well O, only two intervals show this extensive calcite cementation. XRD analysis shows a reduced amount of total clays (2 percent) present in this interval when compared to the underlying and overlying sandstones (Fig. 19). This overall composition of this interval is like the sandstones in composition, but for the abundance of calcite.

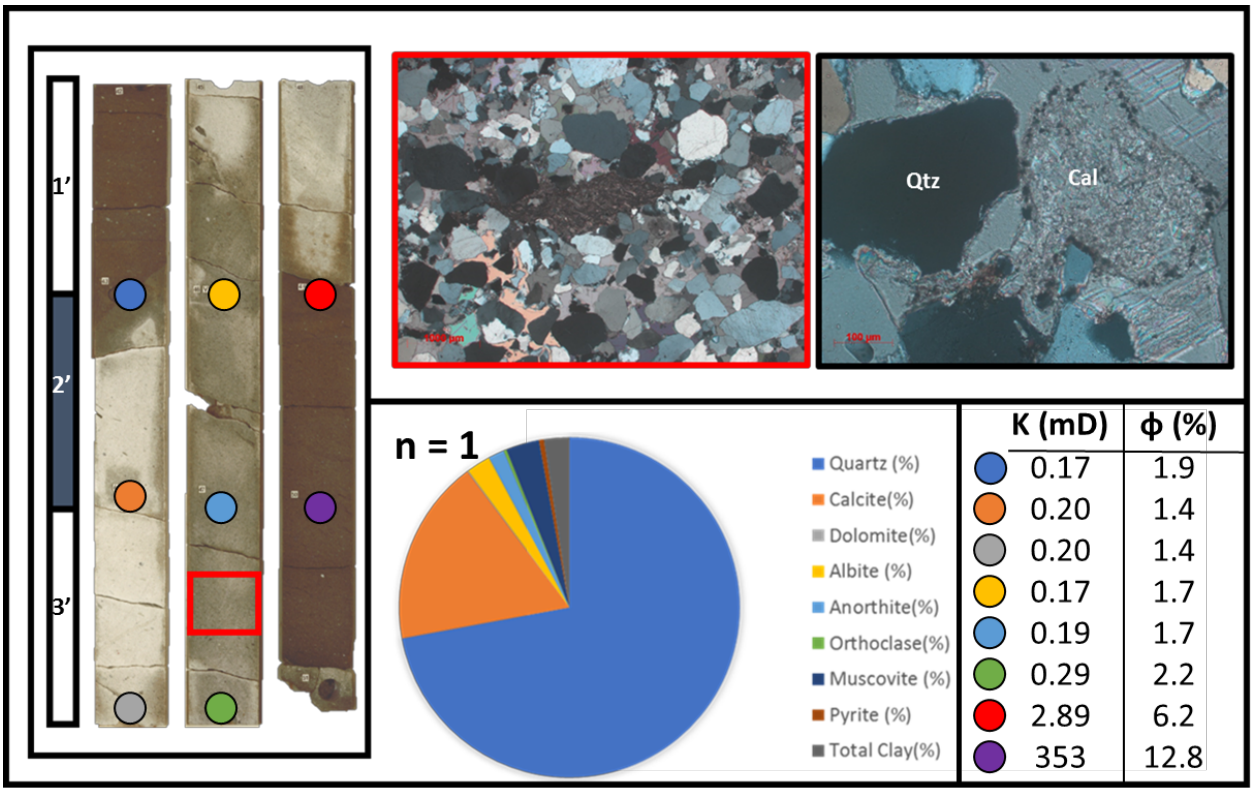

Figure 19: Core (left), thin section photomicrographs (top right), and relative XRD bulk mineralogy of calcite-cemented sandstone. Red outline on core indicates location of thin-section. Color-filled circles indicate core-plugs and their corresponding measurements.

In core, it appears as having a sharp base – the original sandstone bed base – and it gradually fades away at the top of the 6-foot interval. This appearance suggests the cement spreading from the base upwards. However, core plug porosity and permeability measurements indicate the calcite cementation starting from the center of the interval and spreading vertically in both directions. The porosity at the center of the interval is 1.4 percent. It increases to 1.9 percent towards the top and to 2.2 then 6.2 percent from the center downwards (Fig. 14). The permeability at the center is 0.17 millidarcies. It increases to 0.2 millidarcies towards the top and increases to 2.89 millidarcies towards the base. The porosities and permeabilities measured in the uncemented sandstones immediately above and below the concretion are 13.8 and 12.8 percent and 494 and 353 millidarcies, respectively (Fig. 15). XRD analyses of a sample in the center of

the concretion shows an 18 percent volume of calcite present. The massive reduction in porosity compared to the similarly structureless sandstones present above and below the sampled points indicates the calcite cement filled the original pore volume. Thin section analysis shows reduced grain-to-grain contacts in this facies. Instead, calcite cementation takes the place of the inter-grain content and porosity. This indicates this facies is probably a hindrance to the free flow of reservoir fluids within the J66 sequence. This facies is interpreted to be resulting from diagenetic alteration caused by the abundance of meteoric water, dissolving shell fragments, and the shallow burial allowing for interaction with the pore fluids originally present (McLaughlin, 1992).

4.1.6. Pebbly Sandstone

The pebbly sandstone is composed of poorly-sorted, medium- to very coarse-grained sandstones with an abundance of quartz pebbles (0.3 to 1.2 cm). The pebble roundness ranges from angular to rounded. The clast concentrations within the medium- to very coarse-grained sandstone matrices vary from 10 to 30 percent. XRD analysis shows that the composition of this facies is primarily quartz (greater than 90 percent), with small fractions of feldspars (less than 4 percent) and even less clays (less than 2 percent). However, thin section analysis of the depths sampled for XRD highlights something unique about the low clay volume observed from XRD – the clays appear in tiny clumps that are trapped in between tightly packed quartz grains (Fig. 20). These shale clumps (floccules??) likely occlude porosity where they are present within the matrix. The porosity of the pebbly sandstones ranges from 6.5 to 15 percent – the average is 11.5 percent. The permeability range observed is 1 to 1100 millidarcies (Figs. 14 & 15). The beds are medium- to thick-bedded (1 to 3 feet), though, bed boundaries are harder to distinguish in this

facies. This facies is interpreted as being deposited by high and medium energy sandy debris flows (Shanmugam, 2016).

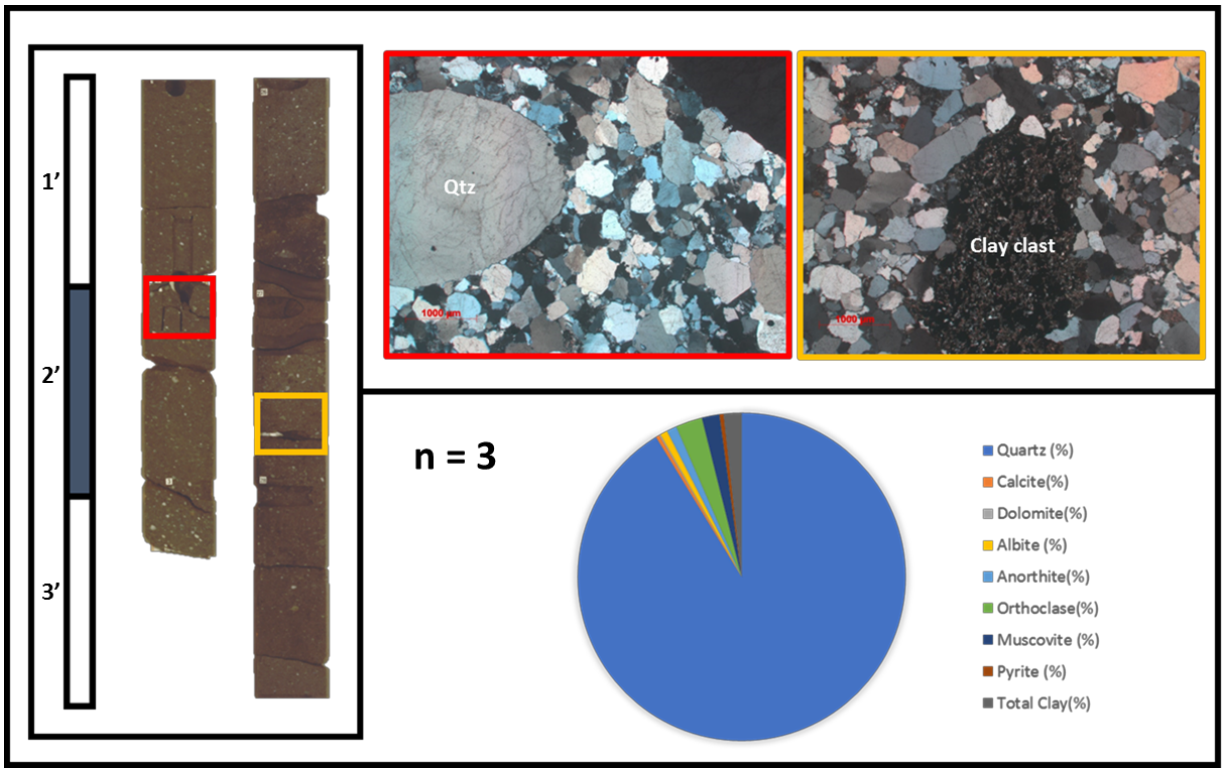

Figure 20: Core (left), thin section photomicrographs (top right), and relative XRD bulk mineralogy of pebbly sandstone. Red and yellow outlines on core indicate location of thin-sections.

4.1.7. Conglomerate

The conglomeratic facies observed in core has a matrix of pebbly sandstones. The sands in the matrix are medium to coarse grained, and the relatively tight-packed quartz pebbles are 1 to 2.5 centimeters – with concentrations as high as 70 percent. Large, subrounded to angular, floating quartz clasts (up to 15 centimeters) are supported by the very poorly-sorted matrix. XRD analysis shows a moderate presence of clays (9 percent), orthoclase (3 percent), and muscovite (4 percent) in a primarily quartz-rich (82 percent) composition. Thin section analysis shows a

tightly packed matrix, of primarily quartz grains and occasional shale clasts as well (Fig. 21). This facies has measured porosities of 4 to 10 percent – with an average porosity of 7 percent. Measured permeability ranges from 1 to 120 millidarcies – with an average of 10 millidarcies (Figs. 14 & 15). This facies is interpreted as being the basal deposit of a high-energy debris flow, as large cobbles are transported up to 2 miles into the basin (where this core was collected).

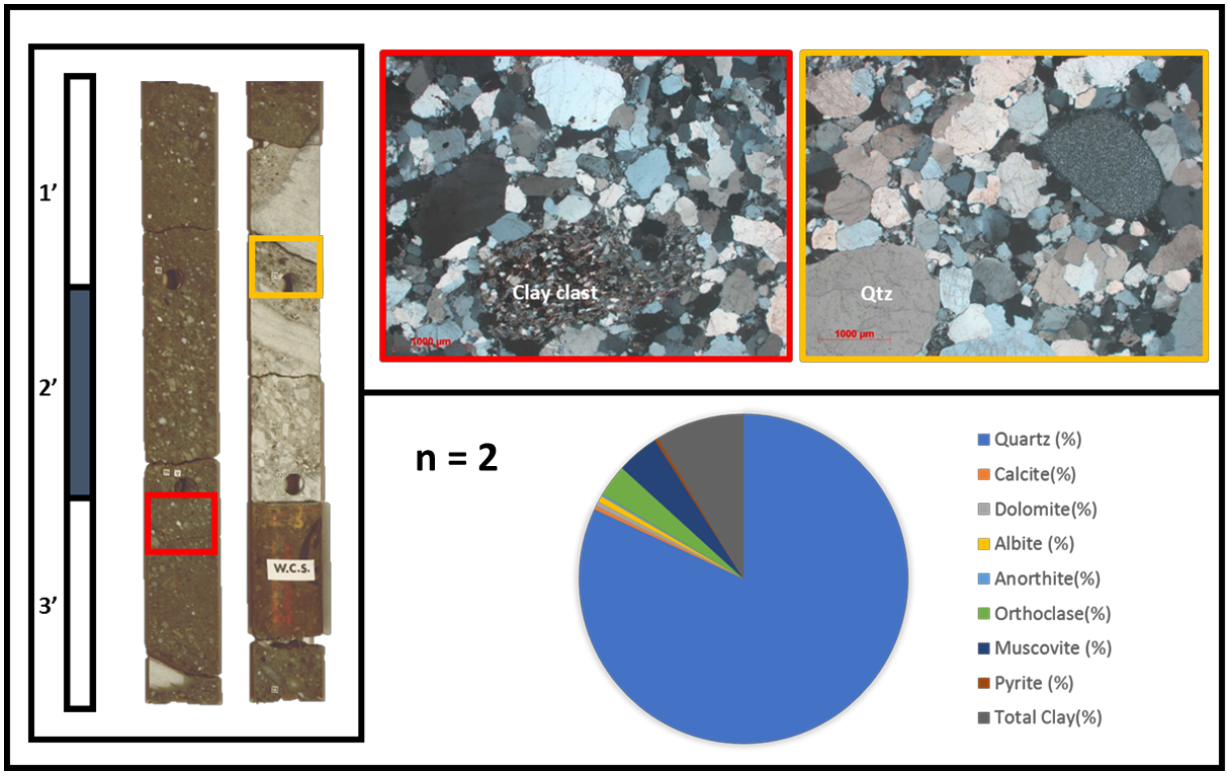

Figure 21: Core (left), thin section photomicrographs (top right), and relative XRD bulk mineralogy of conglomerate. Red and yellow outlines on core indicate location of thin-sections.

4.2. Electrofacies Classification

4.2.1. Wireline Log-Conditioning

The effects of the presence of shale were removed from the porosity calculated from the bulk- and neutron-density logs. This was done by removing a shale volume weighted porosity from the calculation in order to get the total density porosity (PHID.c) of the rock. It relies on the accuracy of the shale volume calculated using the gamma ray log (Eslinger and Pevear, 1988). This was done to test for any possible gains from shale-corrections on the precision and accuracy of the predictions. The resulting PHID.c matched the total porosity measured from core plugs (Fig. 22).

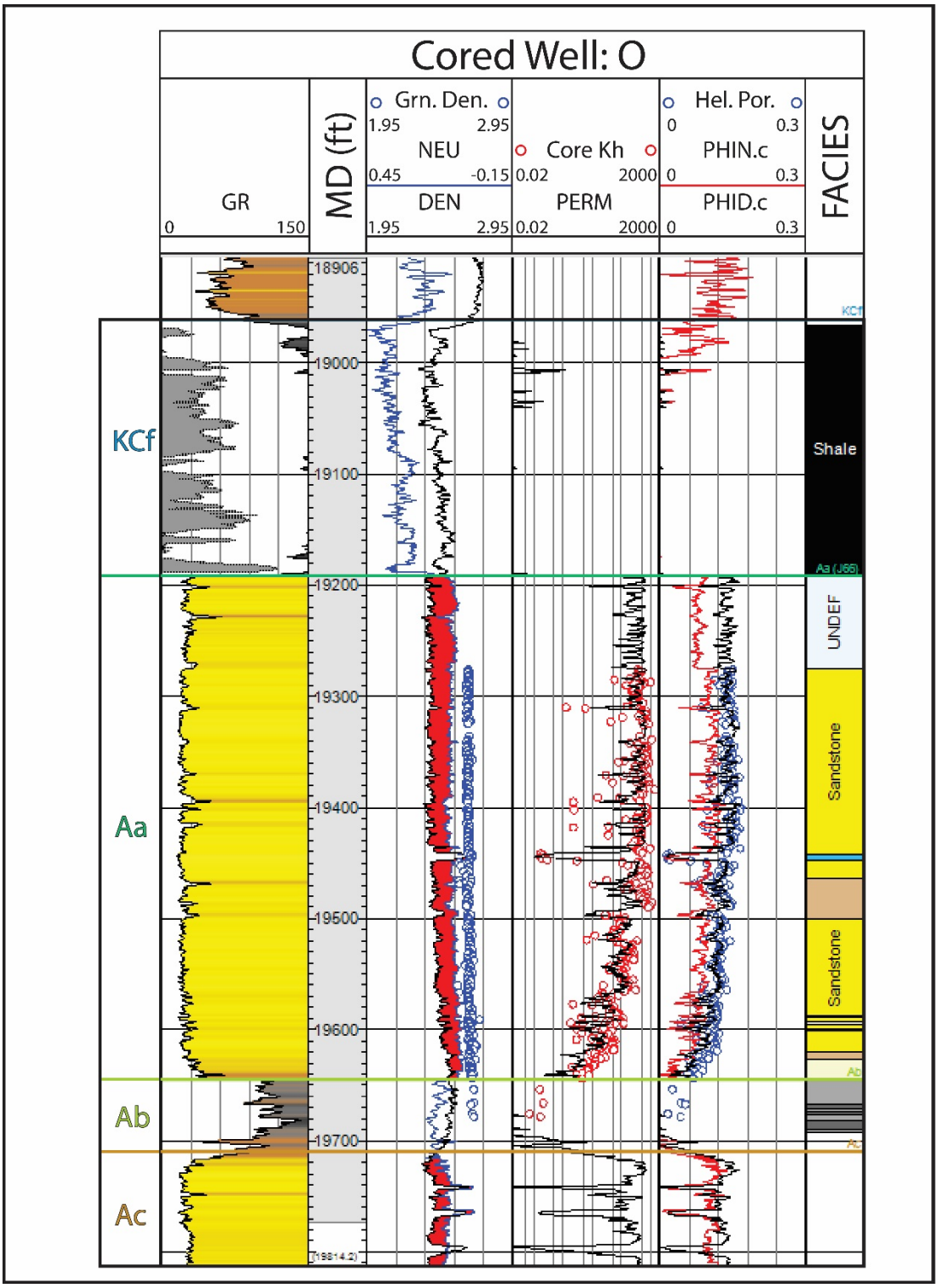

Figure 22: Well O wireline logs, core measurements and lithofacies. Porosity is used to derive permeability and is verified with core permeability measurements. Corrected neutron- and density-porosity are calibrated to core-measured porosity. Lithofacies are from core descriptions.

4.2.2. Classifier Evaluation

Two performance measures were used in the confusion matrix (Table 3 & 4) evaluating the electrofacies classifiers – precision and accuracy. Precision, also referred to as the positive prediction value, measures the ratio of true positives to predicted positives (true positives and false positives). It measures the degree of correctness for each instance that a positive prediction (rock type is present) is made for each electrofacies (Lewis, 1991). Accuracy is a ratio of true predictions (positives and negatives) to all possible predictions (true and false). It measures how often a classifier is correct for all electrofacies it predicts (Fawcett, 2006).

4.2.3. Multi-variate Clustering Analysis (MVCA)

MVCA conducted with GAMLS yielded high accuracies – 91 to 92 percent (Table 6). The precision of the classifiers is highest in the shales (Table 5). This is expected as there are a lot of data samples used for prediction due to the thickness of the Kimmeridge Clay in Well O. Another contributing factor is the uniqueness of the wireline log signature of the shale. It has the highest GR, VShale responses and the lowest porosity. Precision for pebbly sandstones were the lowest (on average) by the MVCA classifier (50 percent). Silty shales and conglomerates also have relatively low precision scores – less than 80 percent (Table 5). These electrofacies are hard to predict as they share compositions similar to one or more facies they are in close vertical proximity to. This leads to muted log responses that are difficult to distinguish from one another.

4.2.4. Artificial Neural Network (ANN)

ANN classification conducted with Petrel yielded high accuracies as well – 89 to 91 percent (Table 6). As in the MVCA, shales are the electrofacies with the highest precision for this classifier. Similarly, the silty shales, pebbly sandstones, and conglomerates have precisions

below 80 percent (Table 5). Though, conglomerates have average precision values almost 10 percent higher than in the MVCA classifier. Splitting the average precision results by input log combinations – original and corrected – yields more positive results. The average precision of the ANN in classifying pebbly sandstones – one of the potential reservoir facies – using only original wireline log combinations is about 93 percent.

Accuracy		Prediction						
91.1%		Shale	Silt-Shale	Sand-Silt	Sandstone	Cal. Cmt. Sst.	Pebbly Sandstone	Conglomerate
Actual	Shale	445	0	2	0	0	0	0
	Silt-Shale	0	21	7	0	0	0	0
	Sand-Silt	0	10	61	0	0	0	0
	Sandstone	1	0	3	731	0	7	20
	Cal. Cmt. Sst.	0	0	0	0	12	0	0
	Pebbly Sandstone	0	0	0	64	0	11	13
	Conglomerate	0	0	0	2	0	0	45
Precision		99.8%	67.7%	83.6%	91.7%	100.0%	61.1%	57.7%

Table 3: Confusion matrix showing actual lithofacies and predicted electrofacies for an MVCA classification made using GR, DEN, NEU, and Vp. Overall accuracy of the classifier is in the top left.

Accuracy		Prediction						
91.2%		Shale	Silt-Shale	Sand-Silt	Sandstone	Cal. Cmt. Sst.	Pebbly Sandstone	Conglomerate
Actual	Shale	447	1	0	0	0	0	0
	Silt-Shale	0	20	8	0	0	0	0
	Sand-Silt	0	7	59	0	0	0	0
	Sandstone	0	0	0	583	1	0	9
	Cal. Cmt. Sst.	0	0	0	0	10	0	0
	Pebbly Sandstone	0	0	0	78	0	9	1
	Conglomerate	0	0	1	6	0	1	39
Precision		100.0%	71.4%	86.8%	87.4%	90.9%	90.0%	79.6%

Table 4: Confusion matrix showing actual lithofacies and predicted electrofacies for an ANN classification made using GR, DEN, NEU, and PEF. Overall accuracy of the classifier is in the top left.

4.2.5. Comparison of Results

Overall, both classifiers yield very high classification accuracies (around 90 percent) and are within a few percentage points of one another (Table 6). No obvious distinction is apparent in the accuracies when comparing log combinations or classification methods. The precisions of each rock type classification vary quite significantly. The highest precision for sandstone is achieved when using an MVCA classifier (Table 5). However, the precision for pebbly sandstones and conglomerates is very low in comparison – 40 and 25 percent less, respectively. This is due to several classification errors. For example, some of the conglomerates and pebbly sandstones are misclassified as sandstones (Table 3). Likewise, a lot of the pebbly sandstones are misclassified as sandstones. This is possible due to their similar compositions of a generally quartz-rich matrix. The ANN classifier has relatively fewer instances of sandstones being misclassified as pebbly sandstones (Table 4) even though, it also misclassifies pebbly sandstones as sandstones. The ANN has relatively higher precisions on average because it is able to back-propagate its results and readjust the weights assigned to the inputs and recalibrating to get a better output (Table 5). The high aggregate accuracies observed in the MVCA classifier indicates that, in general, the classifier can distinguish a very high number of true absences of a rock type in addition to correctly predicting its presence.

Calculated logs do not improve precision when compared to the original wireline logs they are derived from (Table 5). A likely explanation for this is the VShale log used in the calculated log combinations. The GR log it is derived from is measured along an extensive interval with a lot of relative internal heterogeneity, yet it does not highlight it. Normalizing the GR log (to generate the VShale log) highlights aggregate signals acquired over 2-foot intervals. In this relatively homogenous GR regime, it probably does the opposite of that, and introduces

noise relative to the original response (Fig. 22). Another likely problem is the relative process energies of each of the deposits that are potential reservoir facies are not highlighted sequentially on the GR log. The process energies of conglomerates and pebbly sandstones are higher than sandstones. However, sandstones have lower GR responses (Fig. 29). Thus, the VShale log cannot be used for this purpose either.

Wireline logs and their resolutions make electrofacies classification in a formation that exhibits relative homogeneity challenging. Facies that fall in between the standout facies, such as sandstones and shales, are difficult to distinguish, though, this was possible to accomplish in this study. An ideal dataset to use for the electrofacies classification would be XRD. As shown in the previous section, XRD has more unique responses to each of the facies. Thus, combining that into this existing dataset could possibly increase the precision of the classifiers. This would potentially allow for accurate unsupervised classifications, as is currently possible with geochemical proxies in studies focused on shale reservoirs (Turner, 2016; Ekwunife, 2017). However, acquiring an expansive XRD dataset is expensive and impractical (due to the nature of the recording equipment) and the PEF log (when available) offers some improvement in predictions (Table 6).

Classifier		Shale	Silty Shale	Sandy Siltstone	Sandstone	Cal. Cmt. Sandstone	Pebbly Sandstone	Conglomerate
MVCA	O-1	100.0%	71.9%	88.6%	91.3%	100.0%	55.0%	72.1%
	O-2	100.0%	80.0%	91.5%	91.3%	92.3%	47.4%	71.4%
	O-3	99.8%	67.7%	83.6%	91.7%	100.0%	61.1%	57.7%
	O-4	99.1%	80.0%	89.0%	91.9%	100.0%	57.9%	59.2%
	C-1	100.0%	71.9%	88.6%	91.3%	100.0%	55.0%	72.1%
	C-2	100.0%	80.0%	91.5%	91.3%	92.3%	47.4%	71.4%
	C-3	100.0%	66.7%	91.0%	91.4%	92.3%	33.3%	64.7%
	C-4	99.6%	66.7%	91.0%	91.6%	100.0%	43.8%	61.6%
ANN	O-1	99.6%	74.1%	86.4%	87.5%	90.9%	88.9%	75.9%
	O-2	99.3%	80.0%	86.6%	87.9%	90.9%	81.8%	74.5%
	O-3	100.0%	68.0%	82.2%	86.4%	100.0%	100.0%	77.6%
	O-4	99.3%	N/A	67.7%	85.9%	100.0%	100.0%	75.0%
	C-1	99.8%	69.0%	86.6%	86.2%	90.0%	0.0%	72.0%
	C-2	100.0%	66.7%	86.4%	87.0%	90.0%	71.4%	75.0%
	C-3	99.8%	0.0%	68.1%	86.9%	90.0%	100.0%	75.0%
	C-4	100.0%	71.4%	86.8%	87.4%	90.9%	90.0%	79.6%

Table 5: Precisions of electrofacies classifications using MVCA and ANN.

Log Combination		MCVA	ANN
GR, DEN, NEU	O-1	92.2%	90.9%
GR, DEN, NEU, PEF	O-2	92.3%	91.1%
GR, DEN, NEU, Vp	O-3	91.1%	90.3%
GR, DEN, NEU, PEF, Vp	O-4	91.7%	89.0%
VShale, PHID.c, PHIN.c	C-1	92.2%	90.0%
VShale, PHID.c, PHIN.c, PEF	C-2	92.3%	90.5%
VShale, PHID.c, PHIN.c, AI	C-3	91.3%	89.5%
VShale, PHID.c, PHIN.c, PEF, AI	C-4	91.5%	91.2%

Table 6: Accuracy of classifiers using different log combinations.

4.3. Stratigraphic Framework

4.3.1. Stratigraphic Zonation

The Brae Formation in the South Brae Field is correlated across the J66 sequence. Correlations are possible within the J64 sequence (B channel system), though, the data available for that purpose is sparse. The J66 and J64 top surfaces are correlated on wireline logs and seismic (Fig. 29). The intervening shale units represent flooding surfaces within the second-order stratigraphic cycle, as they are deposited over 2 to 4 million years (Fig. 24). These (J66 and J64) tectonostratigraphic units record incidences of basin-filling during a period of regional transgression. The Brae Formation is a second-order stratigraphic cycle deposited in periods of local lowstand during rifting over 14 million years (Fig. 23) (Sneider et al., 1995; Turner et al., 2018).

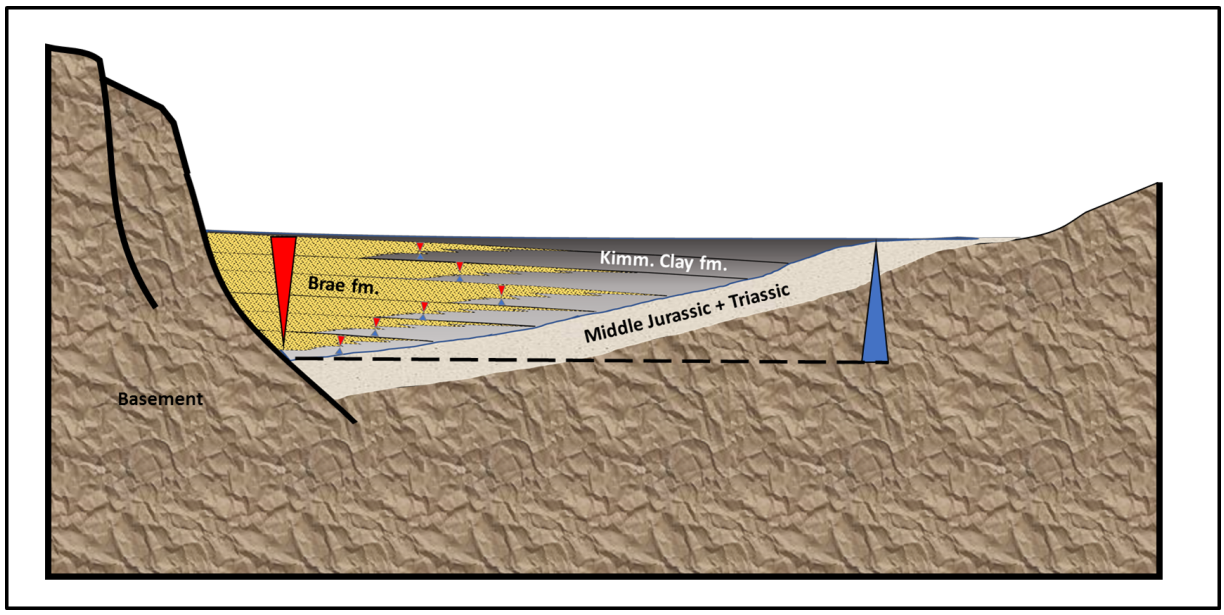

Figure 23: Schematic diagram illustrating concurrent 2nd-order transgressive and regressive cycles, as well as 3rd order sequence stratigraphic cycles. The apparent regression that Brae formation represents is caused by rifting. Not drawn to scale.

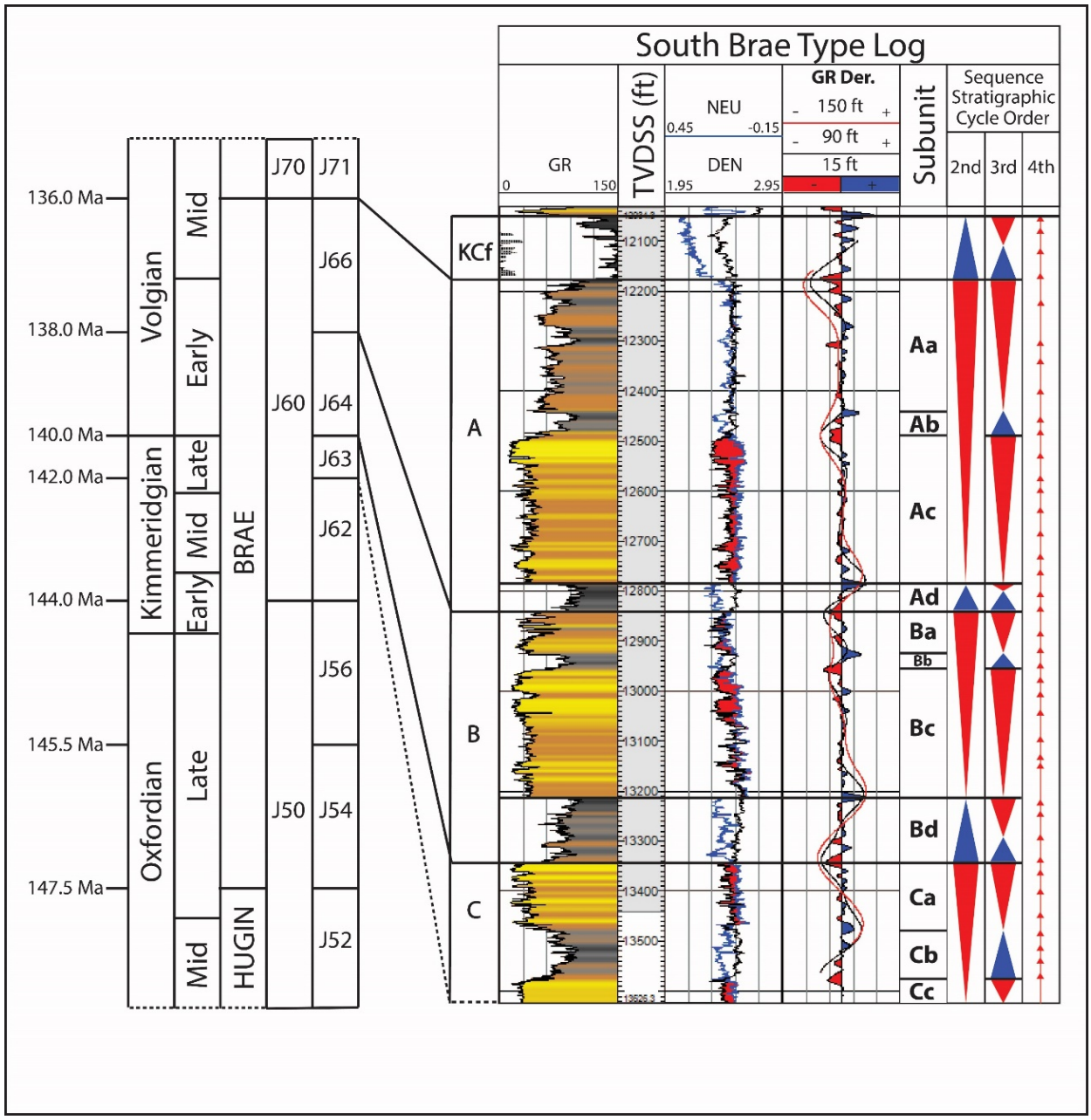

Figure 24: Sequence stratigraphic divisions of the Brae formation defined using GR derivative trend analysis over 15- (4th order), 90- (3rd order), and 150-foot (2nd order) vertical investigation windows. The Brae formation is a singular 2nd order cycle as illustrated in Figure 23.

4.3.2. Wireline Log Correlation

Wireline logs were used to correlate the A (J66) channel system across the field (Fig. 29). This study focused on the A channel system as all the wells available penetrated the interval. The A channel system is readily identifiable on wireline logs as the formation underlying the Kimmeridge Clay. Four key features are generally present – 2 blocky low GR and 2 high GR intervals (Fig. 24). The blocky, low GR intervals represent periods of high, basin-filling clastic input. The character of the wireline logs, along with its expression in core represent high- to medium-density debris flows and turbidity currents from the granitic paleo-highs in the west. The flooding surfaces show relatively high GR responses, representing middle members of the Kimmeridge Clay. The flooding surfaces represent periods of relative quiescence during syn-rift deposition (Fletcher, 2003).

The channels separated by the middle Kimmeridge Clay members are referred to as the Aa and Ac channels. The middle Kimmeridge Clay members separating them are referred to as the Ab, and Ad units. Clastic continental input occurs in subdued amounts and does not cease during the periods of relative depositional quiescence. When well penetrations occur at the margins of the depositional fairways, distinguishing the boundaries of the channels and the middle Kimmeridge Clay members (subunits Ab, Ad, Bb, Bd, Cb, and so on). Smoothened gamma ray derivative curves are used to distinguish the subunits from one another. This was done by smoothing the GR logs at the average interval thickness of the sequence stratigraphic cycles present in the well to be correlated (Fig. 24).

4.3.3. Seismic Stratigraphic Interpretation

A wedge model was constructed to understand tuning behavior of the Brae Formation prior to the commencement of interpretation. The tuning thickness of the J66 to J64 sequence is 145 feet. The thickness and relative homogeneity of the Aa and Ac systems on well logs explain the difficulty in distinguishing individual channels on seismic (Fig. 29). This is true even where the channels exceed the tuning thickness and should be distinguishable in the seismic volume, as constructive interference of the wavelet occurs at 550 feet.

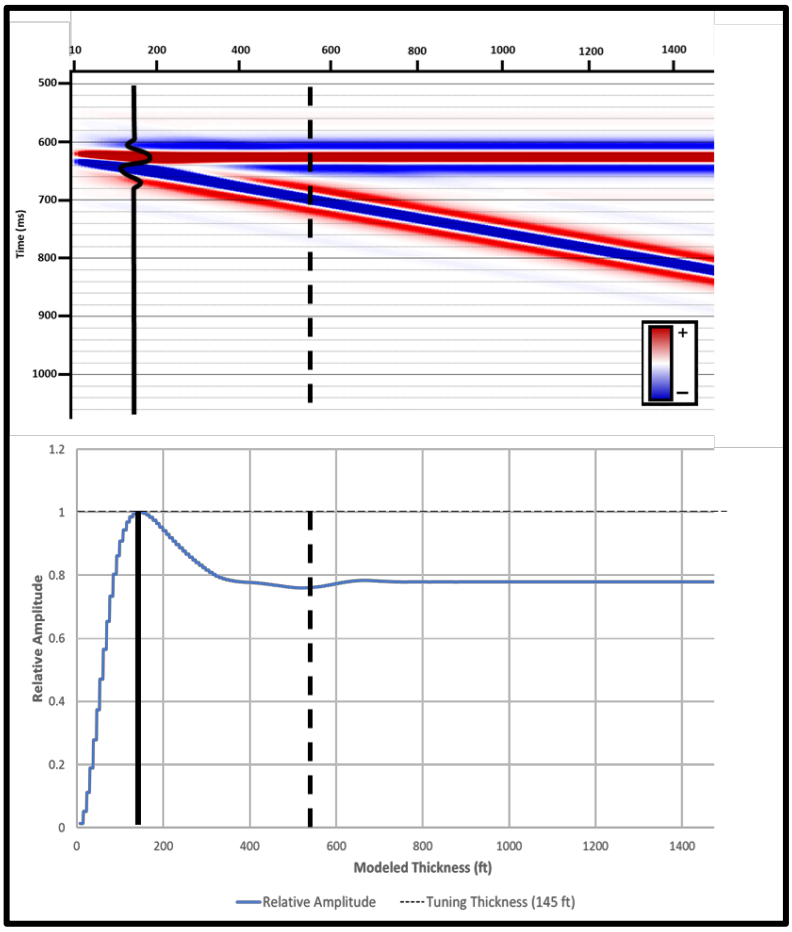

Figure 25: The upper image shows a zero-offset synthetic seismogram wedge model. The lower image shows the relative amplitude of the synthetic extracted at the interface of the top reflector. Constructive interference starts at 550 feet and maximum tuning occurs at 145 feet.

Well ties were used to convert depth correlated well tops to two-way time tops on seismic. The Kimmeridge Clay is represented as a seismic reflector peak. This is because it is a regionally correlative condensed section with a lower acoustic impedance than the overlying Cretaceous sediments. The top of the J66 and J64 sequences are seismic troughs due to the higher acoustic impedance contrast with the overlying sediments – Kimmeridge Clay and J66 sequence. The basement granite is only penetrated by one well which does not provide too much clarity for seismic interpretation. The expression of the basement on seismic amplitude is relatively transparent compared to the overlying and laterally adjacent reflectors (Fig. 26).

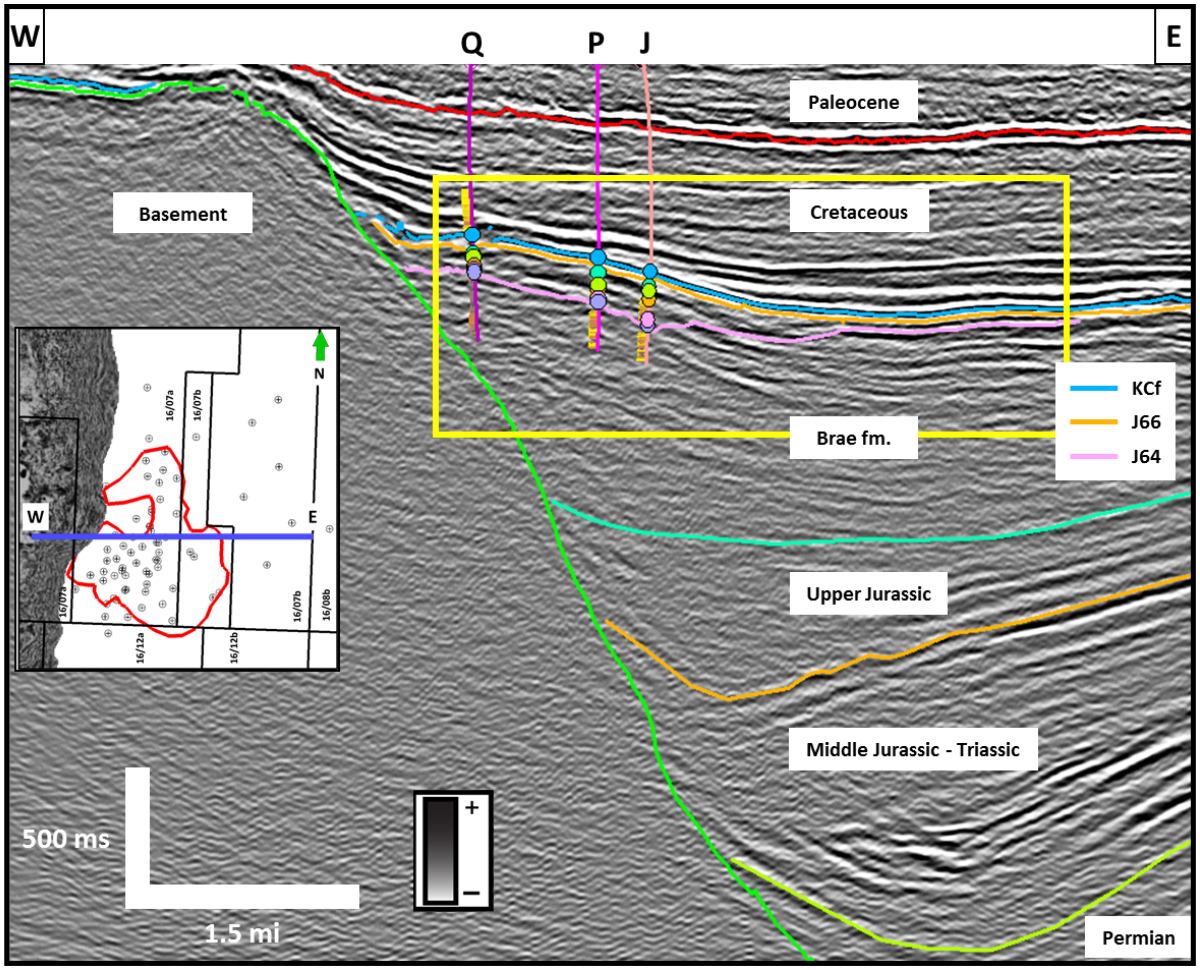

Figure 26: Seismic cross-section showing the basement, graben margin fault, and Permian to Paleocene intervals. Inset map shows cross-section location in field. Yellow box is location of Figure 31.

North-south and east-west trending discontinuities (faults) are observed in the J66 sequence. However, the faults present in the field do not exhibit significant vertical displacement to affect the stratigraphic interpretation of the units of interest within the field. These faults are reverse faults corroborated by the structural expression of the dome crest where the faults are observed (Fletcher, 2003). The effects of these faults on compartmentalization or connectivity cannot be quantified in this study. These faults are not observed in the overlying seal – the Kimmeridge Clay Formation. Thus, indicating any potential connectivity is limited to the J66 sequence and underlying sequences.

4.3.4. Spectral Balancing

The spectral balancing was conducted to broaden the frequency content of the seismic volume and improve the vertical resolution (Marfurt and Matos, 2014). The filter applied to the input signal was: 10 Hz (low cut), 20 Hz (lowpass), 40 Hz (highpass), and 65 Hz (highcut). The filter applied to the resulting frequency content was: 5 Hz (lowcut), 10 Hz (lowpass), 40 Hz (highpass), and 90 Hz (highcut). The resulting frequency spectrum is as shown in Figure 27. A wedge model was made for the reservoir intervals within the spectrally balanced volume. The wedge model showed constructive interference occurring at 355 feet and tuning occurring at 108 feet. Figure 30 shows the improvement in the vertical resolution produced by spectral balancing.

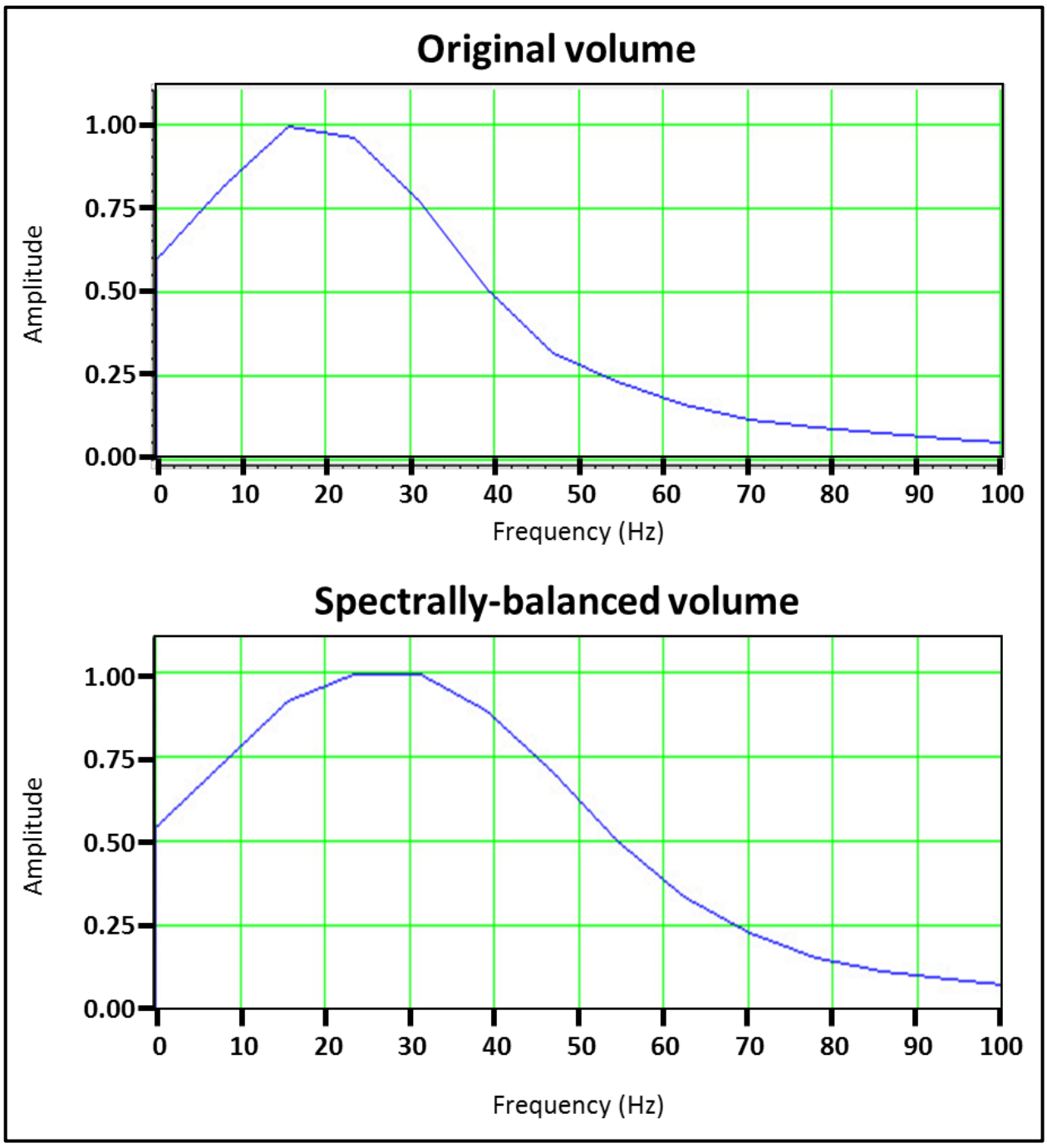

Figure 27: Charts showing the frequency spectrum of the original and spectrally-balanced seismic volumes.

4.3.5. Seismic Attribute Analysis

Spectral decomposition of the J66 sequence shows a large fan-like fairway. In the proximal areas, three (3) east-west linear features in of higher frequency are present that highlight the thinnest parts of the fairway. These areas also correspond to areas of silty shale and sandy siltstone abundance (Figs. 30 & 31). The spectral decomposition, however, does not highlight any of the internal heterogeneities present. The main reason for this is the relatively low and narrow peak frequency spectrum in the channel areas (18 to 24 Hz). This low bandwidth is due to the relative homogeneity (very quartz-rich – similar density) of the Brae Formation, amalgamation (increases apparent thickness) (Fig. 29), and signal attenuation (depths in excess of 12,000 feet below sea level). The resulting image from the J66 cannot be separated to highlight the Aa and Ac channel systems individually. This is because the high apparent thickness resulting from amalgamation causes constructive interference (Fig. 25). Additionally, GR derivative trend analysis over a 150-foot vertical window mimics the constructive interference seen in seismic (Fig. 24).

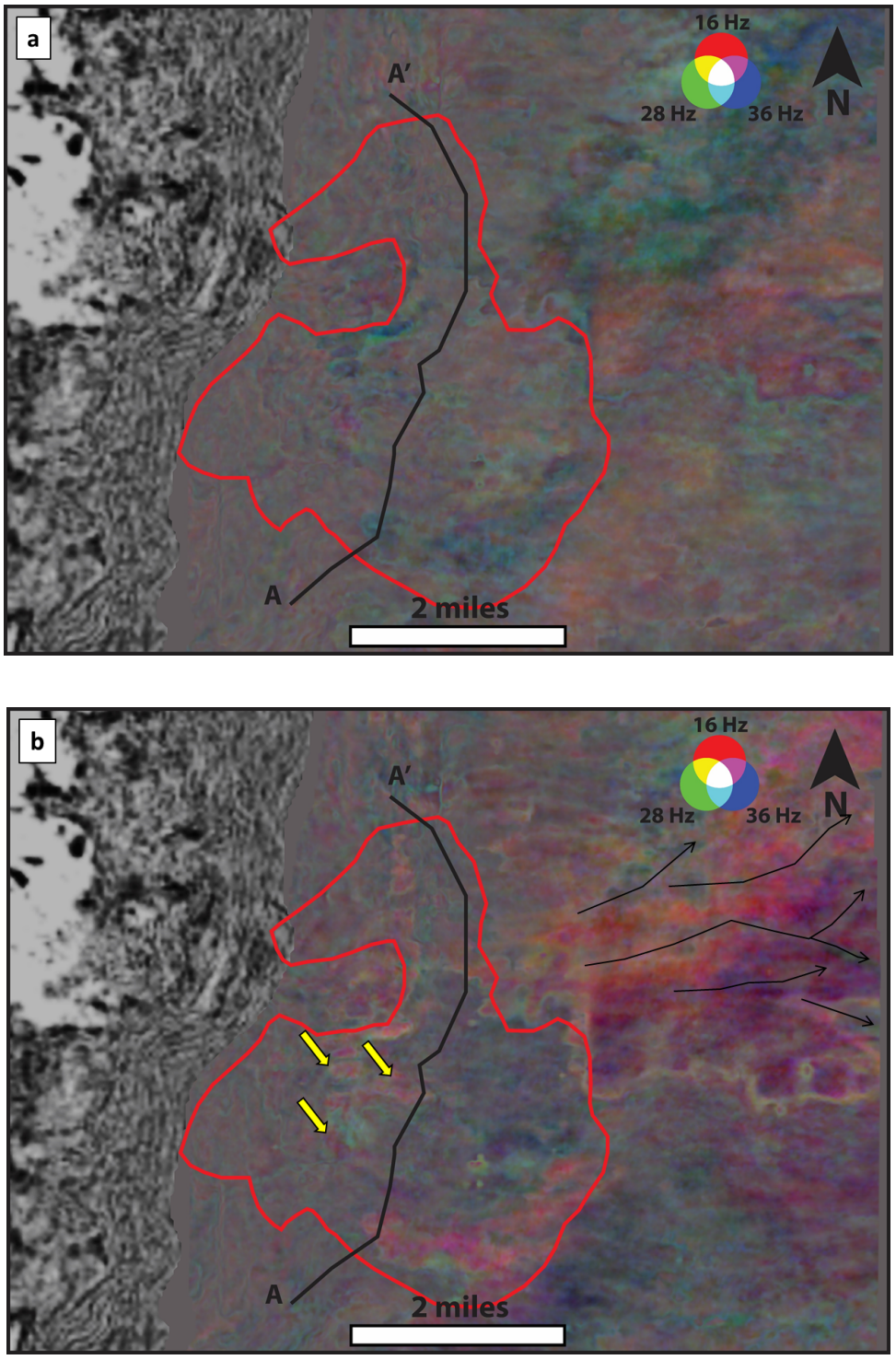

Figure 28: Spectral decomposition of the J66 sequence. (a) stratal slice representing the Ac system taken approximately 75 ms below the top of the J66 sequence. (b) stratal slice representing the Aa system taken 15 ms below the top of the J66 sequence. The yellow arrows point to bifurcated areas. The thin black arrows highlight possible channel paths as highlighted by the 28 Hz frequency voice component.

4.3.6. Stratigraphic Expression of J66 system

4.3.6.1. Unit Ac

The Ac channel system shows a predominance of amalgamated channels on cross-sections and thickness maps (Fig. 29). This is due to the relatively high relief and slope of the sediment source (Fig. 7), which caused predominantly slope-apron fan deposition (Fraser et al., 2003; Turner et al., 2018). This interval has two (2) point-sources. The southern point source splits into two thalwegs that reconnect further into the basin and form a large fan. The northern source is located approximately 1.9 miles to the northeast of the southern point source. The northern thalweg eventually connects to the southern fan approximately 1.2 miles into the basin (Fig. 32). The average thickness within the southern fan is approximately 400 feet. The average thickness of the northern thalweg is 40 feet.

4.3.6.2. Unit Aa

The Aa channel system shows a predominance of individuated channels on cross-sections and stratigraphic thickness maps (Fig. 29). This is due to the reduction in relief and slope of the sediment source, allowing sandier channel-fills to propagate in the major fairways (Fig. 7) (Fraser et al., 2003). There is a junction proximal to the sediment source where the channels split into 3 major thalwegs. Two of the thalwegs flow directly eastward into the Miller field. The other thalweg trends to the northeast and terminates before the Miller Field (Fig. 33). The average thickness of the Aa channel system in the channel thalwegs is 400 feet. The average thickness of the unit is 250 feet.

4.3.6.3. Unit Ab and Ad

Maps of the Ab and Ad units show low thicknesses in the corresponding thalwegs of the channel systems that are deposited above them. This is due to the channels down-cutting into the flooding surface below them (Turner et al., 1987). The GR log character of these units indicates there is continued deposition of low density sandy and muddy turbidites (Fig. 29). The average thickness of the Ab and Ad units is 50 feet.

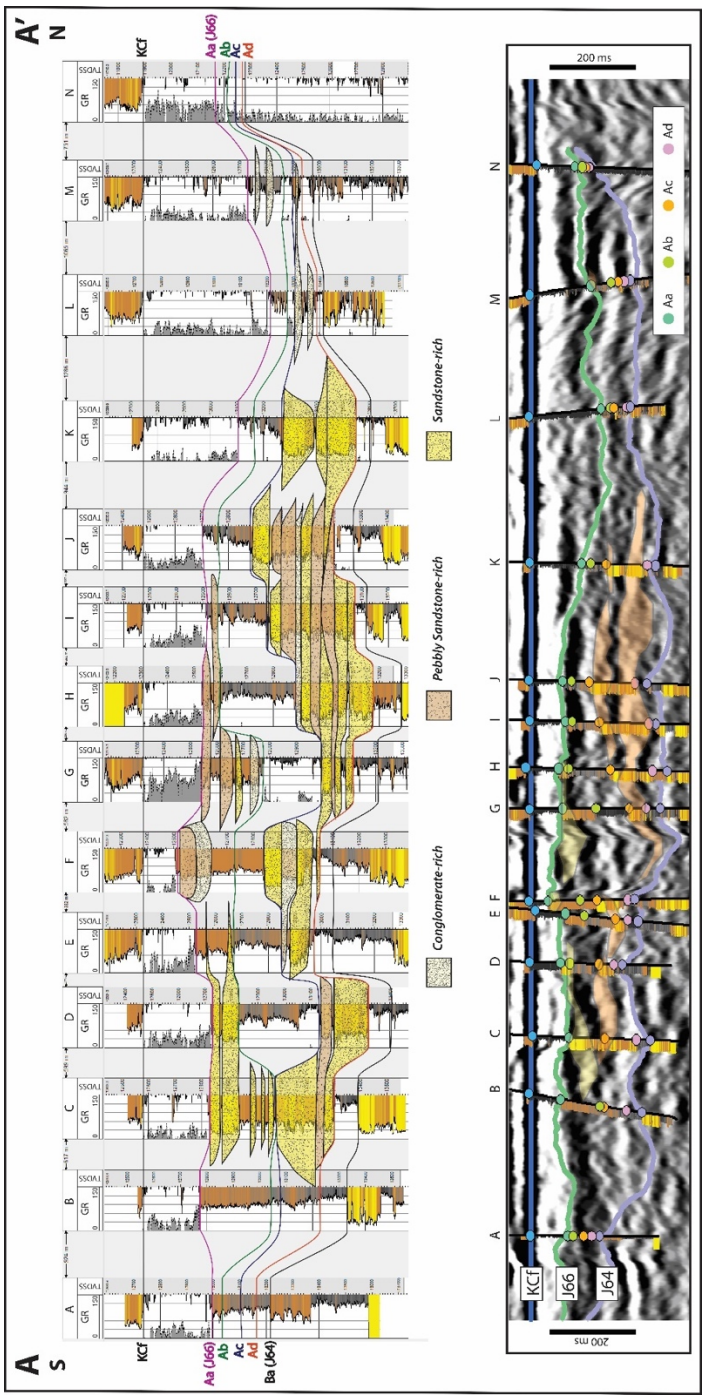

Figure 29: Dip-oriented stratigraphic cross-sections of the J66 sequence showing channel individuation in the Aa channel system and amalgamation in the Ac channel system. The interpreted channel complexes visible on an amplitude volume are highlighted on the seismic cross-section below. The yellow interpretations on seismic represents the identifiable channels within the Aa channel system and the orange interpretations represent the channels identifiable within the Ac channel system. The stratigraphic datum is the top of the Kimmeridge Clay Formation.

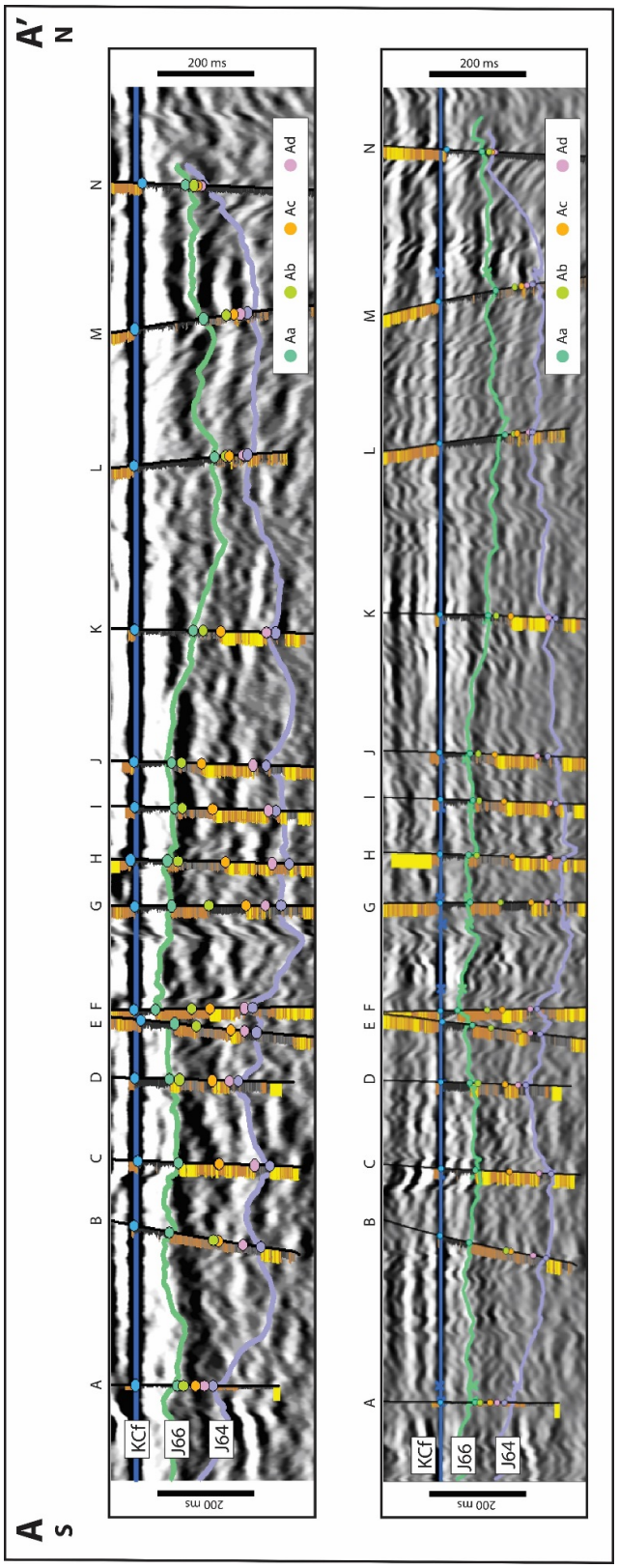

Figure 30: South-north cross-sections of original and spectrally-balanced volumes.

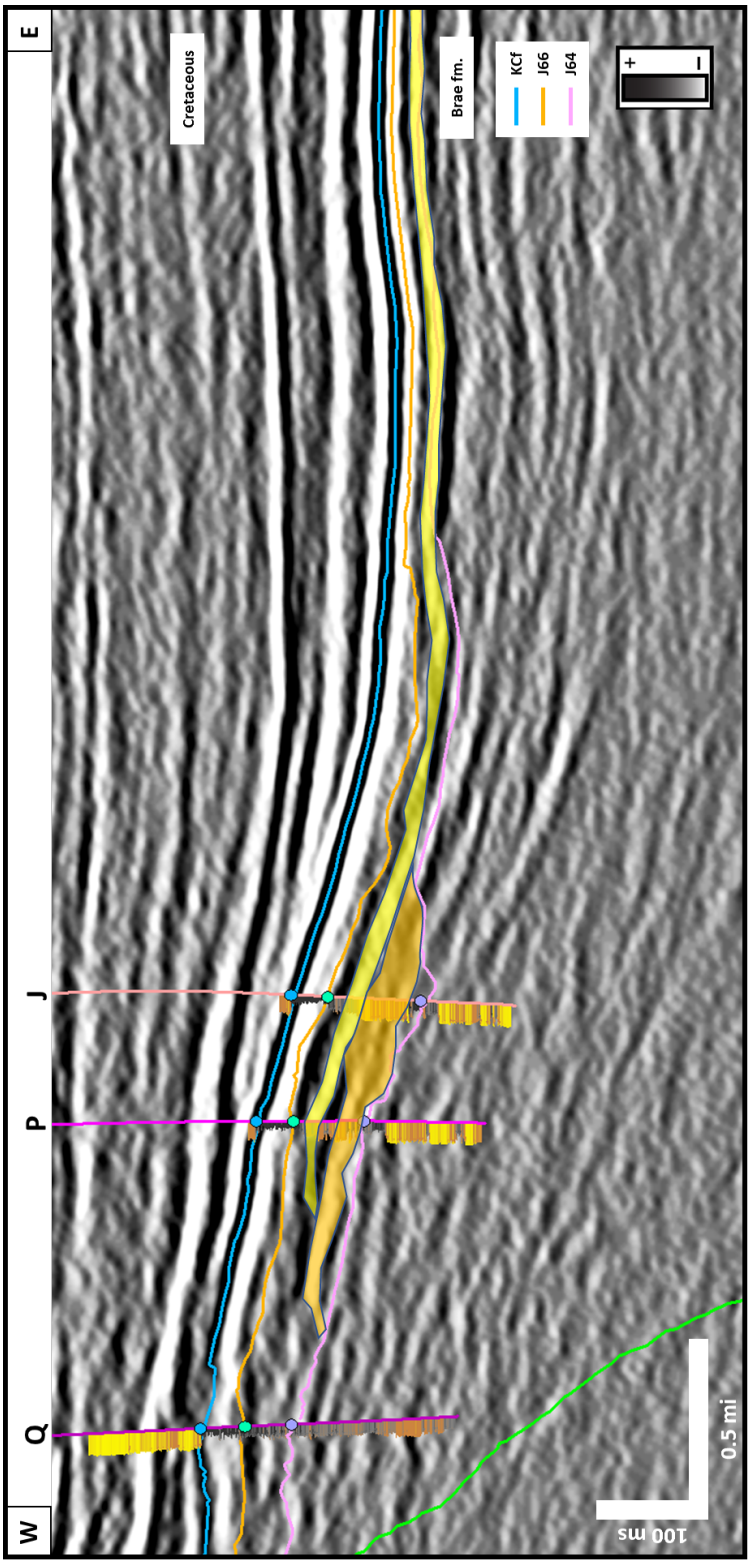

Figure 31: Strike-oriented cross-section. Yellow and orange interpretations are for Aa and Ac channel systems, respectively. Image is extracted from yellow box in Figure 26.

4.4. Electrofacies Distribution

The O-1 and O-2 wireline combinations using ANN – incorporating GR, DEN, NEU, PEF (where available) – were used to populate the facies at the available well locations (Table 1). This is because of the high precisions observed in the facies predicted using the classifier (Table 5). The relative electrofacies distributions were determined by defining the limits of the respective channel system using isopach maps. Relative proportions of the predicted facies were calculated and mapped within the channel boundary (Fig. 32 & 33). Fractional abundances were preferred to using facies thickness maps, as they better highlighted the depositional trends in each region of the channel system by showing the dominant lithofacies in each region. A facies map for each channel system was created to better explain reservoir trends and was corroborated with seismic (Fig. 28).

4.4.1. Ac System

The Ac channel system has an abundance of conglomerates deposited proximal to the foot-wall granite – within the first 2 miles. Two (2) point-sources feed the main fan with these conglomerates. Their abundances progressively reduce further into the basin and they are confined to narrow thalwegs flowing to the northeast and southeast. The pebbly sandstones show a similar pattern in the proximal areas. However, with progression into the basin, the thalwegs seen in the pebbly sandstones are wider. The sandstones appear to be sourced from just the southern source. The fairway splits into two about 2 miles into the basin. This bifurcation coincides with the presence of abundant shales, silty shales, and sandy siltstones. Their abundance increases with further progression into the basin, completely dominating the channel composition within the Miller field. Sandy siltstones are abundant at the channel-fan margins in

the proximal areas (Fig. 32). This suggests the channel-fan was deposited subsequent to the deposition of muddy turbidites (Turner et al., 1987; Fletcher, 2003).

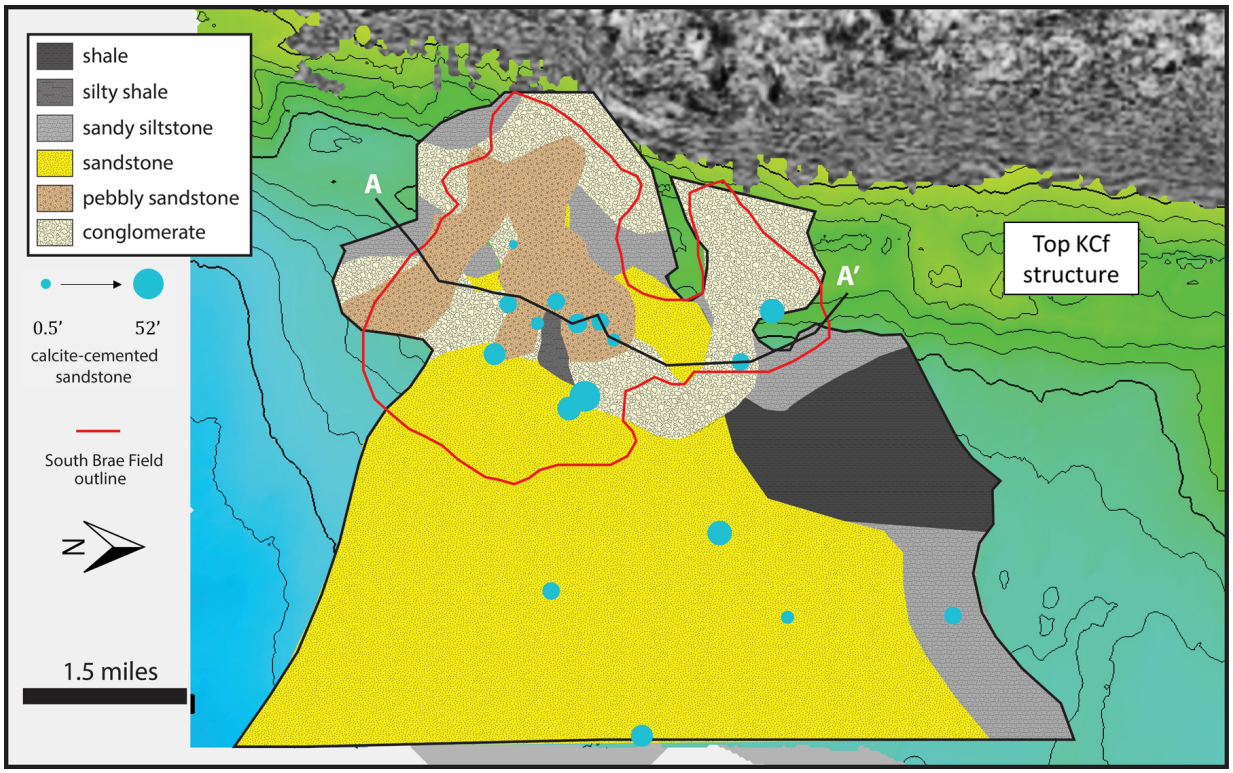

Figure 32: Facies map for the Ac system showing the dominant facies present. Calcite-cemented sandstones are highlighted in blue. Circle size indicates relative volume of concretions.

4.4.2. Aa System

The Aa channel system derives its sediment from a singular source – the southern point-source in the South Brae field. Three (3) channel fairways are apparent – southeastern, eastern, and northeastern flowing. The southeastern- and eastern-flowing channel belts have conglomerates that flow far into the basin. The pebbly sandstones spread out to form a fan-like deposit 1.5 miles away from the source. The fan terminates a further 1.5 miles into the basin. Sandstones also spread out to form a big fan and dominate the facies composition in the distal areas. The northeastern-flowing channel also has an abundance of conglomerates distal to the

source, and pebbly sandstones that appear to fan out and terminate. The sandstones in the distal areas are only present at the edges of the conglomerates (Fig. 33). As in the Ac channel system, the silty shales and sandy siltstones are abundant where the channel (reservoir) facies are absent and appear to dictate the bifurcations and channel flow directions in the proximal areas (Fig. 28).

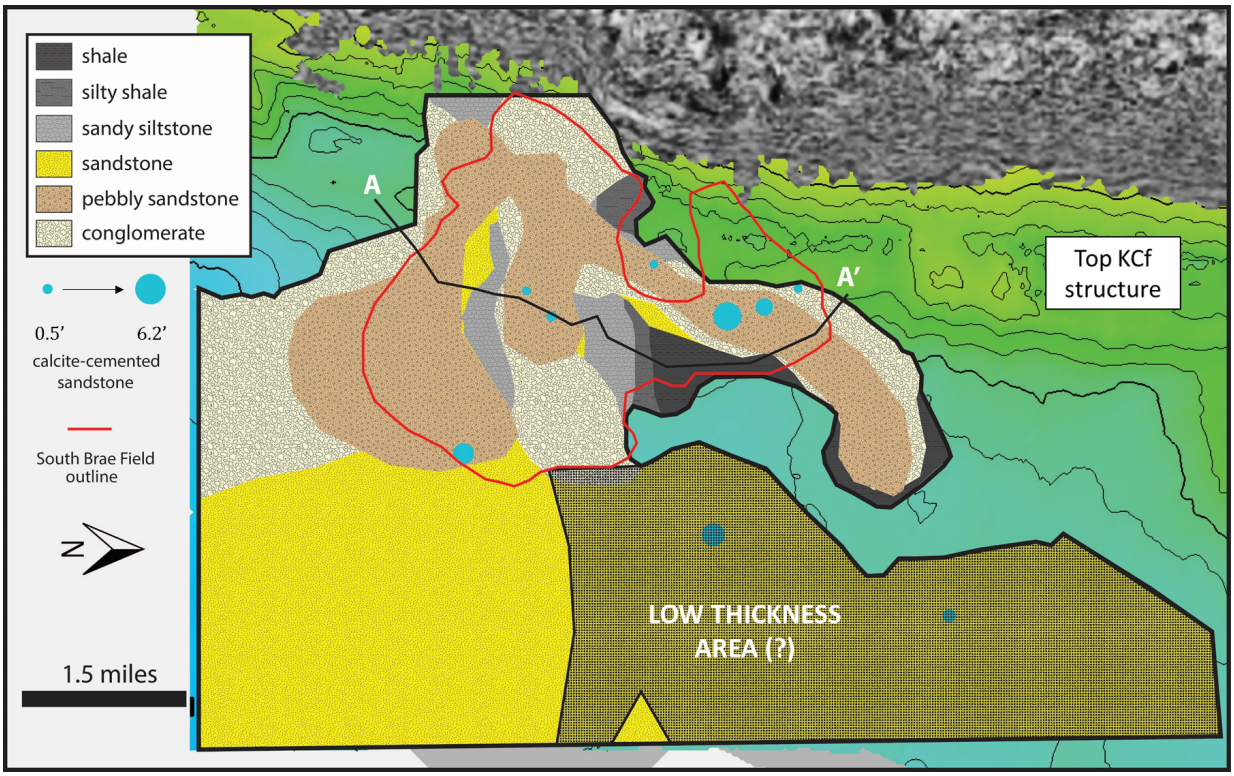

Figure 33: Facies map for the Aa channel system showing the dominant facies present. Calcite-cemented sandstones are highlighted in blue. Circle size indicates relative volume of concretions. The shaded region in the northwest is an area of relative lower thickness – as seen in the spectral decomposition results.

4.4.3. Concretion Distribution

The carbonate concretions are only observed in the Aa and Ac systems. They are mainly present in the sandy parts of the channel systems. More concretions are mapped within the Ac system compared to the Aa system. Concretions were observed in nine (9) wells within the Aa system (Fig. 33). The mean concretion thickness observed in wells with concretions is 2.7 feet.

The thickest concretion observed in the Aa system is 6.2 feet. Concretions are observed in eighteen (18) wells within the Ac system (Fig. 32). The mean thickness observed in well with concretions is 8.7 feet. The thickest concretion observed in the Ac system is 51.7 feet. The increased abundance and average thickness within the Ac system are likely due to the nature of the sandstone deposits. They are amalgamated and are deposited within a laterally extensive fan, allowing for mobility of the pore fluids that form the concretions (McLaughlin, 1992). Stratigraphically-confined concretions are also observed in other North Sea reservoirs (Slatt and Hopkins, 1990).

CONCLUSIONS

The Brae Formation in the South Brae field is comprised of seven (7) broad lithofacies that are representative of low- to high-density sandy debris flows and muddy turbidite deposition. These include: (1) shales, (2) silty shales, (3) sandy siltstones, (4) sandstones, (5) calcite cemented sandstones, (6) pebbly sandstones, and (7) conglomerates. The measured permeabilities and porosities indicate the sandstones and pebbly sandstones are the best reservoir facies. The conglomerates are possible reservoir facies as they have moderate porosities but low permeabilities. The calcite cemented sandstones occur in the form of concretions within the reservoir facies and lack porosity and permeability, likely requiring reservoir fluids to flow around them. They are observed primarily in the channel thalwegs.

Artificial neural networks and multi-variate cluster analysis show very high classification accuracies (~ 90 percent) regardless of the wireline log combination employed. Precision for facies classification is highest in artificial neural net and multi-variate cluster analysis classifications that incorporate GR, DEN, NEU, and PEF logs. This is because the addition of the PEF log includes relative mineralogical proportions in the classification. The lowest precision from both classifiers are observed in the silty shales, pebbly sandstones, and conglomerates. This is because they share part of their composition with other facies. The higher precisions observed in the ANN are due to the backpropagation that allows for reduction in classification error.

A sequence stratigraphic framework built with wireline logs and seismic highlights two major channel systems that form the primary reservoir rocks within the field. These channel systems are comprised of high- to medium-density debris flows. Within the J66 sequence, the channel systems are separated by sandy siltstones and silty shales deposited by muddy turbidites during periods of relative quiescence as sea level continued to rise. The lower channel system

within the J66 sequence, the Ac channel, is comprised of amalgamated channels from two point-sources that spread out to form a large, laterally extensive fan. The upper channel system, the Aa channel, exhibits relatively less amalgamation. One point-source feeds the entire system which splits into 3 separate channel belts that exhibit relatively less lateral connectivity within the South Brae field.

RECOMMENDATIONS FOR FUTURE WORK

Future studies should incorporate core that is available from other wells to possibly increase the accuracy of supervised classifications where core is unavailable. Abundant core data for classification could also allow for the testing of unsupervised classification techniques. Additionally, acquiring core data in wells with compressional and shear slowness logs would allow for the testing of the acoustic response to facies, and the response based on fluid content. Finally, fault sealing capacity or connectivity should be tested by acquiring available pressure data and incorporating that in delineating the different compartments within the reservoir.

REFERENCES

Blakey, R. C., 2012, Paleogeography of Europe: Colorado Plateau Geosystems: Deep Time Maps, web.

Brown, Stewart, 1991, Stratigraphy of the oil and gas reservoirs—U.K. continental shelf, in Abbotts, I.L., ed., United Kingdom oil and gas fields 25—years commemorative volume: London, Geological Society, Memoir 14, p. 9–18.

Carruthers, A., Mckie, T., Price, J., Dyer, R., Williams, G. & Watson, P., 1996, The application of sequence stratigraphy to the understanding of Late Jurassic turbidite plays in the Central North Sea, UKCS, in Hurst, A., Johnson, H. D., Burley, S. D., Canham, A. C. & Mackertich, D. S., eds*., Geology of the Humber Group: Central Graben and Moray Firth, UKCS*. Geological Society, London, Special Publications, 114, 29-45.

Cherry, S. T. J., 1993, The interaction of structure and sedimentary process controlling deposition of the Upper Jurassic Brae Formation Conglomerate, Block 16/17, North Sea, in J. R. Parker, ed., Petroleum geology of northwest Europe: Proceedings of the 4th Conference of the Geological Society (London), p. 387‑400.

Dubois, M. K., Bohling, G. C., Chakrabarti, S., 2007, Comparison of four approaches to a rock facies classification problem, *Computer & Geosciences*, 33, p. 599-617, doi: 10.1016/j.cageo.2006.08.011

Ekwunife, I., C., 2017, Assessing Mudrock Characteristics, High-Resolution Chemostratigraphy, and Sequence Stratigraphy of the Woodford Shale in McAlister Cemetery Quarry, Ardmore Basin, Oklahoma. Master's Thesis, University of Oklahoma, 152 p.

Eric Geoscience, inc., 2000, GAMLS (Geological Analysis via Maximum Likelihood System): User's Manual. Glenham, NY: Eslinger, E., Burdick, B., and Cooper, J.

Eslinger, E. and Pevear, D., 1988, Clay Minerals for Petroleum Geologists and Engineers, SEPM Short Course No. 22.

Eslinger, E., and R. V. Everett, 2012, Petrophysics in gas shales, in J. A. Breyer, ed., Shale reservoirs—Giant resources for the 21st century: AAPG Memoir 97, p. 419 – 451.

Fawcett, T., 2006, An Introduction to ROC Analysis. *Pattern Recognition Letters*. 27 (8): 861–874. doi: 10.1016/j.patrec.2005.10.010

Fletcher, K.J., 2003, The South Brae Field, Blocks 16/07a, 16/07b, UK North Sea, in Gluyas, J.G., and Hichens, H.M., eds., United Kingdom oil and gas fields, Commemorative Millennium Volume: Geological Society, London, Memoir, no. 20, p. 211-221.

Fraser, S. I., Robinson, A. M., Johnson, H. D., Underhill, J. R., Kadolsky, D. G. A., Connell, R., Johannessen, P, and Ravnas, R., 2003, Upper Jurassic, in Evans, D., Graham, C., Armour, A., and Bathhurst, P., eds., *The Millenium Atlas: petroleum geology of the central and northern North Sea*, The Geological Society of London, London, p. 157-189.

Gautier, D. L., 2005, Kimmeridgian Shales Total Petroleum System of the North Sea Graben Province: U.S. Geological Survey Bulletin 2204-C, 24 p.

Glennie, K. W., 1984, Structural framework and pre-Permian history of the North Sea area, in Glennie, K. W., ed., *Introduction to the Petroleum Geology of the North Sea*, Blackwell: Oxford, pp. 25-60.

Gonzalez, R. J., Reeves, S. R., Eslinger, E., & Garcia, G. S., 2007, Development and Application of an Integrated Clustering/Geostatistical Approach for 3D Reservoir Characterization, SACROC Unit, Permian Basin. Society of Petroleum Engineers. doi:10.2118/111453-MS

Gonzalez, R. J., Eslinger, E., Reeves, S. R., Schepers, K. C., & Back, T., 2008, Integrated Clustering/Geostatistical/Evolutionary Strategies Approach for 3D Reservoir Characterization and Assisted History-Matching in a Complex Carbonate Reservoir, SACROC Unit, Permian Basin. Society of Petroleum Engineers. doi:10.2118/113978-MS

Harms, J.C., Tackenberg, P., Pickles, E., and Pollock, R.E., 1981, The Brae Oilfield Area, in Illing, L.V., and Hobson, G.D., eds., *Petroleum geology of the continental shelf of Northwest Europe*: Heyden & Son Ltd, London, p. 352-357.

Jackson, C. A., E. Larsen, S. Hanslien, and A. Tjemsland, 2011, Controls on synrift turbidite deposition on the hanging wall of the South Viking Graben, North Sea rift system, offshore Norway: AAPG Bulletin, v. 95, no. 9, p. 1557-1587.

Laughlin, K., Garossino, P., and Partyka, G., 2002, Spectral Decomposition for Seismic Stratigraphic Patterns, AAPG Search and Discovery Article #40096

Lee, M.J., and Hwang, Y.J., 1993, Tectonic evolution and structural styles of the East Shetland Basin, in Parker, J.R., ed., Petroleum geology of Northwest Europe: Proceedings Fourth Conference, Geological Society, London, p. 1137-1158.

Lewis, D., 1991, Evaluating text categorization. In: Proc. Speech and Natural Language Workshop. Morgan Kaufmann, pp. 312–318.

Marfurt, K. J. and Matos, M. C., 2014, Spectral Balancing Can enhance Vertical Resolution. AAPG Search and Discovery #41357.

McClure, N. M., Brown, A. A., 1992, Miller Field: A Subtle Upper Jurassic Submarine Fan trap in the South Viking Graben, United Kingdom Sector, North Sea, *Giant Oil and Gas Fields of the Decade: 1978 – 1988.* AAPG Memoir 54, 307 – 322.

Mutti, E., 1985, Turbidite Systems and their relations to depositional Sequences, in Zuffa, G. G. ed., *Provenance of Arenites.* NATO ASI Series, Riedel Publishing Co. 65-93.

McLaughlin, O. M., 1992, Isotopic and textural evidence for diagenetic fluid mixing in the South Brae oilfield, North Sea. Doctoral dissertation, University of Glasgow, pp. 298.

Partington, M.A., Mitchener, B.C., Milton, N.J. and Fraser, A.J., 1993, Genetic sequence stratigraphy for the North Sea Late Jurassic and Early Cretaceous: distribution and prediction of Kimmeridgian-Late Ryazanian reservoirs in the North Sea and adjacent

areas. In: Parker, J.R. (ed) Petroleum Geology of Northwest Europe: Proceedings of the 4th Conference. The Geological Society, London, 347-370.

Partington, M. A., Copestake, P., Mitchener, B. C. And Underhill, J. R., 1993, Biostratigraphic calibration of genetic strati-graphic sequences in the Jurassic-lowermost Cretaceous (Hettangian to Ryazanian) of the North Sea and adjacent areas. *In:* Parker, J. R., ed., *Petroleum Geology of Northwest Europe: Proceedings of the 4th Conference.* Geological Society, London, 371-386.

Perlovsky, L. I., 1988, Cramer-Rao bounds for the estimation of means in a clustering problem, *Pattern Recognition Letters*: 8, p. 1-3.

Perlovsky, L. I., and McManus, M. M., 1991, Maximum Likelihood neural networks for sensor fusion and adaptive classification, *Neural Networks*: 4, 89-102.

Reading, H. G. and M. Richards, 1994, Turbidite Systems in Deep-Water Basin Margins Classified by Grain Size and Feeder System: AAPG Bulletin, v. 78, no. 5, p. 792-822.

Roberts, M. J., 1991, The South Brae Field, Block 16/7a, UK North Sea, in Abbotts, I. L. ed., United Kingdome Oil and Gas Fields, 25 Years Commemorative Volume: Geological Society Memoir: no. 14, pp. 55-62.

Rogers, S.J., Fang, J.H., Karr, C.L., Stanley, D.A., 1992, Determination of lithology from well logs using neural networks. *American Association of Petroleum Geologists Bulletin*: 76, 731–739.

Saggaf, M.M., Nebrija, E.L., 2000, Estimation of lithologies and depositional facies from wire-line logs. *American Association of Petroleum Geologists Bulletin*: 84, 1633–1646.

Shanmugam, G., 2016, Submarine fans: A critical retrospective (1950-2015), Journal of Paleogeography, vol. 5, no. 2, 110-184.

Slatt, R. M., and Hopkins, G. L., 1990, Scaling Geologic Reservoir Description to Engineering Needs. Society of Petroleum Engineers. doi:10.2118/18136-PA

Slatt, R. M., E. V. Eslinger, and S. K. Van Dyke, 2008, Acoustic and petrophysical properties of a clastic deep-water depositional system from lithofacies to architectural elements' scales: *GEOPHYSICS*, v. 74, no. 2, p. WA35 – WA50. doi:10.1190/1.3073760

Smith, K. and J. Ritchie, 1993, Jurassic volcanic centres in the Central North Sea, in Parker, J. ed., Petroleum Geology of Northwest Europe: Proceedings of the 4th conference, The Geological Society of London, pp. 519-531.

Stow, D.A.V., Bishop, C.D. and Mills, S.J., 1982, Sedimentology of the Brae Oilfield, North Sea: Fan models and controls. Journal of Petroleum Geology 5, 129 – 148.

Thomas, D.W., and M. P. Coward, 1996, Mesozoic regional tectonics and South Viking Graben formation: Evidence for localized thin-skinned detachments during rift development and inversion: Marine and Petroleum Geology, v. 13, p. 149–177. doi:10.1016/0264-8172(95)00034-8.

Turner, B. W., 2016, Utilization of chemostratigraphic proxies for generating and refining sequence stratigraphic frameworks in mudrocks and shales: Doctoral thesis, University of Oklahoma, Norman, 119p.

Turner, C.C., Cohen, J.M., Connell, E.R. and Cooper, D.M. 1987. A depositional model for the South Brae oilfield. In: Brooks, J. and Glennie, K. (eds) Petroleum Geology of North West Europe. Graham and Trotman Ltd, London. 853 – 864.

Turner, C.C. and Connell, E.R. 1991. Stratigraphic relationships between Upper Jurassic submarine fan sequences in the Brae Area, U.K. North Sea: The implications for reservoir distribution. Proceedings 23rd Annual Offshore Technology Conference, Houston, 83-91.

Turner, C.C., 2013, *Upper Jurassic depositional models, submarine fans and structure of the Brae area, South Viking Graben*, internal communication, Marathon Oil UK, Aberdeen, UK.

Turner, C. C, R. E. Bastidas, E. R. Connell, and F. E. Petrik, 2018, Proximal submarine fan reservoir architecture and development in the Upper Jurassic Brae Formation of the Brae Fields, South Viking Graben, U.K. North Sea, in Colin C. Turner and Bryan T. Cronin, eds., *Rift-related coarse-grained submarine fan reservoirs; the Brae Play, South Viking Graben, North Sea: Memoir 115*, p. -. doi:10.1306/13652183M1153807

US Energy Information Administration, 2016, *International Energy Statistics*. Web. Accessed October 11, 2018.

Vail, P. R., 1987, Seismic stratigraphy interpretation procedure, in Bally, A.W. (ed.), Atlas of seismic stratigraphy: AAPG Studies in Geology No. 27, Vol. 1, p. 1-10.

Vallejo, J. S., 2010, Prediction of lithofacies in the thinly bedded Barnett Shale, using probabilistic methods and clustering analysis through GAMLS^{TM} (Geologic Analysis via Maximum Likelihood System), M.S. Thesis, University of Oklahoma, Norman, Oklahoma, 184 p.

Wethington, N., 2017, Stratigraphic architecture of the Mississippian Limestone through integrated electrofacies classification, Hardtner Field Area, Kansas and Oklahoma, M.S. Thesis, University of Oklahoma, Norman, Oklahoma,103 p.

Zanella, E., and Coward, M.P., 2003, Structural Framework, in Evans, D., Graham, C., Armour, A., and Bathurst, P., eds., *The Millennium Atlas: petroleum geology of the central and northern North Sea*: Geological Society, London, p. 45-59.

Ziegler, P. A., 1975, The geological evolution of the North Sea area in the tectonic framework of North-Western Europe: Norwegian Geological Survey Bulletin, vol. 316, no. 29., pp. 1-27.

Ziegler, P. A., 1982, Faulting and graben formation in western and central Europe: Philosophical Transactions Royal Society London v. 305, no. 1489, p. 113-143. doi: 10.1098/rsta.1982.0029

Ziegler, P. A., 1990, Tectonic and paleogeographic development of the North Sea rift system, in D. Blundell and A. D. Gibbs, eds., Tectonic evolution of the North Sea rifts: Oxford, Clarendon Press, p. 1–36.

APPENDIX

A. Core-Plug Measurements

Log MD (ft)	Kh (mD)	Kv (mD)	Por. (%)	Grn. Den. (g/cc)	Lithofacies
19,276.05	347.00	-	14.9	2.64	Sandstone
19,277.00	419.00	370.00	13.9	2.64	Sandstone
19,278.00	451.00	-	14.7	2.65	Sandstone
19,279.05	400.00	-	13.9	2.64	Sandstone
19,281.00	370.00	-	13.7	2.65	Sandstone
19,282.00	358.00	287.00	14.0	2.65	Sandstone
19,283.00	372.00	-	13.7	2.65	Sandstone
19,284.00	185.00	-	12.8	2.64	Sandstone
19,285.00	57.90	-	11.2	2.64	Sandstone
19,286.00	495.00	-	14.4	2.64	Sandstone
19,287.00	958.00	371.00	15.0	2.65	Sandstone
19,288.00	580.00	-	14.2	2.63	Sandstone
19,289.05	496.00	-	14.3	2.64	Sandstone
19,290.00	144.00	-	12.2	2.63	Sandstone
19,291.00	430.00	-	14.7	2.65	Sandstone
19,292.00	371.00	306.00	14.3	2.64	Sandstone
19,293.00	272.00	-	14.0	2.65	Sandstone
19,294.00	260.00	-	13.4	2.63	Sandstone
19,295.00	226.00	-	13.4	2.63	Sandstone
19,296.00	253.00	-	14.0	2.65	Sandstone
19,297.00	325.00	311.00	14.1	2.65	Sandstone
19,298.00	277.00	-	14.2	2.65	Sandstone
19,299.05	379.00	-	14.7	2.65	Sandstone
19,300.00	346.00	-	13.8	2.64	Sandstone
19,301.00	294.00	-	13.9	2.64	Sandstone
19,303.00	242.00	375.00	13.1	2.64	Sandstone
19,304.00	398.00	-	13.9	2.64	Sandstone
19,305.00	420.00	-	14.4	2.65	Sandstone
19,306.00	501.00	-	14.7	2.64	Sandstone
19,307.00	532.00	523.00	14.2	2.63	Sandstone
19,308.00	255.00	-	14.5	2.64	Sandstone
19,309.00	151.00	-	14.1	2.64	Sandstone
19,309.95	1.26	-	8.4	2.65	Sandstone
19,310.80	5.66	-	9.9	2.64	Sandstone
19,313.00	672.00	676.00	15.3	2.64	Sandstone
19,314.00	445.00	-	14.5	2.64	Sandstone
19,315.00	511.00	-	14.4	2.63	Sandstone

19,316.00	647.00	-	15.0	2.64	Sandstone
19,316.85	435.00	47.70	14.5	2.64	Sandstone
19,318.00	375.00	-	13.7	2.64	Sandstone
19,319.00	107.00	-	12.2	2.64	Sandstone
19,320.00	626.00	-	15.1	2.65	Sandstone
19,321.00	504.00	-	14.2	2.63	Sandstone
19,322.00	590.00	472.00	15.0	2.64	Sandstone
19,322.50	698.00	-	15.2	2.66	Sandstone
19,322.80	42.00	-	12.7	2.66	Sandstone
19,322.95	642.00	-	14.9	2.66	Sandstone
19,323.35	512.00	-	14.2	2.64	Sandstone
19,324.00	671.00	-	15.3	2.65	Sandstone
19,325.00	814.00	-	15.5	2.64	Sandstone
19,325.65	550.00	-	13.5	2.64	Sandstone
19,335.95	405.00	403.00	13.6	2.65	Sandstone
19,339.00	1050.00	-	13.7	2.64	Sandstone
19,340.00	444.00	283.00	13.1	2.64	Sandstone
19,341.00	493.00	-	14.4	2.64	Sandstone
19,342.00	183.00	-	12.2	2.63	Sandstone
19,343.00	353.00	-	14.1	2.64	Sandstone
19,343.95	603.00	-	14.2	2.64	Sandstone
19,345.00	655.00	1040.00	15.2	2.64	Sandstone
19,345.30	663.00	-	15.2	2.66	Sandstone
19,346.20	715.00	-	14.5	2.64	Sandstone
19,347.00	672.00	-	13.9	2.63	Sandstone
19,348.00	613.00	-	14.7	2.65	Sandstone
19,349.00	516.00	-	14.0	2.63	Sandstone
19,350.00	413.00	517.00	13.9	2.64	Sandstone
19,351.00	752.00	-	15.0	2.65	Sandstone
19,352.00	289.00	-	13.1	2.63	Sandstone
19,353.00	680.00	-	15.0	2.65	Sandstone
19,354.00	506.00	-	14.2	2.64	Sandstone
19,355.00	489.00	420.00	14.1	2.64	Sandstone
19,356.00	335.00	-	13.9	2.64	Sandstone
19,356.65	356.00	-	13.8	2.64	Sandstone
19,356.90	400.00	-	13.7	2.67	Sandstone
19,357.10	767.00	-	16.0	2.66	Sandstone
19,357.30	394.00	-	14.7	2.65	Sandstone
19,358.00	124.00	-	13.3	2.65	Sandstone
19,359.00	77.10	-	11.8	2.65	Sandstone
19,360.00	865.00	781.00	15.0	2.64	Sandstone

19,361.00	643.00	-	14.5	2.65	Sandstone
19,362.00	562.00	-	14.7	2.65	Sandstone
19,363.00	283.00	-	13.4	2.64	Sandstone
19,364.00	492.00	-	14.5	2.64	Sandstone
19,365.00	372.00	301.00	13.8	2.64	Sandstone
19,366.00	300.00	-	13.3	2.64	Sandstone
19,367.00	512.00	-	14.5	2.63	Sandstone
19,368.00	550.00	-	15.0	2.65	Sandstone
19,369.00	443.00	-	14.2	2.63	Sandstone
19,370.00	251.00	351.00	14.1	2.64	Sandstone
19,371.00	28.70	-	10.7	2.64	Sandstone
19,372.00	117.00	-	13.1	2.64	Sandstone
19,373.00	746.00	-	16.3	2.65	Sandstone
19,374.00	592.00	-	15.0	2.64	Sandstone
19,375.00	522.00	463.00	12.6	2.65	Sandstone
19,375.95	810.00	-	15.2	2.64	Sandstone
19,377.00	307.00	-	13.1	2.64	Sandstone
19,377.90	49.80	-	10.1	2.63	Sandstone
19,379.00	877.00	-	15.0	2.63	Sandstone
19,380.00	859.00	668.00	15.2	2.64	Sandstone
19,381.00	723.00	-	15.0	2.64	Sandstone
19,382.00	585.00	-	14.1	2.63	Sandstone
19,383.00	859.00	-	14.3	2.64	Sandstone
19,384.00	1340.00	-	15.1	2.64	Sandstone
19,385.00	532.00	335.00	14.0	2.65	Sandstone
19,386.00	377.00	-	13.8	2.64	Sandstone
19,387.00	424.00	-	13.9	2.65	Sandstone
19,388.00	524.00	-	14.3	2.64	Sandstone
19,389.00	422.00	-	13.5	2.64	Sandstone
19,390.00	301.00	192.00	13.1	2.63	Sandstone
19,391.00	15.20	-	12.9	2.65	Sandstone
19,392.00	83.40	-	14.5	2.63	Sandstone
19,393.40	113.00	-	13.9	2.63	Sandstone
19,394.00	400.00	-	16.2	2.64	Sandstone
19,395.10	2.21	2.55	11.4	2.64	Sandstone
19,399.95	702.00	84.50	16.6	2.64	Sandstone
19,400.10	647.00	674.00	16.4	2.64	Sandstone
19,401.00	652.00	-	16.3	2.64	Sandstone
19,402.00	2.33	-	9.7	2.63	Sandstone
19,403.00	478.00	-	16.4	2.64	Sandstone
19,404.15	462.00	-	15.5	2.64	Sandstone

19,405.00	372.00	284.00	14.7	2.65	Sandstone
19,406.00	763.00	-	15.5	2.65	Sandstone
19,407.00	682.00	-	15.6	2.65	Sandstone
19,408.00	568.00	-	15.0	2.65	Sandstone
19,409.00	359.00	-	14.3	2.64	Sandstone
19,410.00	303.00	295.00	13.7	2.64	Sandstone
19,411.00	138.00	-	13.7	2.64	Sandstone
19,412.00	529.00	-	14.8	2.64	Sandstone
19,412.95	743.00	-	15.4	2.64	Sandstone
19,414.00	622.00	-	15.0	2.63	Sandstone
19,415.00	383.00	512.00	14.4	2.65	Sandstone
19,415.95	-	-	8.8	2.65	Sandstone
19,417.00	36.20	-	14.4	2.65	Sandstone
19,418.00	2.20	-	9.8	2.64	Sandstone
19,419.00	418.00	-	16.3	2.64	Sandstone
19,420.00	314.00	279.00	15.7	2.65	Sandstone
19,421.00	403.00	-	15.2	2.64	Sandstone
19,422.25	468.00	-	15.6	2.65	Sandstone
19,423.00	484.00	-	14.4	2.65	Sandstone
19,424.00	481.00	-	14.4	2.64	Sandstone
19,425.00	34.90	59.10	10.6	2.64	Sandstone
19,426.00	349.00	-	14.7	2.64	Sandstone
19,427.05	440.00	-	15.3	2.65	Sandstone
19,428.00	432.00	-	14.7	2.64	Sandstone
19,429.00	378.00	317.00	14.6	2.65	Sandstone
19,430.00	290.00	-	14.6	2.65	Sandstone
19,431.00	450.00	-	14.7	2.64	Sandstone
19,432.00	460.00	-	15.1	2.64	Sandstone
19,432.95	478.00	-	15.3	2.65	Sandstone
19,434.00	227.00	-	13.3	2.64	Sandstone
19,435.00	579.00	548.00	14.7	2.64	Sandstone
19,436.45	412.00	-	14.2	2.65	Sandstone
19,437.00	904.00	-	16.5	2.65	Sandstone
19,438.00	325.00	-	13.1	2.64	Sandstone
19,439.00	359.00	-	13.7	2.64	Sandstone
19,440.00	394.00	338.00	13.8	2.64	Sandstone
19,441.00	494.00	-	13.8	2.64	Sandstone
19,442.00	0.17	-	1.9	2.66	Calcite-Cemented Sandstone
19,442.95	0.20	-	1.4	2.67	Calcite-Cemented Sandstone
19,444.00	0.20	-	1.4	2.66	Calcite-Cemented Sandstone
19,445.00	0.17	0.20	1.7	2.67	Calcite-Cemented Sandstone

19,446.00	0.19	-	1.7	2.66	Calcite-Cemented Sandstone
19,447.00	0.29	-	2.2	2.65	Calcite-Cemented Sandstone
19,448.00	2.89	-	6.2	2.65	Calcite-Cemented Sandstone
19,449.00	353.00	-	12.8	2.65	Sandstone
19,449.90	105.00	-	9.5	2.58	Sandstone
19,451.00	460.00	293.00	13.3	2.64	Sandstone
19,452.00	163.00	-	15.2	2.59	Sandstone
19,453.00	656.00	-	14.1	2.65	Sandstone
19,454.00	702.00	-	14.4	2.65	Sandstone
19,455.00	670.00	443.00	13.7	2.65	Sandstone
19,456.00	744.00	-	14.0	2.64	Sandstone
19,457.00	462.00	-	12.1	2.61	Sandstone
19,457.95	787.00	-	14.4	2.65	Sandstone
19,459.00	741.00	-	14.1	2.65	Sandstone
19,460.90	637.00	313.00	12.8	2.63	Sandstone
19,461.10	474.00	-	12.5	2.64	Sandstone
19,462.00	218.00	-	10.4	2.63	Sandstone
19,463.00	402.00	-	12.2	2.63	Sandstone
19,464.00	231.00	617.00	12.2	2.66	Pebbly Sandstone
19,465.40	30.90	-	8.3	2.58	Pebbly Sandstone
19,466.00	282.00	-	11.8	2.64	Pebbly Sandstone
19,467.00	493.00	-	13.1	2.66	Pebbly Sandstone
19,468.00	306.00	-	12.0	2.61	Pebbly Sandstone
19,469.00	10.60	-	7.0	2.58	Pebbly Sandstone
19,470.00	839.00	545.00	14.2	2.65	Pebbly Sandstone
19,471.00	180.00	-	10.6	2.65	Pebbly Sandstone
19,472.00	609.00	-	13.3	2.63	Pebbly Sandstone
19,473.00	123.00	-	11.5	2.64	Pebbly Sandstone
19,474.00	152.00	-	10.3	2.63	Pebbly Sandstone
19,475.00	343.00	244.00	12.2	2.64	Pebbly Sandstone
19,476.00	496.00	-	12.8	2.63	Pebbly Sandstone
19,477.00	423.00	-	12.2	2.63	Pebbly Sandstone
19,478.00	718.00	-	13.1	2.64	Pebbly Sandstone
19,479.00	480.00	-	12.3	2.63	Pebbly Sandstone
19,480.00	645.00	147.00	13.7	2.65	Pebbly Sandstone
19,481.00	414.00	-	11.9	2.64	Pebbly Sandstone
19,482.00	683.00	-	13.5	2.64	Pebbly Sandstone
19,483.05	503.00	-	13.3	2.64	Pebbly Sandstone
19,484.00	720.00	-	14.3	2.64	Pebbly Sandstone
19,485.00	866.00	671.00	13.9	2.63	Pebbly Sandstone
19,486.00	1080.00	-	14.8	2.65	Pebbly Sandstone

19,487.10	640.00	-	14.4	2.63	Pebbly Sandstone
19,488.00	802.00	-	13.8	2.64	Pebbly Sandstone
19,489.00	908.00	-	14.6	2.64	Pebbly Sandstone
19,490.00	800.00	949.00	14.3	2.63	Pebbly Sandstone
19,496.05	70.40	-	10.5	2.64	Pebbly Sandstone
19,497.00	31.10	37.30	12.1	2.65	Pebbly Sandstone
19,498.00	27.90	-	10.5	2.66	Pebbly Sandstone
19,499.35	131.00	-	11.5	2.64	Pebbly Sandstone
19,500.00	77.00	-	12.3	2.65	Sandstone
19,501.00	98.70	-	12.8	2.65	Sandstone
19,502.00	136.00	114.00	13.2	2.65	Sandstone
19,503.00	113.00	-	13.3	2.64	Sandstone
19,504.00	83.40	-	13.0	2.66	Sandstone
19,505.00	90.10	-	12.5	2.65	Sandstone
19,506.00	92.20	-	12.3	2.64	Sandstone
19,507.00	117.00	99.20	13.7	2.65	Sandstone
19,508.00	102.00	-	12.5	2.63	Sandstone
19,509.00	96.40	-	12.8	2.65	Sandstone
19,510.00	55.60	-	12.2	2.65	Sandstone
19,511.00	82.90	-	11.6	2.66	Sandstone
19,512.00	79.10	103.00	12.4	2.65	Sandstone
19,513.00	49.90	-	12.0	2.66	Sandstone
19,514.00	57.60	-	12.1	2.66	Sandstone
19,515.00	12.20	-	10.5	2.67	Sandstone
19,516.00	41.40	-	11.8	2.65	Sandstone
19,517.00	70.40	53.80	12.3	2.65	Sandstone
19,519.00	6.29	-	8.9	2.65	Sandstone
19,520.00	316.00	-	14.4	2.65	Sandstone
19,521.00	71.00	-	12.6	2.66	Sandstone
19,521.50	86.50	117.00	12.7	2.66	Sandstone
19,522.00	121.00	205.00	12.4	2.65	Sandstone
19,523.00	244.00	-	12.7	2.65	Sandstone
19,524.00	224.00	-	13.2	2.66	Sandstone
19,524.75	241.00	-	13.1	2.66	Sandstone
19,526.00	198.00	-	12.4	2.65	Sandstone
19,527.00	177.00	154.00	12.2	2.65	Sandstone
19,528.00	202.00	-	12.6	2.67	Sandstone
19,529.00	158.00	-	12.0	2.67	Sandstone
19,530.00	245.00	-	12.4	2.65	Sandstone
19,531.00	195.00	-	12.0	2.66	Sandstone
19,532.00	163.00	68.00	11.9	2.64	Sandstone

19,533.00	103.00	-	11.8	2.67	Sandstone
19,534.00	185.00	-	12.1	2.67	Sandstone
19,535.00	266.00	-	12.3	2.64	Sandstone
19,536.00	194.00	-	12.3	2.66	Sandstone
19,537.00	255.00	184.00	12.6	2.64	Sandstone
19,538.00	110.00	-	11.7	2.68	Sandstone
19,539.00	128.00	-	11.8	2.64	Sandstone
19,540.50	122.00	-	11.4	2.65	Sandstone
19,541.00	86.00	-	10.8	2.64	Sandstone
19,542.00	97.30	49.20	11.4	2.62	Sandstone
19,543.00	40.00	-	9.9	2.65	Sandstone
19,544.00	57.80	-	10.5	2.65	Sandstone
19,545.15	139.00	-	12.1	2.66	Sandstone
19,546.00	74.70	-	11.8	2.65	Sandstone
19,547.00	39.60	3.02	11.6	2.65	Sandstone
19,548.00	114.00	-	12.5	2.65	Sandstone
19,549.00	91.00	-	12.1	2.67	Sandstone
19,550.00	120.00	-	12.2	2.65	Sandstone
19,551.00	99.70	-	12.0	2.64	Sandstone
19,552.00	131.00	53.00	12.6	2.65	Sandstone
19,553.00	122.00	-	12.8	2.65	Sandstone
19,554.00	97.00	-	11.8	2.65	Sandstone
19,555.00	244.00	-	13.3	2.64	Sandstone
19,556.00	124.00	-	12.6	2.65	Sandstone
19,557.00	170.00	141.00	12.8	2.66	Sandstone
19,558.00	146.00	-	12.4	2.64	Sandstone
19,559.00	125.00	-	12.5	2.65	Sandstone
19,560.00	23.50	-	8.9	2.57	Sandstone
19,561.00	163.00	-	12.5	2.66	Sandstone
19,562.00	141.00	113.00	12.4	2.64	Sandstone
19,563.00	144.00	-	12.4	2.65	Sandstone
19,564.00	296.00	-	13.7	2.64	Sandstone
19,565.00	129.00	-	12.3	2.64	Sandstone
19,566.00	21.50	-	8.6	2.58	Sandstone
19,567.00	57.20	57.60	10.9	2.64	Sandstone
19,568.00	24.00	-	9.6	2.64	Sandstone
19,569.00	75.50	-	11.8	2.64	Sandstone
19,570.00	45.00	-	10.3	2.65	Sandstone
19,571.00	15.40	-	9.1	2.65	Sandstone
19,572.00	31.60	65.30	11.1	2.64	Sandstone
19,573.00	37.90	-	11.1	2.64	Sandstone

19,573.65	44.20	-	11.2	2.64	Sandstone
19,575.10	35.50	-	10.9	2.64	Sandstone
19,576.00	28.80	29.30	10.9	2.65	Sandstone
19,577.00	2.16	-	7.5	2.65	Sandstone
19,578.00	9.77	-	10.9	2.65	Sandstone
19,579.00	54.80	-	12.2	2.65	Sandstone
19,580.00	53.30	-	11.5	2.65	Sandstone
19,581.00	44.70	42.90	11.5	2.67	Sandstone
19,581.90	38.20	-	11.0	2.67	Sandstone
19,583.00	52.80	-	11.7	2.65	Sandstone
19,584.00	62.60	-	11.4	2.65	Sandstone
19,585.15	77.20	-	11.8	2.65	Sandstone
19,586.00	67.60	58.10	11.6	2.65	Sandstone
19,587.00	40.00	-	10.4	2.66	Sandstone
19,588.00	12.70	-	10.7	2.67	Pebbly Sandstone
19,589.00	4.27	-	6.6	2.67	Pebbly Sandstone
19,590.00	114.00	-	11.9	2.64	Sandstone
19,591.00	66.50	123.00	10.8	2.72	Sandstone
19,592.00	93.30	-	11.6	2.64	Sandstone
19,593.00	104.00	-	11.2	2.64	Sandstone
19,594.00	26.90	-	7.4	2.65	Conglomerate
19,594.05	1.81	-	4.2	2.67	Conglomerate
19,594.20	4.63	-	5.7	2.66	Conglomerate
19,594.55	119.00	-	10.2	2.66	Conglomerate
19,595.00	60.60	-	8.7	2.66	Conglomerate
19,596.00	41.10	32.70	11.0	2.65	Sandstone
19,597.00	34.90	-	10.3	2.64	Sandstone
19,598.00	38.80	-	10.8	2.65	Sandstone
19,599.00	25.30	-	10.6	2.66	Sandstone
19,600.00	2.97	-	7.0	2.66	Conglomerate
19,601.00	47.10	36.10	11.3	2.65	Sandstone
19,602.20	12.30	-	10.8	2.66	Sandstone
19,603.10	4.34	-	10.0	2.66	Sandstone
19,604.00	34.60	-	12.1	2.67	Sandstone
19,605.00	23.50	-	11.1	2.68	Sandstone
19,606.00	20.20	19.00	11.0	2.65	Sandstone
19,606.95	19.80	-	10.7	2.65	Sandstone
19,608.00	9.55	-	10.3	2.65	Sandstone
19,609.00	2.81	-	7.3	2.64	Sandstone
19,610.00	59.30	-	11.7	2.65	Sandstone
19,611.00	49.70	44.60	11.2	2.67	Sandstone

19,612.00	45.20	-	11.2	2.66	Sandstone
19,613.00	48.90	-	11.1	2.67	Sandstone
19,614.00	24.10	-	10.4	2.70	Sandstone
19,615.00	17.10	-	9.8	2.69	Sandstone
19,615.95	54.20	28.80	11.5	2.66	Sandstone
19,617.00	-	-	11.2	2.67	Sandstone
19,618.00	49.60	-	11.2	2.68	Sandstone
19,619.10	54.50	-	11.7	2.65	Sandstone
19,620.00	8.73	-	7.2	2.65	Pebbly Sandstone
19,621.00	11.80	-	8.0	2.66	Pebbly Sandstone
19,622.00	24.00	18.70	9.3	2.65	Pebbly Sandstone
19,623.00	19.60	-	9.9	2.65	Pebbly Sandstone
19,624.00	14.70	-	7.9	2.66	Pebbly Sandstone
19,625.00	27.30	-	9.4	2.64	Pebbly Sandstone
19,626.00	19.00	-	9.9	2.65	Pebbly Sandstone
19,627.00	10.10	6.83	6.0	2.69	Conglomerate
19,628.00	12.70	-	8.4	2.65	Conglomerate
19,629.00	6.88	-	8.4	2.65	Conglomerate
19,630.00	4.75	-	7.9	2.66	Conglomerate
19,631.00	12.30	-	7.5	2.66	Conglomerate
19,632.00	10.80	5.11	8.7	2.65	Conglomerate
19,633.20	2.02	-	6.1	2.67	Conglomerate
19,634.00	7.60	-	7.6	2.66	Conglomerate
19,635.00	6.84	-	7.5	2.66	Conglomerate
19,636.00	6.70	-	6.8	2.65	Conglomerate
19,637.00	7.15	6.60	8.8	2.66	Conglomerate
19,638.00	6.38	-	7.0	2.67	Conglomerate
19,639.00	4.56	-	5.9	2.67	Conglomerate
19,640.00	2.77	-	5.7	2.68	Conglomerate
19,641.00	7.28	-	7.6	2.66	Conglomerate
19,642.00	7.54	4.67	7.9	2.67	Conglomerate
19,644.00	4.38	-	6.8	2.67	Conglomerate
19,653.95	0.16	0.12	2.6	2.68	Sandy Siltstone
19,665.90	0.21	0.15	4.4	2.68	Sandy Siltstone
19,667.10	-	-	5.2	2.66	Sandy Siltstone
19,675.55	0.07	0.11	1.7	2.67	Silty Shale
19,678.30	0.17	-	4.3	2.68	Sandy Siltstone

Table A: Core-plug measurements. Horizontal (parallel to bedding) and vertical (perpendicular to bedding) permeabilities, porosity, and grain density are measured.

B. X-Ray Diffraction Analysis

MD (ft)	Sample	Lithofacies	Qz(%)	Cal(%)	Dol(%)	Ab(%)	An(%)	Ocl(%)	Msc(%)	Py (%)	Clay(%)
19338.9	**ALQ1**	Sandstone	84.3	0.2	0.1	2.4	7.7	1.7	1.3	0.4	1.8
19395.5	**ALQ2**	Sandstone	93.9	0.5	0.2	0.4	0.5	0.1	3	0.1	1.2
19418	**ALQ3**	Sandstone	76.5	0.9	1.7	0.9	0.1	3.8	1	0.5	14.5
19431.9	**ALQ4**	Sandstone	85.1	0.2	0.1	1.5	2.9	5.5	0.7	0.1	3.9
19446.8	**ALQ4B**	Cal. cmt. Sandstone	72.1	17.7	0.1	2.3	1.5	0.3	3.2	0.5	2.4
19471.1	**ALQ5**	Pebbly Sandstone	89.2	0.5	0.1	2	1.7	0.5	3.7	0.2	2.2
19485.2	**ALQ6**	Pebbly Sandstone	94.2	0.5	0.2	0.1	0.1	1.9	0.5	1	1.6
19495.3	**ALQ7**	Pebbly Sandstone	90.4	0.1	0.1	0.2	1.2	5.5	1	0.1	1.5
19519.4	**ALQ7B**	Sandstone	83.6	0.2	0.1	6.9	0.2	0.2	0.2	0.1	8.5
19582	**ALQ7C**	Sandstone	54.1	1.7	4	2.8	1	7.1	14.2	8.5	6.5
19638.2	**ALQ8**	Conglomerate	79.5	0.2	0.6	0.7	0.2	5.3	6.4	0.2	6.8
19640.8	**ALQ9**	Conglomerate	84.3	0.5	0.3	0.5	0.2	1	2	0.5	10.7
19655.3	**ALQ10**	Sandy Siltstone	60.3	0.5	8.5	2.1	2.1	2.6	1.4	0.1	22.3
19655.3	**ALQ10CLAY**	Sandy Siltstone	41.3	1.3	5.2	3.1	0.1	4.6	1.8	5.2	37.4
19688.3	**ALQ11**	Silty Shale	42.6	0.4	5.2	1.6	0.1	12.4	3.1	0.5	34.2
19687.4	**ALQ12**	Silty Shale	39.6	0.4	2.1	5.8	5.2	10.5	5.2	3.8	27.4

Table B: XRD analysis of Well O. Percent volumes of Qz (quartz), Cal (calcite), Dol (dolomite), Ab (albite), An (anorthite), Ocl (orthoclase), Msc (muscovite), Py (pyrite), and clays are measured.

C. Confusion Matrices

C-1. Multi-Variate Cluster Analysis

Accuracy		Prediction						
92.2%		Shale	Silt-Shale	Sand-Silt	Sandstone	Cal. Cmt. Sst.	Pebbly Sandstone	Conglomerate
Actual	Shale	447	0	0	0	0	0	0
	Silt-Shale	0	23	5	0	0	0	0
	Sand-Silt	0	9	62	0	0	0	0
	Sandstone	0	0	3	742	0	8	9
	Cal. Cmt. Sst.	0	0	0	0	12	0	0
	Pebbly Sandstone	0	0	0	69	0	11	8
	Conglomerate	0	0	0	2	0	1	44
Precision		100.0%	71.9%	88.6%	91.3%	100.0%	55.0%	72.1%

Table C-1.1: Confusion matrix for MVCA classification using GR, DEN, NEU

Accuracy		Prediction						
92.3%		Shale	Silt-Shale	Sand-Silt	Sandstone	Cal. Cmt. Sst.	Pebbly Sandstone	Conglomerate
Actual	Shale	447	0	0	0	0	0	0
	Silt-Shale	0	24	4	0	0	0	0
	Sand-Silt	0	6	65	0	0	0	0
	Sandstone	0	0	2	741	1	10	8
	Cal. Cmt. Sst.	0	0	0	0	12	0	0
	Pebbly Sandstone	0	0	0	69	0	9	10
	Conglomerate	0	0	0	2	0	0	45
Precision		100.0%	80.0%	91.5%	91.3%	92.3%	47.4%	71.4%

Table C-1.2: Confusion matrix for MVCA classification using GR, DEN, NEU, PEF

Accuracy		Prediction						
91.1%		Shale	Silt-Shale	Sand-Silt	Sandstone	Cal. Cmt. Sst.	Pebbly Sandstone	Conglomerate
Actual	Shale	445	0	2	0	0	0	0
	Silt-Shale	0	21	7	0	0	0	0
	Sand-Silt	0	10	61	0	0	0	0
	Sandstone	1	0	3	731	0	7	20
	Cal. Cmt. Sst.	0	0	0	0	12	0	0
	Pebbly Sandstone	0	0	0	64	0	11	13
	Conglomerate	0	0	0	2	0	0	45
Precision		99.8%	67.7%	83.6%	91.7%	100.0%	61.1%	57.7%

Table C-1.3: Confusion matrix for MVCA classification using GR, DEN, NEU, Vp

Accuracy		Prediction						
91.7%		Shale	Silt-Shale	Sand-Silt	Sandstone	Cal. Cmt. Sst.	Pebbly Sandstone	Conglomerate
Actual	Shale	447	0	0	0	0	0	0
	Silt-Shale	0	20	8	0	0	0	0
	Sand-Silt	1	5	65	0	0	0	0
	Sandstone	3	0	0	736	0	7	16
	Cal. Cmt. Sst.	0	0	0	0	10	0	2
	Pebbly Sandstone	0	0	0	64	0	11	13
	Conglomerate	0	0	0	1	0	1	45
Precision		99.1%	80.0%	89.0%	91.9%	100.0%	57.9%	59.2%

Table C-1.4: Confusion matrix for MVCA classification using GR, DEN, NEU, PEF, Vp

Accuracy		Prediction						
92.2%		Shale	Silt-Shale	Sand-Silt	Sandstone	Cal. Cmt. Sst.	Pebbly Sandstone	Conglomerate
Actual	Shale	447	0	0	0	0	0	0
	Silt-Shale	0	23	5	0	0	0	0
	Sand-Silt	0	9	62	0	0	0	0
	Sandstone	0	0	3	742	0	8	9
	Cal. Cmt. Sst.	0	0	0	0	12	0	0
	Pebbly Sandstone	0	0	0	69	0	11	8
	Conglomerate	0	0	0	2	0	1	44
Precision		100.0%	71.9%	88.6%	91.3%	100.0%	55.0%	72.1%

Table C-1.5: Confusion matrix for MVCA classification using VShale, PHID.c, PHIN.c

Accuracy		Prediction						
92.3%		Shale	Silt-Shale	Sand-Silt	Sandstone	Cal. Cmt. Sst.	Pebbly Sandstone	Conglomerate
Actual	Shale	447	0	0	0	0	0	0
	Silt-Shale	0	24	4	0	0	0	0
	Sand-Silt	0	6	65	0	0	0	0
	Sandstone	0	0	2	741	1	10	8
	Cal. Cmt. Sst.	0	0	0	0	12	0	0
	Pebbly Sandstone	0	0	0	69	0	9	10
	Conglomerate	0	0	0	2	0	0	45
Precision		100.0%	80.0%	91.5%	91.3%	92.3%	47.4%	71.4%

Table C-1.6: Confusion matrix for MVCA classification using VShale, PHID.c, PHIN.c, PEF

Accuracy		Prediction						
91.3%		Shale	Silt-Shale	Sand-Silt	Sandstone	Cal. Cmt. Sst.	Pebbly Sandstone	Conglomerate
Actual	Shale	446	1	0	0	0	0	0
	Silt-Shale	0	22	6	0	0	0	0
	Sand-Silt	0	10	61	0	0	0	0
	Sandstone	0	0	0	735	1	15	11
	Cal. Cmt. Sst.	0	0	0	0	12	0	0
	Pebbly Sandstone	0	0	0	67	0	8	13
	Conglomerate	0	0	0	2	0	1	44
Precision		100.0%	66.7%	91.0%	91.4%	92.3%	33.3%	64.7%

Table C-1.7: Confusion matrix for MVCA classification using VShale, PHID.c, PHIN.c, AI

Accuracy		Prediction						
91.5%		Shale	Silt-Shale	Sand-Silt	Sandstone	Cal. Cmt. Sst.	Pebbly Sandstone	Conglomerate
Actual	Shale	447	0	0	0	0	0	0
	Silt-Shale	2	20	6	0	0	0	0
	Sand-Silt	0	10	61	0	0	0	0
	Sandstone	0	0	0	741	0	8	13
	Cal. Cmt. Sst.	0	0	0	0	11	0	1
	Pebbly Sandstone	0	0	0	67	0	7	14
	Conglomerate	0	0	0	1	0	1	45
Precision		99.6%	66.7%	91.0%	91.6%	100.0%	43.8%	61.6%

Table C-1.8: Confusion matrix for MVCA classification using VShale, PHID.c, PHIN.c, PEF, AI

C-2. Artificial Neural Network

Accuracy		Prediction						
90.9%		Shale	Silt-Shale	Sand-Silt	Sandstone	Cal. Cmt. Sst.	Pebbly Sandstone	Conglomerate
Actual	Shale	448	0	0	0	0	0	0
	Silt-Shale	0	20	8	0	0	0	0
	Sand-Silt	2	7	57	0	0	0	0
	Sandstone	0	0	0	580	1	1	11
	Cal. Cmt. Sst.	0	0	0	0	10	0	0
	Pebbly Sandstone	0	0	0	78	0	8	2
	Conglomerate	0	0	1	5	0	0	41
Precision		99.6%	74.1%	86.4%	87.5%	90.9%	88.9%	75.9%

Table C-2.1: Confusion matrix for ANN classification using GR, DEN, NEU

Accuracy		Prediction						
91.1%		Shale	Silt-Shale	Sand-Silt	Sandstone	Cal. Cmt. Sst.	Pebbly Sandstone	Conglomerate
Actual	Shale	448	0	0	0	0	0	0
	Silt-Shale	0	20	8	0	0	0	0
	Sand-Silt	3	5	58	0	0	0	0
	Sandstone	0	0	0	580	1	1	11
	Cal. Cmt. Sst.	0	0	0	0	10	0	0
	Pebbly Sandstone	0	0	0	76	0	9	3
	Conglomerate	0	0	1	4	0	1	41
Precision		99.3%	80.0%	86.6%	87.9%	90.9%	81.8%	74.5%

Table C-2.2: Confusion matrix for ANN classification using GR, DEN, NEU, PEF

Accuracy		Prediction						
90.3%		Shale	Silt-Shale	Sand-Silt	Sandstone	Cal. Cmt. Sst.	Pebbly Sandstone	Conglomerate
Actual	Shale	446	2	0	0	0	0	0
	Silt-Shale	0	17	11	0	0	0	0
	Sand-Silt	0	6	60	0	0	0	0
	Sandstone	0	0	0	582	0	0	9
	Cal. Cmt. Sst.	0	0	0	6	3	0	1
	Pebbly Sandstone	0	0	0	79	0	8	1
	Conglomerate	0	0	2	7	0	0	38
Precision		100.0%	68.0%	82.2%	86.4%	100.0%	100.0%	77.6%

Table C-2.3: Confusion matrix for ANN classification using GR, DEN, NEU, Vp

Accuracy		Prediction						
89.0%		Shale	Silt-Shale	Sand-Silt	Sandstone	Cal. Cmt. Sst.	Pebbly Sandstone	Conglomerate
Actual	Shale	447	0	1	0	0	0	0
	Silt-Shale	0	0	28	0	0	0	0
	Sand-Silt	3	0	63	0	0	0	0
	Sandstone	0	0	0	583	0	0	8
	Cal. Cmt. Sst.	0	0	0	6	2	0	2
	Pebbly Sandstone	0	0	0	80	0	6	2
	Conglomerate	0	0	1	10	0	0	36
Precision		99.3%	#DIV/0!	67.7%	85.9%	100.0%	100.0%	75.0%

Table C-2.4: Confusion matrix for ANN classification using GR, DEN, NEU, PEF, Vp

Accuracy		Prediction						
90.0%		Shale	Silt-Shale	Sand-Silt	Sandstone	Cal. Cmt. Sst.	Pebbly Sandstone	Conglomerate
Actual	Shale	446	2	0	0	0	0	0
	Silt-Shale	0	20	8	0	0	0	0
	Sand-Silt	1	7	58	0	0	0	0
	Sandstone	0	0	0	582	1	1	9
	Cal. Cmt. Sst.	0	0	0	0	9	0	0
	Pebbly Sandstone	0	0	0	83	0	0	5
	Conglomerate	0	0	1	10	0	0	36
Precision		99.8%	69.0%	86.6%	86.2%	90.0%	0.0%	72.0%

Table C-2.5: Confusion matrix for ANN classification using VShale, PHID.c, PHIN.c

Accuracy		Prediction						
90.5%		Shale	Silt-Shale	Sand-Silt	Sandstone	Cal. Cmt. Sst.	Pebbly Sandstone	Conglomerate
Actual	Shale	447	1	0	0	0	0	0
	Silt-Shale	0	20	8	0	0	0	0
	Sand-Silt	0	9	57	0	0	0	0
	Sandstone	0	0	0	584	1	0	8
	Cal. Cmt. Sst.	0	0	0	0	9	0	0
	Pebbly Sandstone	0	0	0	79	0	5	4
	Conglomerate	0	0	1	8	0	2	36
Precision		100.0%	66.7%	86.4%	87.0%	90.0%	71.4%	75.0%

Table C-2.6: Confusion matrix for ANN classification using VShale, PHID.c, PHIN.c, PEF

Accuracy		Prediction						
89.5%		Shale	Silt-Shale	Sand-Silt	Sandstone	Cal. Cmt. Sst.	Pebbly Sandstone	Conglomerate
Actual	Shale	447	1	0	0	0	0	0
	Silt-Shale	0	0	28	0	0	0	0
	Sand-Silt	1	1	64	0	0	0	0
	Sandstone	0	0	0	583	1	0	9
	Cal. Cmt. Sst.	0	0	0	0	9	0	0
	Pebbly Sandstone	0	0	0	79	0	6	3
	Conglomerate	0	0	2	9	0	0	36
Precision		99.8%	0.0%	68.1%	86.9%	90.0%	100.0%	75.0%

Table C-2.7: Confusion matrix for ANN classification using VShale, PHID.c, PHIN.c, AI

Accuracy		Prediction						
91.2%		Shale	Silt-Shale	Sand-Silt	Sandstone	Cal. Cmt. Sst.	Pebbly Sandstone	Conglomerate
Actual	Shale	447	1	0	0	0	0	0
	Silt-Shale	0	20	8	0	0	0	0
	Sand-Silt	0	7	59	0	0	0	0
	Sandstone	0	0	0	583	1	0	9
	Cal. Cmt. Sst.	0	0	0	0	10	0	0
	Pebbly Sandstone	0	0	0	78	0	9	1
	Conglomerate	0	0	1	6	0	1	39
Precision		100.0%	71.4%	86.8%	87.4%	90.9%	90.0%	79.6%

Table C-2.8: Confusion matrix for ANN classification using VShale, PHID.c, PHIN.c, PEF, AI